A

The Morphology of Titanium Dioxide Aerogels

by

ZHU ZHU

A dissertation submitted to the Graduate Faculty in Physics in partial fulfillment of the requirements for the degree of Doctor of Philosophy, The City University of New York.

1996

UMI Number: 9618125

UMI
300 North Zeeb Road
Ann Arbor, MI 48103

This manuscript has been read and accepted for the Graduate Faculty in Physics in satisfaction of the dissertation requirement for the degree of Doctor of Philosophy.

Dec 15, 1995
Date

Prof. Micha Tomkiewicz
Chair of Examining Committee

Dec 18, 1995
Date

Prof. Joseph B. Krieger
Executive Officer

Prof. Peter Lesser

Prof. Ken Miyano

Prof. Steven G. Greenbaum

Dr. Min Lin

Supervisory Committee

The City University of New York

To My Parents

ABSTRACT

The Morphology of Titanium Dioxide Aerogels

by

Zhu Zhu

Advisor: Prof. Micha Tomkiewicz

The morphology of titanium dioxide TiO_2 aerogels has been characterized by four major techniques. This work will discuss these complementary techniques such as nitrogen adsorption, X-ray powder diffraction (XRD), electron microscopies (EM- TEM, SEM), and small angle neutron scattering (SANS). The results of these characterizations have shown that the morphology of titanium dioxide TiO_2 aerogels can be characterized in terms of two length scales: 5 nm diameter, crystalline nanoparticles of anatase closely packed into mesoaggregates about 50 nm in size. The mesoaggregates are, in turn, packed into a loosely linked structure with an overall porosity of 80%.

ACKNOWLEDGMENTS

I would like to express my sincere appreciation to all the people who were involved in this project. The success of this work was due to an outstanding group effort. Without the help of everyone involved I could not have completed all the steps of Ph.D. process. I enjoyed working with everyone and I would like to thank them for their time, friendship and advice. I would like to give a special thanks to my thesis advisor for his help, vision and financial support.

The major contributors to this project are as follows order:

Dr. M. Tomkiewicz, Dr. C. Thompson, Dr. W. M. Shen, Dr. G. Dagan, Mr. J. M. Bai, Dr. K. G. Huang, Dr. M. Lin, Dr. S. Sinha, Dr. J. S. Huang, Mr. D. Song, Dr. C. Forest, Dr. Y. M. Zhu, Dr. R. P. Nolan, Dr. A. M. Langer, Dr. L.Y. Tsung, Dr. G. F. Neilson, Dr. C. Wang, Dr. J. William, Dr. S. Krueger, Dr. D. W. Schaefer, Dr. P. Lesser, Dr. X. Wu.

This work was supported by the US Department of Energy and New York State Energy Research and Development Authority.

CONTENTS

LIST OF TABLES

LIST OF FIGURES

CHAPTER 1. Introduction

The relationship between form and purpose or morphology and functionality has been more clearly understood and applied to our daily life. The examples can go from trees, whose branches and roots developed for photosynthesis and use solar energy to produce carbohydrates and adsorb nutrition, to organizations which set up levels of departments for their operation. Material science is no exception. In this introduction, the scope and importance of porous media are emphasized as it relates to the many materials familiar to most of us.

§ 1. 1 Porous Materials

Porous materials are encountered literally everywhere in everyday life, in nature and in technology. The importance of the correlation between their behavior and their structure has long been recognized by scientists and engineers. For example, chemical reactivity, adsorptive capacity, and photocatalytic activity are dependent on pore structure. It has become a fast-growing interdisciplinary area, with special emphasis on a unified approach by scientists and engineers from such diverse fields as: civil, mechanical, agricultural, chemical, environmental, mining and petroleum engineering, geohydrology, soil physics, powder metallurgy, ceramics, biomechanics, mathematics and industrial filtration, water purification, and wastewater treatment [1].

There are many examples of porous materials in everyday life:

Textiles and leathers are highly porous; they owe their thermal insulating properties, as well as the ability of "breathing", to their pore structure.

Paper towels and tissues are also highly porous; they owe their absorbency partly to

their porous structure and partly to the property that they remain strongly water-wet [2].

Bread, cake, and pastry, tofu and cheese, whipped gelatin and beaten egg whites or whipped cream are highly porous, as are dried meats and vegetables. The most clear and easy way to imagine porous structure is to look at a sponge either of sessile animals, often siliceous or calcareous skeleton, or an elastic skeleton of plastic, cellulose, or rubber which are light in weight and highly absorbent.

Living organisms are not usually referred to as porous media, although cellular structure is a special kind of porous medium filled with a variety of different fluid substances. Lungs and bones both have unique and elaborate pore structures, and even skin and hair are porous.

There are also many examples of technology that depend on the properties of porous media or make use of porous media:

Medicine and biochemical engineering, biological membranes and filters, the flow of blood and other body fluids, and electroosmosis are a few examples where the role played by porous media is critical.

For chemical engineering, heterogeneous catalysis is an important technology where pore diffusion of gases as well as impregnation of porous catalysts with catalyst precursor and distribution of molten catalyst are processes that depend on pore structure. Chromatography and, in particular, gel permeation chromatography are important processes, which depend on both diffusion and flow through porous media. Other separation processes use porous polymer biological and inorganic membranes. Filtering of gases and liquids and drying of bulk goods are equally important technologies based on flow or diffusion through

porous media. The impregnation of plastics with plasticizers also depends on pore structure.

In electrochemical engineering, porous electrodes and permeable and semipermeable diaphragms for electrolytic cells play important technological roles in the struggle to obtain improved current efficiencies.

Meanwhile, porous materials play important roles in many technologies too.

Zeolites are porous crystals now commonly used in refining petroleum and for absorbing specific substances from air or water. In zeolites, aluminum or silicon atoms form rings that link to make channels and cages up to about a nanometer in diameter. Many exciting new developments have occurred in the industrial application and these developments have in turn inspired new fundamental science. The numerous new studies span all fields of science and technology such as mineralogy, geology, synthesis, ion-exchange, sorption, catalysis, etc.[3,4].

Ceramics are unique products in a wide variety of forms with an ever increasing range of applications. These materials have experienced fast developments in energy technology for both high and low temperatures, which includes power generation, energy saving, heat transfer, sensors and catalysts. Tailoring the properties and structure of ceramic materials to their specific functions in all possible applications requires a deep understanding of the relationships between composition and properties. There are new studies in the structure of crystalline and amorphous ceramic phases, surfaces and interfaces, the morphology of polycrystals, multiphase materials (including composites), fibrous and dispersed ceramic systems, and the response of all these forms of ceramic materials to mechanical loads, heat, aggressive environments, and to electromagnetic fields [5].

In the field of absorbance, particular attention is given to cross linked structures - polymeric materials which swell to more than fifty times their initial weight in water or electrolytic solutions [6].

Since the discovery of luminescence from porous silicon, many potential applications are listed in the areas of photo-electronic devices [7].

Porous materials such as foams, porous metals and aerogels have brought new opportunities to material science. Tailored porosity represents a material need in several important technologies such as: high efficiency gas separation membranes; catalytic membranes for chemical processing; porous electronic substrates for high speed electronics; precursors for making optical communications; high efficiency thermal insulators; porous electrodes for fuel cells; separators and electrodes for batteries; materials for storing fuels; selective absorbents for environmental cleanup, and reusable particulate filters.

Porous membranes are the leading candidates for new separation systems for the chemical industry, hot gas filtration for energy production, and separation media for numerous environmental cleanup technologies. Emerging transportation technologies, such as fuel-cell-powered vehicles, require efficient porous materials for electrodes, separators, and gas storage media. Next-generation batteries call for porous materials for electrodes and separators. Finally, porous substrates provide a viable way to reduce the dielectric constant in electronic substrates, thereby reducing the resistance-capacitance time constant for signal processing and leading to increased speed [8].

Various porous materials have their specific application due to the porous nature or porous morphology. Aerogels will be described in the next section. Their advantages and

applications will also be discussed.

§ 1. 2 Aerogels

What would it be like to hold in one's hand a solid, crystalline object composed almost entirely of empty space - a material so sparse in structure that it appears nearly as faint as the air itself? Such wispy, ethereal masses - almost like a solid, translucent version of beer foam - do exist. Since their first appearance in the 1930's [9,10], they were called aerogels. A significant development came in the1960s when Teichner and co-workers started to prepare aerogels by hydrolyzing metal alkoxides in alcoholic solutions [11-13], thereby drastically reducing the amount of water used and thus making the preparation of aerogels more feasible. The sol-gel techniques were practiced willingly and unwillingly since the first encounters with colloidal materials. One can imagine the frustration of the early Chinese and Egyptians laboring to find a suitable protective agent such as gelatin or Arabic gum to manufacture ink before finally succeeding in avoiding gelation, or of the alchemists trying to prevent the gelation of their "aurum potable". It is to the credit of contemporary material scientists, who have converted a source of frustration into an art, then into a technology, and now into a science. At the time the term sol-gel became common, many colloid scientists felt like Moliere's Monsieur Jourdan, who discovered at a very late age that, unknowingly, he had spoken prose all his life. In the same manner, some colloid scientists realized at one point that unknowingly and often unwillingly, they had been practitioners of sol-gel technologies.

What is now called sol-gel technology was originally developed by mineralogists for the preparations of homogeneous powders for use in studies of phase equilibria, by chemists

for manufacturing nuclear fuel pellets, and by ceramists for the preparation of advanced ceramic materials.

The development of sol-gel science and related colloidal techniques is contributing significantly to the development of the advanced materials required by the advanced technologies. For example, a crucial issue in the manufacture of ceramics for electronics is reliability. Improved processes are required to produce improved products, to minimize the number of rejects, and to achieve the high quality required for electronic parts. Product reliability (reproducible performance) comes with microstructure control, which requires process reproducibility, which in turn requires materials reproducibility. In this respect Turner points out that the sol-gel process exhibits a number of advantages over conventional ceramic processing. The first advantage is increased chemical homogeneity in multicomponent systems. A second advantage of the sol-gel process is the high surface area of the gels or powders produced, which leads to relatively low sintering temperatures. A third advantage is that relatively high chemical purity can be maintained because of the absence of grinding and pressing steps. Finally, a fourth advantage of the sol-gel process is that a range of products in the form of fibers, powders, coatings and spheres can be prepared with relative ease from simple solutions.

The term sol-gel science was coined in the 1950s to refer to the art of manufacturing materials by preparation of a sol, gelation of the sol, and removal of the solvent. In the field of ceramics and glass the term sol-gel applies not only to processes in which sols are gelled, but also to processes in which it is never clear whether discrete colloidal particles may at some time exist. If there is no evidence of a sol, the use of the term sol-gel can better be

thought of as an abbreviation of solution-gelation.

A stable dispersion of solid colloidal particles in a liquid is called a *sol*. Stable in this case means that the solid particles do not settle or agglomerate at a significant rate. If the liquid is water, the dispersion is known as an *aquasol* or *hydrosol*. If the liquid is an organic solvent, the dispersion is called an *organosol*. The term *gel* is applied to systems made of a continuous solid skeleton which is made of colloidal particles or polymers enclosing a continuous liquid phase. Drying a gel by evaporation under normal conditions results in a dried gel called a *xerogel* (air dried gel). Large capillary forces cause macroscopic shrinkage during drying. Xerogels obtained in this manner are often reduced in volume by a factor of 5 to 10 compared to the original wet gel as a result of stresses exerted by capillary tension in the liquid.

An *aerogel* is a special type of xerogel from which the liquid has been removed by *supercritical drying*. The product is mostly air, having volume fractions of solid as low as about 10%, hence the term aerogel.

Iler [14] defined the gelling in the following manner: where the particles are aggregate or linked together in branched chains that fill the whole volume of sol so that there is no increase in the concentration of silica in any macroscopic region in the medium. Instead, the overall medium becomes viscous and is solidified by a coherent network of particles that, by capillary action, retains the liquid.

The TiO_2 aerogels were prepared by sol-gel processing. The sol-gel processing is a chemical route via hydrolysis and condensation reactions of wet inorganic precursors employing a catalyst (e.g., HNO_3). At the functional group level, three reactions are

generally used to describe the sol-gel process:

$$-\mathrm{Ti}-\mathrm{OC_3H_7} + \mathrm{H_2O} \underset{\text{esterification}}{\overset{\text{hydrolysis}}{\rightleftharpoons}} -\mathrm{Ti}-\mathrm{OH} + \mathrm{C_3H_7OH} \qquad (1\text{-}1)$$

$$-\mathrm{Ti}-\mathrm{OR} + \mathrm{OH}-\mathrm{Ti}- \underset{\text{alcoholysis}}{\overset{\text{alcohol condensation}}{\rightleftharpoons}} -\mathrm{Ti}-\mathrm{O}-\mathrm{Ti}- + \mathrm{ROH} \qquad (1\text{-}2)$$

$$-\mathrm{Ti}-\mathrm{OH} + \mathrm{OH}-\mathrm{Ti}- \underset{\text{hydrolysis}}{\overset{\text{water condensation}}{\rightleftharpoons}} -\mathrm{Ti}-\mathrm{O}-\mathrm{Ti}- + \mathrm{H_2O} \qquad (1\text{-}3)$$

where R is an alkyl group, C_xH_{2x+1}. The hydrolysis reaction (Eq. 1-1) replaces alkoxide groups (OR) with hydroxyl groups (OH). Subsequent condensation reactions involving the ⋮Ti – OH groups produce ⋮Ti – O –Ti⋮ bonds plus the by-products alcohol (ROH) (Eq.1-2) or water (Eq. 1-3). Under most conditions, condensation commences before hydrolysis is complete. Because water and titanium isopropoxide are immiscible, a mutual solvent such as alcohol is normally used as a homogenizing agent. It should be noted that alcohol is not simply a solvent. As indicated by the reverse of Eq. 1-1 and 1-2, it can participate in esterification or alcoholysis reactions.

Chemical formulas can also be used to represent the reaction for hydrolysis and condensation as overall reactions:

$$\mathrm{Ti(OC_3H_7)_4} + 4\mathrm{H_2O} \rightleftharpoons \mathrm{Ti(OH)_4} + 4\mathrm{C_3H_7OH} \qquad (1\text{-}4)$$

$$\Sigma\mathrm{Ti(OH)_4} \rightleftharpoons \mathrm{TiO_2} + 2\mathrm{H_2O} \qquad (1\text{-}5)$$

$$\mathrm{Ti(OC_3H_7)_4} + 2\mathrm{H_2O} \rightleftharpoons \mathrm{TiO_2} + 4\mathrm{C_3H_7OH} \qquad (1\text{-}6)$$

After mixing, small sol particles grow to a diameter determined mainly by PH value and temperature of the basic alcoholic solution. During aging, these small sol particles start to agglomerate forming clusters, which ultimately constitute the branched network and exhibit a gelatinous mass. Sol-gel processing enables materials to be mixed on a molecular level then be brought out of solution either as a colloidal gel or a polymerized macromolecular network whilst still retaining the solvent. In the formation of *aerogels*, shrinkage of the wet gel is minimized by *supercritical drying* [15].

When a wet, porous material dries by evaporation, the changeover of the liquid to a vapor can cause stresses and strains that induce cracking, shrinkage, and even complete disintegration of delicate solid skeletons. Using supercritical drying, the liquid can be removed from the material's pores and the fractural contractions that ordinarily accompany drying can be avoided. Actually, this kind of drying has come into wide use in preparing biological samples.

Supercritical drying is performed by putting the wet gel in an autoclave. The pressure and temperature are then increased until they exceed the corresponding critical value of the solution. In this supercritical state there are no liquid/vapor interfaces, thus no capillary pressure nor surface tensions therefore relatively little shrinkage occurs. After the solvent is released from the autoclave by decreasing the pressure and subsequently cooling, an aerogel is obtained. The structure of which is nearly identical to the gel body in the wet state. In many cases, the liquid within the gel is replaced by liquid carbon dioxide CO_2 because it has lower supercritical temperature and pressure. Figure 1-1 shows a flow chart of sol-gel processing.

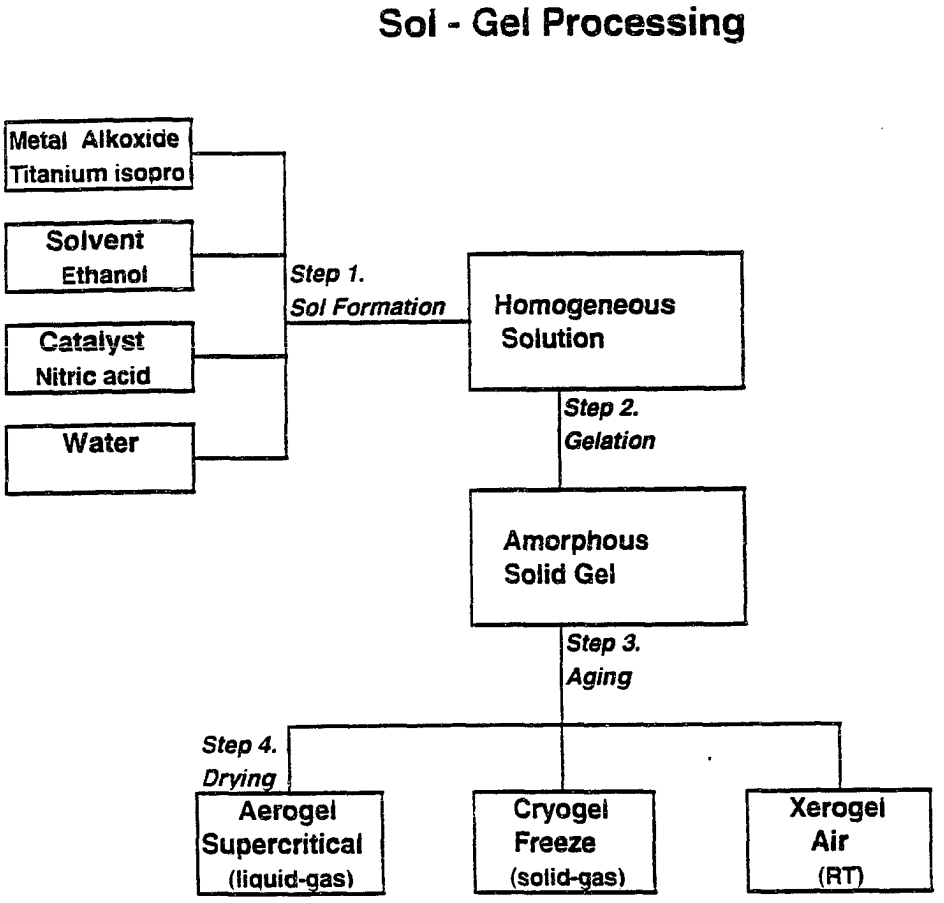

Figure 1-1 Sol-gel processing flow chart.

The resulting aerogels are solids of high porosity and high surface area with ultrafine cell/pore size (<100 nm). They have continuous three dimensional framework which is highly linked by an interconnected colloidal or polymeric primary particles about the order of 5-40 nm in size. They have an open structure with a relatively small solid cross sectional area through a given place. They are one of the lightest known solids with remarkably low densities about 0.1-0.5 g/cc. Aerogels are transparent because the characteristic size of the microstructure is much smaller than the wavelength of visible light, which allows light to be transmitted rather than scattered. Aerogels adsorb water and must be protected from the ambient.

Sol-gel processing has gained considerable attention and enormous effort has been devoted to develop various commercial applications. It is possible to achieve many technologically useful shapes and forms of materials and to control composition and purity much easier than by conventional processing. For example, coatings can be applied to architectural glass to enhance solar reflection. Fine ceramic powders can be formed which are uniform in size and can be sintered to high density at temperatures much lower than in conventional powder processing. Sols can be filled with other ceramic powders and used as a binding phase to enable good dense bodies to be obtained with minimal shrinkage. Glasses can be prepared at temperatures as low as one third of the fusion temperature, thereby avoiding the problems associated with high temperature fusion. Very thin coatings can be applied to almost any geometry of substrate and these coatings can be multi-layered to build up complex surfaces exhibiting nonlinear optical effects. Fibers can be drawn from partially hydrolyzed gels and subsequently densified by heat treatment. The highest porosity of all

solid ever tested makes aerogels so special that they could have important applications as optical fibers, catalyst supports: high-efficiency insulators, radiation detectors and for a wide variety of other electronic and optical applications [16].

CHAPTER 2. Photoelectrochemistry with TiO_2 Aerogels

§ 2. 1 Introduction

The primary photochemical processes occurring upon irradiation of a semiconductor are now well established [1-3]. By definition, a semiconductor has band structure, roughly characterized as a series of energetically closed spaced energy levels associated with covalent bonding between atoms composing the crystallite (the valence band) and a second series of spatially diffuse, energetically similar levels lying at higher energy and associated with conduction in the macromolecular crystallite (the conduction band). The magnitude of the fixed energy gap between the electronically populated valence band and the largely vacant conduction band governs the extent of thermal population of the conduction band (and hence the magnitude of the electrical conductivity of the particle) in its intrinsic (undoped) state. The band gap also defines the wavelength sensitivity of the semiconductor to irradiation.

Photoexcitation with light of an energy greater than the band gap promotes an electron from the valence band to the conduction band, creating an electronic vacancy or hole (h) at the valence band edge. The classical picture of a hole is that of a highly localized electron vacancy in the lattice of the irradiated semiconductor particle. This hole can initiate interfacial electron transfer or other chemical reactions to an adsorbate or, with the surface-bound OH radical, can itself diffuse into the solvent bulk. Since the carrier trapping is so fast, it is often the reaction of the hole with a substrate, rather than the carrier trapping itself, that often constitutes the rate determining step of a given sequence.

The photogenerated electron (e) usually relaxes thermally to the conduction band edge (and the hole to the valence band edge), but further deactivation is more difficult

because of energetic mismatching of the energies of the electron and hole. Only in special cases can nonthermalized "hot electrons" be transferred across the semiconductor interface at a rate competitive with internal relaxation. Conduction band electrons generated within semiconductor clusters by pulse radiolysis or by flash excitation of the suspended semiconductor exhibit characteristic chemical reactivity patterns which can be monitored by microwave conductivity measurements. The electrons are rapidly caught through equilibrium localization at a trap, followed by eventual recombination with a photogenerated hole at the semiconductor surface. Appreciable negative charge can be built up on a particle in the absence of an appropriate acceptor.

Unlike metals, semiconductors lack a continuum of interband states to assist the recombination of the electron-hole pair. This assures an electron-hole pair lifetime sufficiently long to allow these species to participate in interfacial electron transfer. Thus, the act of photoexcitation usually generates an electron-hole pair poised respectively at the conduction band and valence edges (Eq. 2-1). The components of this activated pair, when transferred across the interface, are capable, respectively, of reducing and oxidizing a surface-adsorbed substrate, forming on a common surface a singly oxidized electron donor and singly reduced electron acceptor (Eq. 2-2 and 2-3).

$$\text{Semiconductor} + h\nu \rightarrow (e, h) \qquad (2\text{-}1)$$

$$D + h \rightarrow D^{+} \qquad (2\text{-}2)$$

$$A + e \rightarrow A^{-} \qquad (2\text{-}3)$$

When the semiconductor is in contact with an electrolyte containing a redox couple, the Fermi level of the semiconductor moves to equilibrate with the potential of the redox

couple. Contact between the semiconductor and the electrolyte establishes a Schottky barrier. The electric field of this Schottky barrier induces spatial separation between e and h by driving the photogenerated e and h in opposite directions, causing the bands to bend at the solid-liquid interface. The fermi level of the semiconductor then moves to equilibrate with the potential of the redox couple. Charge carriers are driven to surface trapping sites either by diffusion or by migration induced by the space-charge gradient (See Fig. 2-1).

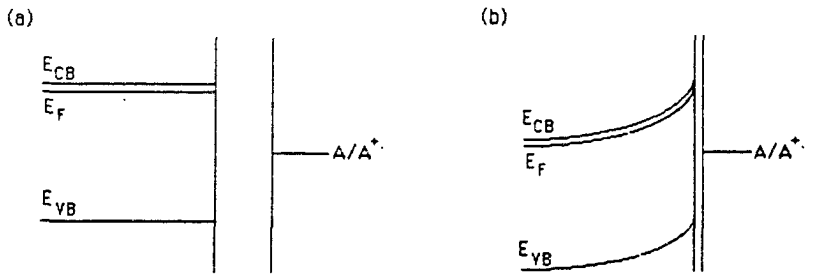

Figure 2-1 Band structure in a semiconductor: (a) before contact with an electrolyte and (b) in contract with an electrolyte.

If a photogenerated hole reaches the surface of the semiconductor, it can react with an adsorbed substrate by interfacial electron transfer, assuming that the adsorbate possesses a redox potential appropriate for a thermodynamically allowed reaction. Thus, an adsorbed electron donor can be oxidized by transferring an electron to a photogenerated hole on the surface, and an adsorbed acceptor can be reduced by accepting an electron from the surface. Hole trapping generates a cation radical, D^+ (Eq. 2-2), and electron trapping generates an anion radical, A^- (Eq. 2-3).

These radical ions can participate in several path ways: (1) they may react chemically

with themselves or other adsorbates. (2) they may recombine by back electron transfer to form the excited state of one of the reactants or to waste the excitation energy by a nonradiative pathway. (3) they may diffuse from the semiconductor surface and participate in chemical reaction in the bulk solution. If the rate of formation of D^+ is kinetically competitive with the rate of back electron transfer, photoinduced oxidation will occur for any molecule with an oxidation potential less positive than the semiconductor valence band edge, since under these conditions interfacial electron transfer at the illuminated interface is thermodynamically allowed. By similar considerations, the photoinduced reduction can occur, barring kinetic restraints, to any molecule possessing a reduction potential less negative than the conduction band edge.

§ 2. 2 Titanium Dioxide

Crystal structure of TiO_2 polymorphs

The mineral form of titanium dioxide, TiO_2, is titania. Most titania specimens are nonstoichiometric and are slightly deficient in oxygen. Titania can occur in seven crystalline modifications. There are currently four naturally occurring TiO_2 polymorphs (rutile, anatase, brookite, and TiO_2 (B)) and at least three (plus some very high-pressure forms) polymorphs that have been produced synthetically [4,5].

Titanium derivatives occur in nature as minor components in many rocks - biotite, pyroxene, etc.. However, rutile is much more common than the rest of them. It is usually red or brownish-red because of impurities such as Fe, Nb, Ta and, to a lesser extent, Sn, Cr and V [6]. Rutile ore, containing titanium, which is the ninth most abundant element in the Earth's crust [7], is principally obtained from heavy sands, ilmenite, an iron titanate, which

is more widely distributed. The largest deposits of rutile in the world are in Sierra Leone on the southwestern coast of the bulge of West Africa [8]. The most widely used are rutile and anatase.

All of the polymorphs contain edge- and corner-linked, octahedrally coordinated Ti cations. The available structure refinements show relatively constant Ti-O distances (about 1.9 Å) and quite variable O-O distances, particularly when the shared vs. unshared octahedral edges are compared. Pairs of face-sharing octahedra (containing trivalent Ti) are found only in crystallographic shear structures in reduced rutile derivatives (TiO_{2-x}). All of these structures except rutile can be constructed from a unit composed of four edge-sharing octahedra. The basic rutile structural elements can be created by the stacking of this assembly by shear.

Both anatase and rutile are tetragonal. The two crystal structure of TiO_2 is made of titanium octahedrally coordinated with oxygen atoms (See Fig.2-2). All the polymorphs display a sixfold coordination of oxygen about a titanium atom, with each of the oxygens occupying the corners of a regular octahedron. In turn, every oxygen atom is coordinated with three titanium atoms occupying the approximate corners of an equilateral triangle. This structure has been referred to as a 6:3 coordination and is referred to by crystallographers as the "rutile structure". Though this coordination is constant, the octahedra bond angles and distances differ among the polymorphs so that the sharing of edges of the octahedrons increase from two in rutile, to three in brookite, to four in anatase.

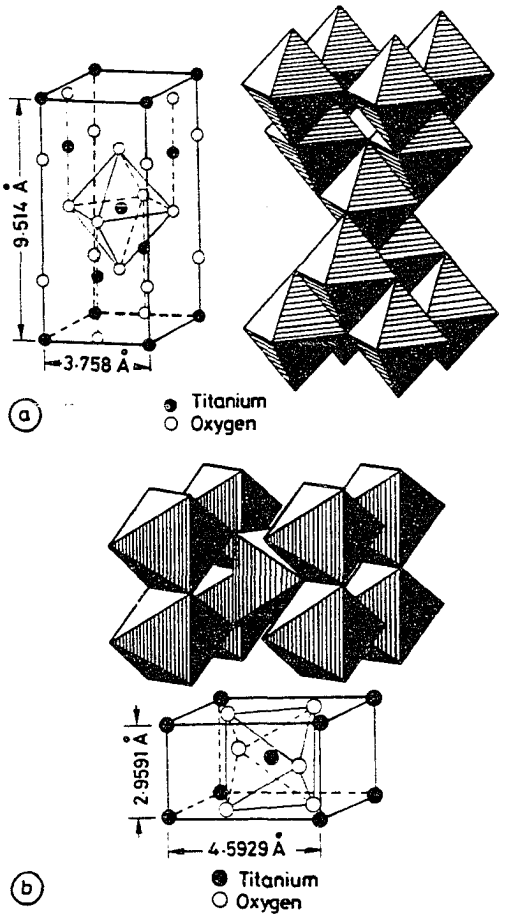

Figure 2-2 Crystal structure of (a) anatase and (b) rutile.

For rutile and anatase, the positions of the octahedra in the unit cell differ. Anatase contains four TiO_2 molecules per unit cell while rutile contains two. As edges and faces of the octahedra are increasingly shared, the titanium distances decrease, setting up cation repulsive forces. This decreases the stability of the mineral structure and is reflected in such basic features as hardness and solubility. Rutile, the most stable, is the hardest and least soluble polymorph. The small variations in the structure of rutile and anatase lead to different cleavage and twin planes along which separation tends to occur. Therefore, one would assume that for anatase and rutile the density of surface titans, and their isoelectric point for anatase and rutile, would differ regardless of whether the crystals are similarly

grown to a certain size or being reduced in size from larger particles.

Properties and applications of anatase and rutile

Titanium dioxide is industrially important as a white pigment for paints, sunscreen agents, emollients, linoleum and conditioning agents, in many plastics applications, in the production of white paper, ceramic, rubber, leather, enamel and fabric industries, instant vanilla-pudding mixes, many toothpastes, and in such products as false teeth. This is a consequence of the high refractive index of titania and its relatively low and uniform absorption of visible light. Why does white paint remains cool in sunlight ? This is because white paint has titanium dioxide which is an excellent absorber, and therefore emitter, not reflector in the infrared. Also its relative chemical inertness and the comparative abundance (and hence low cost) of titanium ores are suitable for its manufacture.

1) The crystal lattice and bulk properties:

The rutile modification of titania has greater density, hardness and a higher refractive index than the anatase form (See Table 2-1). Unlike the massive crystalline forms of titania, the powder crystalline forms do not have well developed crystalline structures, but consist essentially of small domains of crystalline lattice with nonplanar surfaces, surrounded by disordered regions [9].

2) Other physical properties:

Rutile is an insulator at room temperature (conductivity 10^{-14} $ohm^{-1}cm^{-1}$), but the specific conductivity, which is highly anisotropic, rises rapidly with increasing temperature. The conductivity of rutile is also strongly dependent on the exact stoichiometry. In addition to the above factors, the conductivity of rutile is affected by: the pressure, the history of the

sample, the length of time for which the field has been applied and the concentration of impurity ions in the lattice.

Titanium dioxide, which is n-type semiconductor, also possesses a wide range of semi-conductor and dielectric properties, which are highly dependent on the density of point defects. Indeed much photochemical research has been carried out on this oxide due to its band structure (See Table 2-2).

Table 2-1 Comparison of Physical Properties of the Titanium Dioxide Polymorphs [6]

	Anatase	Rutile
X-ray JCPDS	21-1272	21-1276
Crystal system	Tetragonal	Tetragonal
Unit Cell (nm) a	0.379	0.459
c	0.951	0.296
Z Cell	4	2
Distance Ti-O (nm)	0.191	0.194
Density (g/cm^3)	3.90	4.27
Hardness (Mohs'scale)	5.5-6.0	6.0-6.5
Melting Point (°C)	Change to rutile	1840
Refractive Index (25°C)	2.56 (λ=589 nm)	2.61
Energy Gap (eV)	3.20	3.05
Dielectric Constant	48	110 - 117

Table 2-2 Band-gap Energies of Common Semiconductors [6]

	Ge	Si	InP	GaAs	CdSe	GaP	TiO_2
eV	0.7(I)	1.12(I)	1.35	1.44	1.70	2.26(I)	3.0(I)

(I) indicates that an indirect gap is the lowest-energy optical transition.

§ 2. 2 Photoelectrochemistry with TiO_2 Aerogels

Any functionality that involves optimization of different length scale should require some kind of ramified structure. The possible correlation between morphologies of catalytic structures and the catalytic activity was reviewed by Van Damme [10]. For photocatalytic activity we need to optimize substrate light adsorption with diffusion of products and reactants. We wish to study the rules that correlate the morphology of a porous or ramified photocatalyst with the efficiency of photocatalytic reactions, such that for a desired photocatalytic reaction, one could design the morphology of the photocatalyst for an optimized reaction rate.

The morphological requirements of such a catalyst will depend on the intended application. For the application of photocatalytic decomposition of organic solutes in an aquatic environment, we have two requirements: 1) the density should be smaller than water to enable the photocatalyst to float even in a completely soaked state. 2) we need to simultaneously maximize the real surface area for maximum adsorption of the reactant, and the light exposed area that is approximately (neglecting transmission and reflection) equal to the geometric area. The low density requires a porous structure, but what kind of porosity is needed? For given porosity the need to maximize the real area for a given geometric area requires the smallest possible pores but, in addition, one needs to maximize the diffusion

rates of oxygen, CO_2 and the unabsorbed reactants that will require unhindered pathways, which means large pores. A dilute dispersion of the photocatalyst on a support will not suffice because of the requirement to maximize light absorption.

Aerogels are highly porous materials derived from the sol-gel processing and supercritical drying. Because of their ultra-low density, high homogeneity, and large surface area, aerogels have recently attracted great attention in various applications [11,12]. One of the major focal-points is that aerogels satisfy the above two requirements in water pollution control applications. It was demonstrated that titanium dioxide (TiO_2) aerogels can be used as an effective photocatalyst for photooxidation of organic and organometallic compounds [10,13-15]. They are also naturally good candidates as supporting substrates for catalysts [16].

The surface of titanium dioxide is capable of oxidizing or reducing a wide variety of adsorbed or contacted inorganic and organic compounds when these are exposed to light of wavelengths 300 - 400 nm. This activity can have a number of practical applications. The photodecomposition of water on titanium dioxide surfaces can yield hydrogen, thus providing a potential means of solar energy storage. Titanium dioxide also functions as an efficient photocatalyst, dramatically speeding the sunlight-mediated breakdown of many chemicals, including toxic hydrocarbons. So titanium dioxide aerogels can be considered as for clean up of oil spills [13].

The role played by titanium dioxide in photocatalysts is due to its absorbtion of near-ultraviolet light. This absorption results in the conversion of light quanta into excited lattice species, in which electrons are promoted from the valence band to the conduction band in

the lattice electronic structure. The energy gap between these bands in the rutile lattice is approximately 3.05 eV, and 3.20 eV in the anatase lattice (See Table 2-2). These energy levels correspond to light quanta having the respective wavelengths of 420 and 380 nm, which correspond in turn to the long wavelength edges of the rutile and anatase lattice absorption bands. A light having wavelengths shorter than these critical values is absorbed with the formation of "excitons" or electron-hole pairs (h-e). These can dissociate into free, mobile holes (h) and electrons (e) that are capable of migration through the lattice to the surface or other reactive sites. The formation of an exciton corresponds, in terms of discrete Ti^{4+} and O^{2-} ions, to the transfer of an electron from an oxygen 2p to a titanium 3d orbital.

Five different aggregation modes can be classified for photoelectrochemistry on semiconducting substrates [17], they are powder mode, aerogel mode, nanocrystalline film, polycrystalline film and single crystal. In powder mode, the particles (isolated nanocrystalline grains) are well defined but the interparticle space is constantly changing. Interparticle transport can take place only through the surrounding electrolyte. In aerogel mode, the fundamental units remain nanocrystallites but they aggregate to establish connectivity. The surface area and most of the bulk properties are similar to ones obtained with the powders but the interparticle pore space is well defined and interparticle transport can take place not only through the electrolyte but also between particles. For nanocrystalline film electrodes, the morphology is similar to the aerogels but they are deposited on a substrate. In this mode one can measure collective macroscopic charge-distributions such as current and voltage. For polycrystalline electrodes, much of the nanocrystalline grain structure remains, although at a much higher packing density, and the

void structure is replaced by grain boundaries. The final aggregation mode in this procession takes place when the individual grains and their associated grain boundaries disappear and the solid crystallizes to form a single crystal. The specific surface area across these aggregation modes varies between 10^3 to 2.5×10^{-5} m^2/g. The output parameters are different photocatalytic products with the non-electrode configurations and photovoltaic performance parameters with the electrode-style configurations. One can also find considerable overlap; photocatalytic activity is being investigated throughout the series and photovoltaic performance starting with the nanocrystalline electrodes. Subject to their intrinsic limitations (bandgap and band location), in almost all the systems, TiO_2 is among the most efficient in the respective categories. This brings into focus the need to parametrize these systems in terms that can be applied across the different aggregation modes. Unfortunately, there are not many studies on photoelectro-chemistry with aerogel mode even though there is a large volume of literature on photoelectrochemistry with most of these aggregation modes using the same semiconducting materials - TiO_2. For instance, the dynamics of interfacial electron-transfer reactions were studied with colloidal TiO_2 [18]. Vlachopoulos et al reported that by using high surface area polycrystalline anatase films, together with tris ruthenium (II), RuL_3^{4-}, as a sensitizer, they have achieved unprecedentedly high visible light to electric current conversion efficiencies in regenerative photoelectrochemical cells. Incident photon to current conversion efficiencies of 73% have been obtained at a wavelength of maximum absorption of dye in the presence of iodide as an electron donor [19].

For the TiO_2 aerogels, the control of the morphological parameters can come at almost every stage of the preparation procedure; at the onset during the colloidal stages of

the sol, appropriate control parameters are: water contents, temperature, acidity, ionic strength, etc.. During the aging process, one can affect the strength of the connectivity between the individual mesoparticles by adjusting the chemistry of the gelation environment.

The work presented in this thesis is the investigating of the morphology of titanium dioxide aerogels by applying various independent characterization techniques, in order to correlate the morphology of the porous photocatalysts with their catalytic activity [13,15]. The purpose of this study, the characterization and understanding the morphology of titanium dioxide (TiO_2) aerogels, is three fold. First, titanium dioxide aerogels are a model example of porous media which has great potential to be developed into new materials through morphological engineering of traditional substances. Secondly, this work leads to a better understanding of the fundamental aspects of characterizing aerogels based on techniques such as: gas adsorption, X-ray powder diffraction, electronic microscopy and scattering methods. And finally, it is vital to study the pore structure requirements for important applications. TiO_2 is a good photocatalyst which can be applied to environmental protection (e.g., photocatalytic degradation of organic compounds in an aqueous environment). It is significant then, to understand the correlation between its morphology and its functionality.

This work will include experimental measurements and development of models with theoretical calculations coupled with data analysis. Comparisons between the different methods of measurement and their results will also be studied.

The remainder of this thesis is structured as follows: Chapter 3 provides a review of both concepts to define porous materials and techniques to characterize porous materials.

A detailed procedure on the preparation of titanium dioxide aerogel samples is given. Chapter 4 demonstrates pore size information using nitrogen adsorption. Chapter 5 illustrates the results of nano-crystal size of titanium dioxide aerogels (anatase) by X-ray powder diffraction. Chapter 6 is a study of small-angle neutron scattering. Chapter 7 presents a study of electron microscopy on titanium dioxide aerogels. Chapter 8 correlates and compares the microstructural parameters obtained from nitrogen adsorption, helium pyknometry, X-ray powder diffraction (XRD), small angle neutron scattering (SANS) and electron microscopy (TEM, SEM).

CHAPTER 3. Characterization TiO_2 Aerogels

Von Buzagh in 1937 [1] clearly identified the variables that must be taken into account to define an aggregate structure:

1) The size and shape of the primary particles.

2) The spatial distribution of the particles, including the order and density of packing.

3) The strength of the bond between particles.

He further pointed out that the size of the particles determines the specific surface area. For a given density of packing, the size of the particles determines the size of the pores throughout the aggregate or gel [1]. It is necessary to know what parameters will define the pore structure before the characterization. In this chapter we discuss the macroscopic pore structure parameters along with the experimental methods used for their determination.

§ 3. 1 Parameters of Pore Structures

The unique property of a porous medium, the one that distinguishes it from other solid bodies, is its complicated pore structure (empty spaces in the solid are called voids, pores, or capillaries, etc.). The vast majority of porous media contain an interconnected three-dimensional network of capillary channels of nonuniform sizes and shapes, commonly referred to as *pores*. But the conventional concepts of pore structure lose meaning as the pore size approaches molecular dimensions.

A pore is defined as a portion of empty space bounded by solid surfaces, just as a room is defined by its walls and the doors opening into it. If the local minima, the pore throats (the doors), can be located and imaginary partitions erected at these positions (the doors closed) then the pores are defined, and their size can be determined by any arbitrary

definition of size of an irregularly shaped object. Such definitions have been used for a long time in the field of particle size measurement. (The concept of void particles was introduced by Rumpf in 1966[2]).

All macroscopic properties of porous media are influenced, to a greater or lesser degree, by the pore structure. Pore structure parameters are those properties that are completely determined by the pore structure of the medium and do not depend on any other property. Macroscopic pore structure parameters represent average behavior of a sample containing many pores. Full description of a porous solid may require many parameters such as: porosity, density, surface area, pore volume, pore size (mean, hydraulic radius/diameter, pore size distribution), pore connectivity, pore shape, pore surface roughness, and others. Unfortunately, these parameters are commonly used without precise definition. So the definition of these parameters will be given as follows:

Porosity

Porosity ϕ is defined as the volume fraction of a solid that is porous. (or the fraction of the bulk volume of the porous sample that is occupied by pore space.) Depending on the type of the porous medium, the porosity may vary from near zero to almost unity.

It is important to distinguish between two kinds of pore space, one that forms a continuous phase within the porous medium, called interconnected pore space, and the other that consists of isolated or noninterconnected pores dispersed over the medium. Dead-end or blind pores are interconnected only from one side.

Depending on the measurement technique, either open porosity or total porosity is obtained. Also, the measure of the open-pore volume varies with the probe used. Therefore,

when porosity values are reported, they should also be accompanied by a description of the measurement. The problem is particularly acute for powders where intergranular voids may or may not be included as porosity. There are various experimental methods used to determine porosities:

1) Direct method. This method consists of measuring bulk volume of a porous sample and then somehow destroying all the pores and measuring the volume only of the solids.

2) Mercury injection method. The bulk volume of the sample is determined by immersion of the sample in mercury. As most materials are not wetted by mercury, the liquid will not penetrate into the pores.

3) Gas expansion method. This method also measures the effective porosity. The bulk volume of the sample is determined separately. (See Ch. 4)

4) Density methods. Density methods depend on determining the bulk density of the sample and the density of the solids in the sample. (See Ch. 4)

5) X-ray method. The porosity of the sample can be calculated through X-ray transmission which is determined by attenuation of the scattered signal from a sample,

$$T = \exp[-\mu t(1-\phi)] \qquad (3\text{-}1)$$

where μ is the linear absorption coefficient, t is the sample thickness (determined with an optical microscope), and ϕ is the porosity [11].

Density

The *true density* is defined as the ratio of the mass to the volume occupied by that

mass. Therefore, contribution to the volume made by pores or internal voids must be subtracted when measuring the true density. Regardless of whether pores and internal voids are present, the density of fine powders is often not the same as that of larger pieces of the same material because in the process of preparing many powders, those atoms or molecules located near the surface are often forced out of their equilibrium position within the solid structure. On large pieces of material the percentage of atoms near the surface is negligibly small. However, as the particle size decreases, this percentage increases with its resultant effect upon the density.

When the fluid displaced by powder does not penetrate the pores, the measured density will be less than the true density. When densities are determined by liquid displacement an *apparent density* is obtained which can differ according to the liquid used because of their different capabilities to penetrate small pores. Therefore, when reporting apparent density, the liquid used should also be reported.

The volume occupied by the solid, plus the volume of voids when divided into the sample mass, yields the *bulk density*. Therefore, when the sample is poured into a graduated container, the bulk density is the mass divided by the volume of the powder bed.

Skeletal density is the density of the solid matrix only. Density as measured by helium (or other fluid) displacement may be lower than the true density if closed pores are present. Bulk density is the mass of the porous solid over total sample volume (solid phase + closed pore + open pore). However, for porous powders, bulk density may refer tc the bulk density of either individual particles or the sample bed [3].

Specific surface area

The specific surface of a porous material is defined as the interstitial surface area of the pores either per unit mass (S/M) or per unit bulk volume (S/V) of the porous material. It is equal the sum of its internal and external surface areas. The specific external surface area, S_e, corresponds to the geometric surface of porous particles per gram. S_e is an inverse function of the particle size. For spherical particles of equal size

$$S_e = 6 / D_p \rho_s \qquad (3\text{-}2)$$

where D_p is the diameter of the spherical particles and ρ_s the skeleton density of the porous solid. The internal surface area, S_i, originates from the pore walls. As by definition, pores have to be open to the exterior of the particle. S_i does not include the walls of closed pores.

Normally, the specific surface area is obtained for all pores present within the porous particles. By applying special methods, the specific surface area of micropores and mesopores (definition is in the section of mean pore diameter) can be estimated separately.

Surface area can vary dramatically depending on both technique and data analysis method. The surface area of both open and closed pores is measured via scattering, but only the accessible porosity is detected with adsorption or mercury porosimetry. Depending on the temperature and adsorbate size, the measured surface area may differ.

Specific Pore Volume

The specific pore volume, V_p, is the amount of liquid adsorbate that fills the total volume of pores per gram of adsorbent. To the first degree approximation, V_p should be independent of the type of liquid, provided that the liquid wets the surface. By analogy to the specific surface area, the total specific pore volume can be attributed to the volumes of micropores, mesopores and macropores. Once V_p is known, the particle porosity, ϕ, can be

calculated by the equation

$$\phi = V_p / (V_p + V_s) \qquad (3\text{-}3)$$

V_s is the volume of pore solid per gram and corresponds to the reciprocal of the skeleton density.

Mean pore diameter

Mean pore diameter, D, may span several orders of magnitude, ranging from molecular size to macroscopic cracks. In 1971, a pore size classification was adopted by the International Union of Pure and Applied Chemists (IUPAC), which was based mainly on the work of Dubinin [4]. A specific nomenclature for porous materials has been recommended: micro porous (pore diameter $D < 2$ nm), mesoporous ($2 < D < 50$ nm), or macroporous ($D > 50$ nm) [5,6]. These dimensions are somewhat artificial since they arise from nominal limits associated with characterization techniques and specific applications to gas separation.

As every pore represents a distinct geometric space, its shape also has to be taken into consideration. Because of the irregularities in most porous solids, the real shape is known in only a few instances, and models have to be employed for an approximation [7].

Pore size distribution

So far, our treatment has been restricted to the parameter characterizing the pore itself. However, in practice, one has to consider the porous solid as a whole, i.e., the three-dimensional assembly of pores exhibiting a distinct size distribution f(D)dD, meaning the distribution density of pore volume by some length scale assigned to it. Every method of pore size distribution determination defines pore size in terms of a pore model best suited to the quantity measured. The general procedure used for pore size distribution determination

consists of measuring some physical quantity in dependence on another physical parameter that is under the control of and is varied by the experiment. For example, in nitrogen adsorption, the volume of nitrogen penetrating the sample is measured as a function of the pressure imposed on the nitrogen. The pore size is calculated from this pressure by Laplace's equation of capillarity and, using the bundle of capillary tubes model of pore structure, the volume of nitrogen is assigned to this pore.

Usually, pore size distributions (PSDs) can be expressed in two forms: one is the size histograms; the other is continuous distribution function. The size histograms can be provided if there are a sufficient number of size classes represented. Plots in which the number, volume, or weight of particles (pores) are represented as ordinate and the size range of particles, then yield graphs with rectangular steps. The height of each rectangle is the percentage of the number (or wight) of particles in the size class. The area enclosed by the histogram represents the total frequency (it sums to 100%).

The limit of the histogram obtained with a large number of increments is a continuous distribution curve. A mathematical representation of these curves is often useful and possible if a distribution function f(D) can be shown to fit the experimental data. In this case, the relative frequency, that is, the relative number of particles in any chosen interval, can be determined by integration of the function as follows

$$\int f(D)\, dD \qquad (3\text{-}4)$$

Several types of distribution functions are encountered in particle size measurements. The simplest curve shape, but one seldom adequate to represent actual particle samples, is the normal probability. It resembles a Gaussian distribution, its standard deviation being a

direct measure of the width of the dispersion.

The normal distribution which is said to fit classified particles that have a narrow size range or the PSD is homogeneous. However, most particles were found to have size distribution curves that are skewed with a long tail extending toward larger sizes. Frequently such skewed distributions exhibit equal frequencies of components whose dimensions have equal ratios to the mean size, rather than differences from it. If this is the case, the curve can be converted to the normal probability form by use of the logarithm of the dimension, and the system is said to obey the log-normal distribution.

Sometime, PSDs are presented in either cumulative (volume versus radius/diameter) or differential form (dV/dr versus r). Here V is volume and r pore radius. For very broad PSDs, the log-differential distribution is also presented as dV/dlog (r) as a function of pore size.

Some miscellaneous methods of pore size distribution determination are: mercury porosimetry and sorption isotherms, scattering technique, X-ray absorption, ion exchange diffusion and frequency response methods.

§ 3. 2 Characterization Techniques

This section surveys the methods used to determine the morphology or parameters mentioned in previous section for titanium dioxide aerogels. This is done by presenting the output of each method, together with comments on its advantages and limitations. More detailed theoretical principles, methodology, comparison and utilization of these techniques will be presented in later chapters.

Pores are invisible to the naked eye in the majority of porous media. The porous

nature of a material is usually established by performing any one of a number of experiments on a sample and observing its behavior, because porous materials behave differently from nonporous ones in a number of respects. Usually, if the width of the size distribution is not large, as indicated by preliminary microscopic examination, then a variety of methods will produce nearly the same average size, so that the choice of a method can be based on the simplest and most reliable techniques that are easily available. However, if the size distribution is broad, then there is a need to compare size results with an average size that is related to the properties of interest [8-10].

Several novel experimental techniques with particular high-resolution have been applied to characterize the TiO_2 aerogels in this work. They are: density measurement, nitrogen adsorption techniques, X-ray powder diffraction and Small Angle Neutron Scattering (SANS) techniques and electron microscopies, such as high-resolution Transmission Electron Microscopy (TEM) and Scanning Electron Microscopy (SEM). These techniques cover different length scales of structure determination. Density measurements yield information about the total cavity volume in the sample. The adsorption method, on the other hand, measures the total surface area, and information on differential pore size distribution can be obtained through a model-dependent analysis. The X-ray powder diffraction was used to characterize the phase of titanium dioxide and crystal size of the primary particles of the aerogels. Electron microscopy supplies a direct image which is unparalled by written description. It allows the locations and sizes of individual pore and particle to be determined. However, mean pore sizes and size distributions may not be accurate because of limited statistics which are associated with the low number densities of

pores. Whenever very small pores are present along with larger ones, it is difficult to make sure that all the small pores have been accounted for by the measurement. This is one of the reasons why PSD determined by image methods may differ significantly from the results obtained by other methods. Electron microscopy techniques are model independent but two dimensional in character.

In principle, one of the most powerful techniques for measuring particle sizes and number densities with high precision is SANS. The intensity of scattered radiation depends on the contrast in scattering power between the two phases. Neutrons have a large penetration length in most high density materials, thus large volumes are covered in one experiment providing statistically meaningful information about the total volume, number density and size of pores. The SANS techniques are model-dependent but bulk-characteristic in all interfaces.

§ 3. 3 Preparation of TiO_2 Aerogels

The titanium dioxide aerogels were prepared by the following procedure:

First, a TiO_2 sol was made containing: 1 $Ti(O\text{-}C_3H_7)_4$: 20 ethanol : 3 H_2O : 0.08 HNO_3. Titanium isopropoxide $Ti(O\text{-}C_3H_7)_4$ (Alfa) was mixed with the anhydrous ethanol (analytical grade, Aldrich) at room temperature and added to a solution of ethanol + deionized water + 70% nitric acid over a 5 minute period. The sol was stirred for additional 5 minutes before being transferred to plastic petri dishes. The hydrolysis reaction is rapid compared to the condensation reaction. Hydrolysis and condensation reactions lead to the formation of the gel structure. The network formed during condensation is highly porous and interconnected. The gels were then left to age from a few days to weeks at room temperature

in air-tight containers completely immersed in alcohol before supercritical drying. The supercritical drying was carried out in a SAMDRI-790A (Tousimis) critical point dryer, which replaced the alcohol in the gel with carbon dioxide at the critical point of the carbon dioxide (35°C and 1200 psi). The resulting aerogel has a low density (0.5 g/cm^3) and a high porosity (80%).

CHAPTER 4. Nitrogen adsorption

§ 4. 1 Introduction

Nitrogen sorption measurements are mainly applied in routine pore structure analysis. The methods of gas adsorption can probe the surface irregularities and pore interiors even at the atomic level. In this manner a very powerful method is available which can generate detailed information about the morphology of surfaces.

It has long been known that a porous solid can take up relatively large volumes of condensable gas. Already in 1777 Fontana noted that freshly calcined charcoal was able to take up several times its own volume of various gases; and in the same year Scheele recorded that "air" expelled from charcoal on heating was taken up again on cooling [1]. It was soon realized that the volume taken up varies from one charcoal to another and from one gas to another. The term *adsorption* appears to have been introduced by Kayser in 1881 to connote the condensation of gases on free surfaces, in contrast to gaseous absorption where the molecules of gas penetrate into the mass of the absorbing solid [1].

To some extent adsorption always occurs when a clean solid surface is exposed to vapor. Invariably the amount adsorbed on a solid surface will depend the absolute temperature T, the pressure P, and the interaction potential E between the vapor (adsorbate) and the surface (adsorbent). Therefore, at equilibrium pressure and temperature the volume V of gas adsorbed on a unit volume of adsorbent is determined by

$$V = f(P, T, E) \qquad (4\text{-}1)$$

Usually the quantity adsorbed is measured at a specified temperature and Eq. 4-1 reduces to

$$V = f(P, E) \qquad (4\text{-}2)$$

A plot of V versus P, at constant T, is referred to as the adsorption isotherm of a particular vapor-solid interface. Were it not for the fact that E, the interaction potential, varies with the properties of the vapor and the solid and also changes with the extent of adsorption, all adsorption isotherms would be identical.

Depending upon the strength of the interaction, all adsorption processes can be divided into two categories: chemical and physical adsorptions. The former, also called irreversible adsorption or chemisorption, is characterized mainly by large interaction potentials, which leads to high heat of adsorption often approaching the value of chemical bonds. The second category, reversible or physical adsorption, exhibits characteristics that make it most suitable for surface area determinations as described by the following:

1) Physical adsorption is accompanied by low heat of adsorption with no violent or disruptive structural changes occurring to the surface during the adsorption.

2) Unlike chemisorption, physical adsorption may lead to surface coverage by more than one layer of adsorbate. Thus, pores can be filled with the adsorbate for pore volume measurements.

3) At elevated temperatures physical adsorption does not occur, thus that relatively clean surfaces can be prepared on which to make accurate surface area measurements.

4) Physical adsorption equilibrium is achieved rapidly since no activation energy is required as in chemisorption. The exception here is adsorption in small pores where diffusion can limit the adsorption rate.

5) Physical adsorption is fully reversible, enabling both the adsorption and desorption

processes to be studied.

6) Physically adsorbed molecules are not restricted to specific sites and are free to cover the entire surface. For this reason surface areas rather number of sites can be calculated.

Using the nitrogen adsorption technique we can obtain pore information such as specific surface area which is based on BET (Brunauer, Emmett, Teller) theory, total pore volume, and pore size distribution which is based on Kelvin equation. The BET equation and pore size distribution work table will be presented in the following section.

BET theory

During the process of physical adsorption, at very low relative pressure, the first sites to be covered are the more energetic ones. Other high-energy sites lie between the horizontal and vertical edges of surface steps where the adsorbate can interact with surface atoms in two planes. On surfaces consisting of heteroatoms, such as organic solids or impure materials, there will be variations in adsorption potential depending upon the nature of the atoms or functional groups exposed at the surface.

Although more energetic sites are covered first as the pressure is increased, this does not imply that no adsorption occurs on sites of less potential. Rather, it implies that the average residence time of a physically adsorbed molecule is longer on the higher-energy sites. Accordingly, as the adsorbate pressure is allowed to increase, the surface becomes progressively coated and the probability increases that a gas molecule will strike and be adsorbed on a previously bound molecule. Clearly then, prior to complete surface coverage there will commence the formation of second and higher adsorbed layers. In reality, there

exists no pressure at which the surface is covered with exactly a completed physically adsorbed monolayer. The effectiveness of the Brunauer, Emmett and Teller (BET) theory [2,3] is that it enables an experimental determination of the number of molecules required to form a monolayer, despite the fact that exactly one monomolecular layer is never actually formed.

The Langmuir model [3] assumes monolayer adsorption and is thus limited to chemisorption and microporous solids. Brunauer, Emmett and Teller, in 1938, extended Langmuir's kinetic theory to multilayer adsorption. The BET theory assumes that the uppermost molecules in adsorbed stacks are in dynamic equilibrium with the vapor. This means that, where the surface is covered with only one layer of adsorbate, an equilibrium exists between that layer and the vapor, and where two layers are adsorbed, the upper layer is in equilibrium with the vapor, and so forth. Since the equilibrium is dynamic, the actual location of the surface sites covered by one, two or more layers may vary, but the number of molecules in each layer will remain constant.

For BET analysis, the adsorption data (V vs. P/P_0) is plotted in the linear form of the BET equation [3]:

$$1/ V[(P_0/P) - 1] = [1/ V_mC] + [(C-1)/ V_mC](P/P_0) \qquad (4\text{-}3)$$

where V_m and C is a measure of the adsorbent-adsorbate interactions.

Specific surface areas, S_{BET}

The success of kinetic theories directed toward the measurements of surface areas depends upon their ability to predict the number of adsorbate molecules required to exactly cover the solid with a single molecular. Equally important is the cross-sectional area of each

molecular or the effective area covered by each adsorbed molecule on the surface. The surface area then, is the product of the number of molecules in a completed monolayer and the effective cross-sectional area of an adsorbate molecule [3].

The determination of surface areas from the BET theory is a straight forward application of Eq.4-3. Nitrogen is usually employed as adsorptive and consequently adsorption measurements were carried out at the temperature of liquid nitrogen (77K). Data on the nitrogen isotherm between relative pressures (P/P_0) of about 0.05 and 0.35 were plotted in terms of the BET equation (i.e. BET plot, a plot of $1/ V[(P_0/P) - 1]$ vs. P/P_0), which should result in a straight line. The slope s and the intercept I of a BET plot are

$$s = (C-1) /V_mC \tag{4-4}$$

$$I = 1/V_mC \tag{4-5}$$

Solving the preceding equation for V_m, the volume adsorbed in a monolayer, gives

$$V_m = 1/(s + I) \tag{4-6}$$

and the solution for C, the BET constant, gives

$$C = 1 + s / I \tag{4-7}$$

From the slope (s) and the intercept (I), the specific surface area can be calculated by multiplying specific monolayer capacity by the cross-sectional area of a nitrogen molecule

$$S_{BET} (m^2/g) = n_m N_a a_m \tag{4-8}$$

where N_a is Avogadro's constant (6.02×10^{23} molecules/mole) and $a_m(N_2)$ is the average area occupied by a molecule of adsorbate in the completed monolayer and is taken to be 16.2×10^{-20} m^2 /molecule, n_m being expressed in moles of adsorbate per gram of adsorbent. Alternatively, if the monolayer capacity is expressed as the volume of gas is V_m

(milliliters/mole), then the specific surface area obtained by BET equation is

$$S_{BET} = (N_a a_m / 22414) V_m \qquad (4\text{-}9)$$

Based on the mathematical nature of the BET equation, reasonable results are obtained only when the constant C is greater than 10 [3]. In simple terms, the nitrogen isotherm should exhibit a distinct knee in the relative pressure range mentioned. C is proportional to the heat of adsorption of the adsorbate in the multilayer region. Further more, the BET plot should give a straight line with an intercept $I \geq 0$. The reproducibility of S_{BET} is about $\pm$ 5%.

Specific pore volume, Vp

As pointed out in Chapter 3, the total specific pore volume can be easily obtained by measuring the densities and adsorption isotherm. Various studies have shown that at saturation the liquid volume of different adsorbates, when measured on porous adsorbents, is essentially constant and is independent of the adsorbate. This constancy of adsorbed liquid at saturation is known as the Gurvitsch rule [3], and provides direct evidence that the pores are filled with liquid adsorbate at saturated vapor pressures.

To calculate the total pore volume it is necessary to measure the total adsorbate volume at a relative pressure close to 0.98. In general, a relative pressure as close to unity as possible should be chosen in order to include the large radii pores in the measurement. Then V_p is calculated as

$$V_p \text{ (ml/g)} = n_m V_m \qquad (4\text{-}10)$$

where n_m = amount adsorbed (moles per gram), and V_m = molar volume of liquid adsorbate (milliliters per mole) at the adsorption temperature.

Using the assumption that no surface other than the inner walls of the pores exists and cylindrical geometry, the average pore radius r_p can be calculated from the ratio of the total pore volume and the BET surface area from the following equation

$$V_p / S_{BET} = r_p /2 \qquad (4\text{-}11)$$

Kelvin equation and pore size distribution

Adsorption studies leading to measurements of pore size and pore-size distribution generally make use of the Kelvin equation [3] which relates the equilibrium vapor pressure of a curved surface, such as that of a liquid in a capillary or pore, to the equilibrium pressure of the same liquid on a plane surface

$$\ln(P/Po) = -2\gamma V_m \cos\theta/rRT \qquad (4\text{-}12)$$

where P is the equilibrium vapor pressure of the liquid contained in a narrow pore of radius r, and Po is the equilibrium pressure of the same liquid exhibiting a plane surface. The terms γ and V_m are the surface tension and molar volume of the liquid, respectively, and θ is the contact angle with which the liquid meets the pore wall.

In a pore the overlapping potentials of the walls more readily overcome the translational energy of an adsorbate molecule so that condensation occurs at a lower pressure in a pore than that normally required on an open or plane surface. Thus, as the relative pressure is increased, condensation will occur first in pores of smaller radii and will progress into the larger pores until, at a relative pressure of unity, condensation will occur on those surfaces where the radius of curvature is essentially infinite. Conversely, as the relative pressure is decreased, evaporation will occur progressively out of pores with decreasing radii. Equation 4-12 is the working equation for pore size analysis in adsorption unless more

specific information is available regarding the pore geometry and the wetting angle.

Taking 8.85 erg/cm^2 as the surface tension and 34.6 cm^3/mole as the molar volume of liquid nitrogen at 77 K, assuming a zero wetting angle, the Kelvin equation can be written as

$$r_k = 4.15/\lg(Po/P)\ (Å) \qquad (4\text{-}13)$$

The term r_k indicates the radius into which condensation occurs at the required relative pressure. This radius, called the Kelvin radius or the critical radius, is not the actual pore radius since some adsorption has already occurred on the pore wall, prior to condensation, leaving a center core of radius r_k.

If the depth of the adsorbed film when condensation or evaporation occurs is t, then the actual pore radius r_p is given by

$$r_p = r_k + t \qquad (4\text{-}14)$$

It means evaluating t is required if the pore radius is to be determined.

The experimental formula is described closely by the Halsey equation [3]. For nitrogen it can be written as

$$t = 3.54\ [5/2.303 \lg (Po/P)]^{1/3} \qquad (4\text{-}15)$$

A procedure to calculate pore size was proposed by Wheeler in 1945, and developed by a number of workers, including Shull, Barrett, Joyner and Halenda (BJH). Pierce method [4] appears to combine reasonable simplicity with a necessary degree of precision, and will now be described. This procedure involving only wall area and based on the cylindrical pore model was put forward by Pierce in 1953. It is the numerical integration method of Pierce and modified by Orr and Dalla Valle with regard to calculating the depth of the adsorbed

film. It includes the work sheet of Table 4-1, and the explanation of each column.

1) (P/Po): Relative pressures data obtained directly from the isotherm.

2) V(cc/g): Adsorbed volumes from a adsorption isotherm.

3) r_k (Å): Kelvin radius, calculated from the Kelvin equation assuming a zero wetting angle. If nitrogen is the adsorbate, Eq. (4-13) can be used.

4) t (Å): Film depth t, calculated using Eq. (4-15), the Halsey equation.

5) r_p (Å): Column 5 gives the pore radius r_p obtained from Eq. (4-14).

6) r_k (avg): Average r_k prepared by calculating the mean value in each decrement from successive entries.

7) r_p (avg): Average r_p prepared by calculating the mean value in each decrement from successive entries.

8) Dt (Å): Change in film depth, calculated by taking the difference between successive values of t.

9) DV(cc/g): Change in adsorbed volume between successive P/Po values.

10) DS (m^2): ΔS_p, surface area of the pore walls corresponding to the decremental volumes ΔV_p. It is calculated by

$$\Delta S_p = 31.2\ \Delta V_p / r_p\ (avg) \qquad (4\text{-}16)$$

It is referring to the cylinder pore assumption (i.e. $\Delta S_p = 2\ \Delta V_p / r_p$ (avg)) and the converting coefficient. The most direct way to convert ΔV to the volume of liquid ΔV_l is by calculating the moles of gas, and then multiplying the liquid molar volume. For nitrogen at standard temperature and pressure this is given by $\Delta V_l = (\Delta V/22.4 \times 10^3) \times 34.6 = \Delta V\ (1.54 \times 10^{-3})$ cc.

11) Sum (DS): Values obtained by the summation of all the preceding lines of column (10) and used in the manner for the calculation of ΔV_f. The total pore volume is also calculated by summing all the individual decrements ΔV_p.

12) DV_f: Values of ΔV_f represent the amounts adsorpted from the film on the walls. It is calculated from the area of the walls covered with film and the diminution in thickness of the film, using the expression

$$\Delta V_f = 0.064\ \Delta t\ \text{sum}\ (\Delta S_p) \qquad (4\text{-}17)$$

13) DV_k: Volume of the "inner cylinder"

$$\Delta V_k = \Delta V - \Delta V_f \qquad (4\text{-}18)$$

14) DV_p: Volume of the actual pore ΔV_p related to ΔV_k by the expression

$$\Delta V_p = \Delta V_k\ [r_p\ (\text{avg}) / r_k\ (\text{avg})] \qquad (4\text{-}19)$$

If the utmost rigor were used, it would be correct to modify the area contributed by previously emptied pores since their statistical thickness diminishes with each successive decrement. However, this procedure would be cumbersome and of questionable value in view of the many other assumptions that have been made. Nevertheless, the BJH method attempts to make this modification by introducing an average inner core based on its variation with each decrement of relative pressure.

§ 4. 2 Experiment

Nitrogen sorption measurements were carried out at 77K. Sorption isotherms are usually measured in the range $0.05 < P/P_0 < 1.0$. With the aid of these isotherms, the following pore structure parameters can be calculated: the specific pore volume V_p of the

1 P/P0	2 V(cc/g)	3 rk (A)	4 t (A)	5 rp (A)	6 rk(av)	7 rp(av)	8 Dt(A)	9 DV(cc/g)	10 DS(m2)	11 Sum(DS)	12 DVf	13 DVk	14 DVp
0.9783	880.66	0.051192	434.5113	21.37767	455.8889	309.893	291.7237	6.416691	366.3	93.37868	93.37868	38.34765	327.9523
0.938	514.36	0.029413	148.9361	14.96098	163.897	132.3993	118.6339	2.391065	115.06	47.02509	140.4038	21.48573	93.57427
0.8977	399.3	0.021976	88.33173	12.56991	100.9016	86.9906	75.12276	1.404131	55.88	31.00795	171.4117	15.40381	40.47619
0.8573	343.42	0.017494	61.91379	11.16578	73.07957	65.20552	54.52485	0.970231	36.685	25.94133	197.353	12.2546	24.4304
0.8169	306.735	0.014545	47.13592	10.19555	57.33147	52.2499	42.41997	0.731234	26.95	23.28671	220.6398	10.32572	16.62428
0.7766	279.785	0.012425	37.70402	9.464315	47.16834	43.58682	34.41543	0.585841	19.965	20.12312	240.7629	9.027127	10.93787
0.7362	259.82	0.010741	31.12684	8.878473	40.00531	37.34585	28.71019	0.485621	17.765	21.3684	262.1313	8.146967	9.618033
0.6959	242.055	0.009454	26.29353	8.392853	34.68639	32.6165	24.43189	0.416481	15.62	21.76215	283.8934	7.567112	8.052888
0.6555	226.435	0.008403	22.57025	7.976372	30.54662	28.8946	21.09959	0.362734	12.705	19.51746	303.4109	7.043678	5.661322
0.6153	213.73	0.007483	19.62894	7.613638	27.24258	25.87596	18.42484	0.325041	11.715	20.47025	323.8811	6.737575	4.977425
0.5749	202.015	0.006694	17.22075	7.288597	24.50934	23.36064	16.2192	0.294324	10.56	20.49528	344.3764	6.486922	4.073078
0.5345	191.455	0.005997	15.21766	6.994273	22.21194	21.23088	14.37139	0.269563	9.955	21.72666	366.1031	6.316022	3.638978
0.4942	181.5	0.005383	13.52511	6.72471	20.24982	19.39426	12.79516	0.251225	9.295	22.34704	388.4501	6.245654	3.049346
0.4538	172.205	0.004825	12.0652	6.473485	18.53869	17.78377	11.42843	0.23629	8.745	23.02736	411.4775	6.22258	2.52242
0.4134	163.46	0.004311	10.79166	6.237196	17.02886	16.35537	10.23031	0.224263	8.415	24.42602	435.9035	6.256443	2.158557
0.3731	155.045	0.003839	9.668949	6.012933	15.68188	15.07022	9.165497	0.216421	8.47	27.68064	463.5841	6.421077	2.048923
0.3327	146.575	0.003402	8.662045	5.796512	14.45856	13.89856	8.207263	0.210436	8.305	29.69216	493.2763	6.643404	1.661596
0.2924	138.27	0.002989	7.75248	5.586076	13.33856	12.81611	7.334312	0.208565	8.25	32.01723	525.2935	7.01171	1.23829
0.252	130.02	0.002591	6.916144	5.377511	12.29365	11.80092	6.528017	0.209221	8.525	36.9519	562.2454	7.528562	0.996438
0.2117	121.495	0.00221	6.13989	5.168289	11.30818	10.83191	5.771439	0.215636	9.075	44.18689	606.4323	8.369182	0.705818
0.1713	112.42	0.001839	5.402988	4.952654	10.35564	9.883869	5.045615	0.228798	9.625	50.54587	656.9782	9.620187	0.004813
0.1309	102.795	0.001465	4.688241	4.723855	9.412097	8.924228	4.328112	0.255478	11.385	70.52598	727.5042	11.89512	-0.51012
0.0905	91.41	0.001089	3.967982	4.468378	8.43636	7.887987	3.577161	0.315103	14.025	94.27436	821.7785	16.57246	-2.54746
0.0502	77.385	0.000683	3.18634	4.153275	7.339615	6.496204	2.623649						
0.0098	52.195	0.00019	2.060959	3.591835	5.652794								

Table 4-1 Pore size distribution work table from Pierce method.

adsorbent (at P/Po = 0.98), V_p as function of the mean pore diameter D, the specific surface area S_{BET} of the adsorbent (at $0.05 < P/Po < 0.3$), S_{BET} as a function of D.

The most common mode of the sorption techniques is the volumetric [5,6]. A sample, placed in a small-diameter glass tube, is outgassed in a helium atmosphere. After cooling, a stream of gas composed of nitrogen and helium passes through the tube and through the cell of a thermal conductivity detector. After a constant detector baseline is attained the sample is cooled to the temperature of liquid nitrogen, adsorbing a certain amount of gas depending on its partial pressure. When equilibrium has been established, the bath of liquid nitrogen is removed, and the glass tube is thermostated at room temperature. The adsorbed nitrogen is desorbed. Finally, the volume of gas adsorbed per gram of adsorbent can be output as a function of the relative pressure.

Measurement of the surface area is classically performed following the BET method. The method first involves the removal of preadsorbed gases and vapors from the surface of the solid. Then the solid is typically cooled to the boiling point of a chosen adsorbate gas. The surface is then incrementally exposed to higher partial pressures of the adsorbate gas until the entire surface is covered by these molecules. The extent of the surface of the solid can be calculated by multiplying the number of molecules of adsorbate gas required to form a monolayer times the area covered by each adsorbate gas molecule.

The apparatus used was a Micromeritics Gemini 2360 surface area analyzer: a fully automatic nitrogen gas adsorption apparatus that can be programmed to measure gas adsorption isotherms. The analyzer consists of two tubes of matched internal volume. One contains the sample, while the other is empty. These two tubes are joined by servo valves

as seen in Fig. 4-1.

In operation, a prepared sample is placed in the sample tube (right-hand). The balance tube (left-hand) remains empty. A vacuum is pulled on the manifold system to expel residual gas and vapors before opening the tubes to the system. When a sufficient vacuum is obtained (usually a few minutes or less), the valves to the tubes are opened, and the system is brought into volumetric balance with an adjusting piston incorporated into the manifold. From this point on, any differences observed between the sample tube and the balance tube are due strictly to the presence and influence of the sample itself.

The sample and balance tubes are immersed in the coolant bath by raising the platform that holds the coolant bath (nitrogen adsorption was carried out at 77K). When thermal equilibrium is achieved, the adsorbate gas is admitted into the manifold at the first designed relative pressure. This gas has equal access to both tubes. Because there is no sample in the balance tube, no adsorption of the gas takes place. In the sample tube, however, the sample begins to adsorb the gas in direct proportion to its surface area.

As the sample adsorbs gas, the gas pressure in the sample tube drops. This unbalances the manifold and servo valve circuit. The servo valve circuit then causes more gas to be brought into the manifold in an attempt to bring the gas pressure back into a fully balanced condition. The amount and rate of new gas introduced into the manifold is in exact proportion to the amount of gas that has been adsorbed onto the surface of the sample. This action continues until the highest relative pressure requested has been reached. In every case, the instrument responds exactly to, and only to, the amount and rate at which gas is adsorbed by the sample.

Any deviation of the adsorbing gas from the ideal gas behavior in the sample tube is exactly duplicated in the balance tube. By cancellation of the nonideal-gas behavior in the sample tube from that observed in the balance tube, this error is completely nulled. The same is true for any thermal gradients in the coolant bath. Virtually all of the deviations from ideal conditions in the sample tube are exactly duplicated in the balance tube and are subtracted from the experimental results. At the same time, the delivery rate of the gas into the sample tube is controlled by the rate at which the sample can adsorb the gas onto the surface. A rapidly acting servo device continuously restores the pressure balance between the tubes by admitting more gas into the sample side. The result is that the instrument maintains the pressure constant over the sample, while varying the rate of gas delivery to match the sample adsorption rate.

A prerequisite for sorption measurements is the outgassing of the adsorbent, which involves the exposure of the adsorbent to a vacuum. For general purposes, a vacuum of the order of 10^{-2} -10^{-3} Pa is sufficient. Outgassing is often carried out at elevated temperatures, in order to accelerate the removal of humidity and previously adsorbed gases. The temperature, however, may be a critical parameter concerning pore structure and surface composition. Outgassing was completed by heating the sample to 60C and sustaining it for at least 2 hours at Micromeritics FlowPrep 060. After outgassing, the sample was cooled under vacuum and the tubes were back-filled with helium before being transferred to the analysis ports.

§ 4. 3 Density measurement

Apparatus used to measure solid volumes are often referred to as pyknometers or

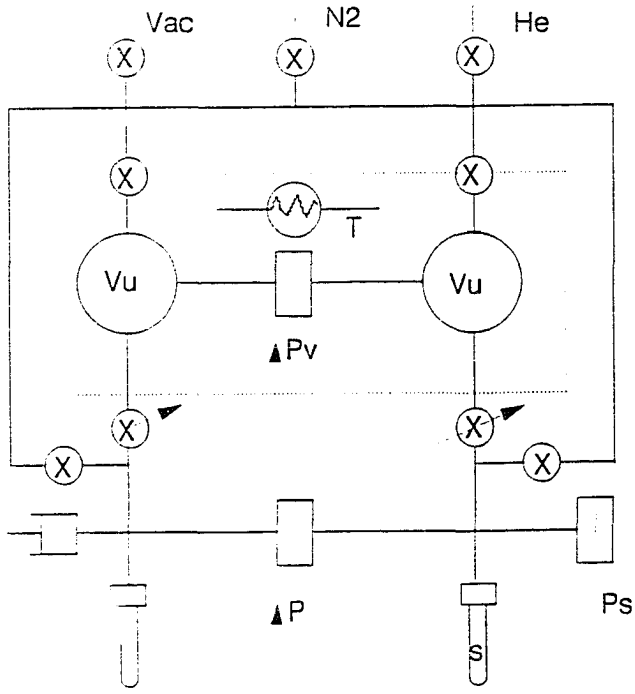

Figure 4-1 Diagram of the gas adsorption analyzer showing the connection of the two matched tubes by the servo valve mechanism.

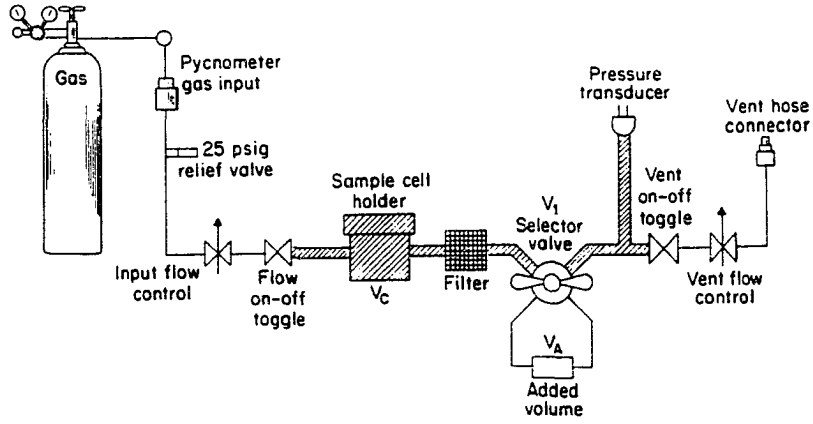

Figure 4-2 A schematic diagram of the pycnometer for skeleton density measurement.

pycnometers after the Greek "pyknos" meaning thickness or density. Once the sample volume and mass have been determined, the density is readily calculated.

The recent availability of economical, stable and high-resolution pressure transducers has led to the development of a new type of helium pycnometer which offers extreme simplicity of operation along with great speed and accuracy (Micromeritics, AccuPyc 1330). A schematic diagram of this pycnometer is shown in Fig.4-2. The volume V_c in the shaded area is the sample cell. After purging the system with helium and bringing all volume to ambient pressure, the sample cell is pressurized to P_2, about 15 psi above ambient. Valve V_1 is opened to connect the additional volume V_A to that of the cell. Consequently, the pressure drops to a lower value P_1 in the cell while increasing from ambient to P in the added volume. Using P_1 and P_2, the sample volume V_s is calculated from

$$V_s = V_c + V_A / (1 - P_2/P_1) \qquad (4\text{-}20)$$

The above equation assumes ideal gas behavior which is closely obeyed at pressures near ambient at room temperature by both pure helium and nitrogen. However, helium is preferred because of its smaller size. Our skeletal density d_s was measured by helium pyknometry at 19.5 psi and a rate of 0.005 psi/min.

§ 4. 4 Results and Discussion

One must be cautious in interpreting absolute physisorption data derived from such highly structured aerogels [7]. Fig. 4-3 shows the N_2 adsorption isotherm of the aerogel, and Fig. 4-4 is a BET plot from which specific surface area can be drawn following the procedure of section one (Eq. 4-6 to 4-9). The relative pressure range used for BET analysis was chosen to give the best linear correlation in the BET function, which is $0.05 < P/P_0 < 0.3$.

Total pore volume V_{TP}, was obtained from the N_2 adsorption isotherm at $P/P_0 = 0.98$. Table 4-2 lists the composition of four samples and some of the structural parameters.

Table 4-2 The composition of the starting materials from which the four different TiO_2 aerogels were made, are presented along with structural parameters obtained using nitrogen adsorption and He pycnometry[a].

Samples	Composition	d_s	V_{TP}	ϕ	d_b	S/M
A	1:20:4:0.08	3.62	0.62	0.69	1.11	201
B	1:20:4:0.08	3.01	1.50	0.82	0.55	465
C	1:20:5:0.08	3.24	1.61	0.84	0.52	426
D[b]	1:20:2:0.08	2.70	1.37	0.79	0.58	447

[a] The composition is given in the ratio of $Ti(OR)_4/ETOH/H_2O/HNO_3$. ϕ is the porosity; $d_s(g/cm^3)$ is the skeletal density; d_b (g/cm^3) the bulk density and V_{TP} (cm^3/g) the total pore volume. The simple relationships among these parameters are $\phi = V_{TP}/(V_{TP}+(1/d_s))$ and $d_b = d_s(1-\phi)$. The specific surface area is S/M (m^2/g).

[b] Sample D was washed with water during gelation time.

The pore size distributions derived from the adsorption isotherm (desorption is not available in the instrument) using the Pierce method [3] are illustrated in Fig. 4-5 and 4-6. They are in cumulative (volume versus diameter) and differential form respectively. All samples show pronounced meso- to macro porosity with only little microporosity.

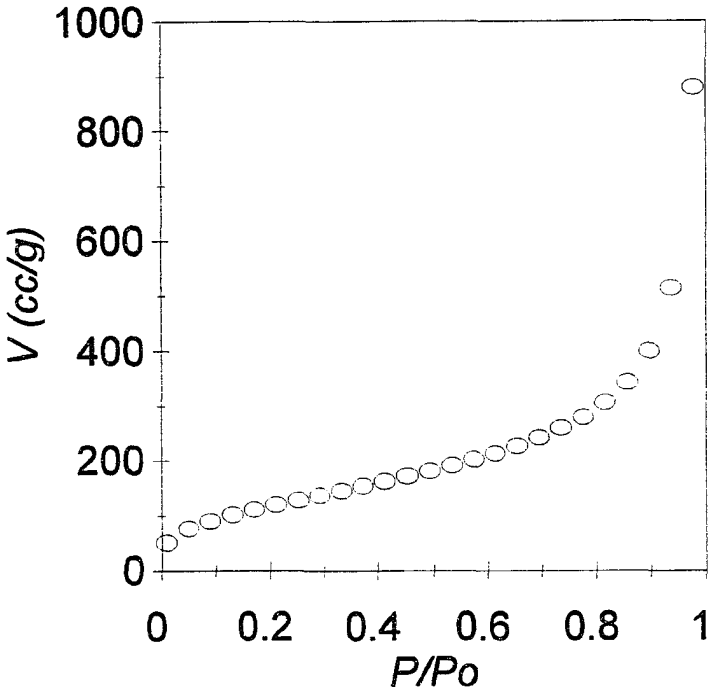

Figure 4-3 N_2 adsorption isotherm of the TiO_2 aerogel sample D.

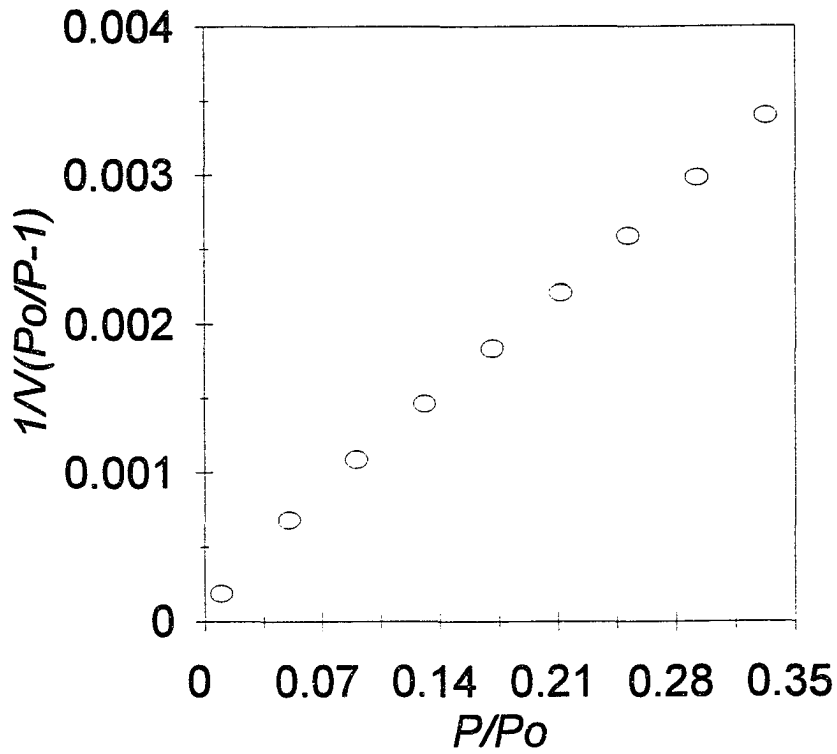

Figure 4-4 BET plot from Figure 4-3.

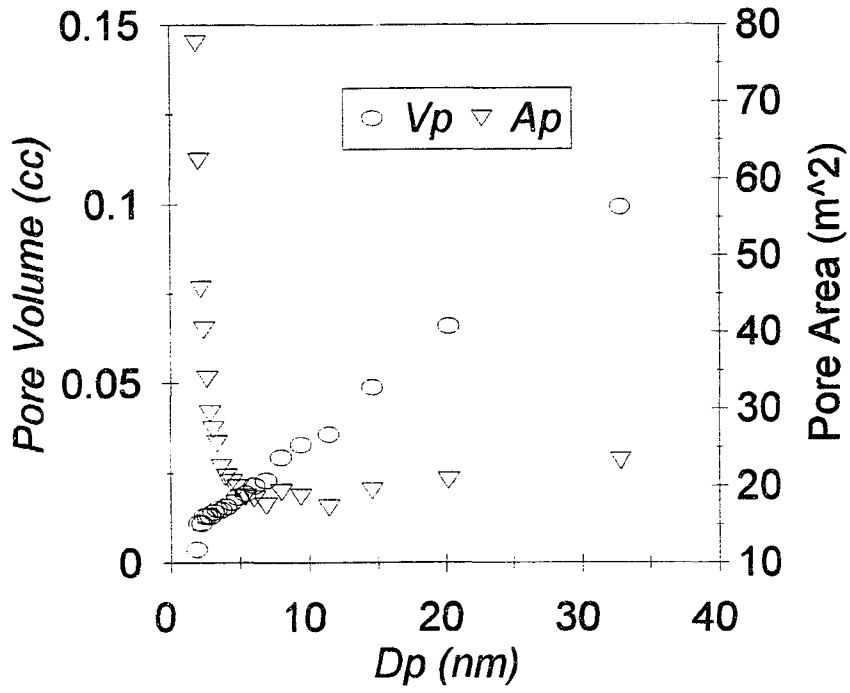

Figure 4-5 Pore size distribution in cumulative (volume or area versus diameter)form of sample D obtained from the nitrogen adsorption analysis.

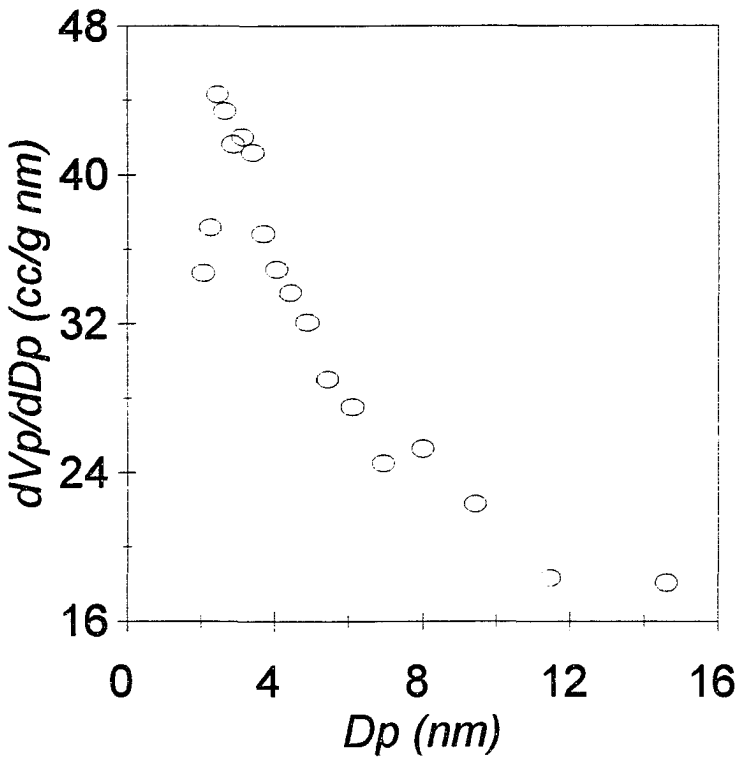

Figure 4-6 Pore size distribution in differential form of sample D.

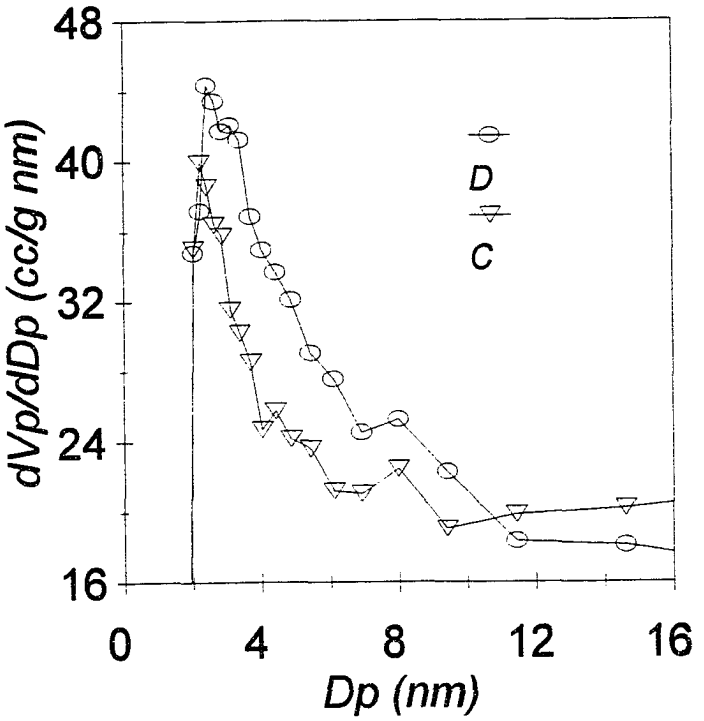

Figure 4-7 Pore size distribution tailored by water content.

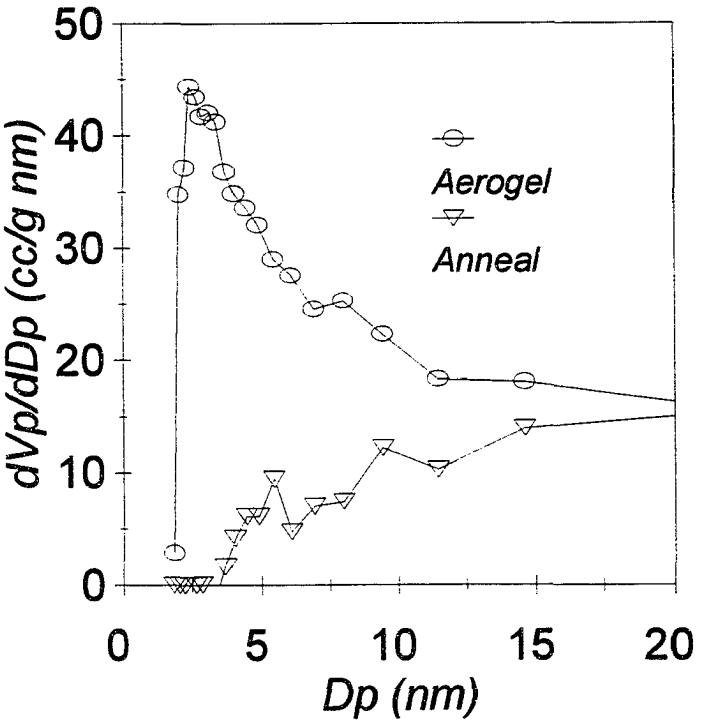

Figure 4-8 Pore size distribution tailored by annealing. (a) is the original aerogel, (b) is after 2 hrs 400 C annealing.

Moreover, it emerges from Table 4-2 that the aerogel with lower water content (sample D) has larger surface area (447 m^2/g), smaller total pore volume (1.37 cm^3/g) and broader pore size distribution which was shown in Fig. 4-7 comparing it with sample C. On a molecular scale water can cause dissolution, reprecipitation, depolymerization, repolymerization, alkoxylation and enhanced syneresis (network densification) leading to crystallographic and chemical restructuring phenomena in such materials. Water content of sample A is not consistent with its morphology parameter due to supercritical drying fast purge. The pore size determined from pore size distribution maxima (D_m -nm) is listed as Table 4-3. Average pore size information can be provided.

Table 4-3 The average pore size.

Samples	D_m -nm
A	2.52
B	2.26
C	2.26
D	2.46

In order to tailor pore morphology, the sample D was chosen to show comparison. Fig. 4-8 (a) is the original aerogel; (b) is after 2 hr 400 C annealing. The annealing diminishes most small pores and makes macropores the major contributor.

The density of anatase is 3.8 g/cm^3, whereas the skeletal density measured by helium pyknometry, is 2.7 g/cm^3. This difference can be explained by incomplete penetration of the helium into the mesoaggregates. Higher pressure and longer equilibration time might allow the helium to penetrate into the mesoaggregates, then increase the skeletal density measured.

Thus the porosity of the nanoparticles can be calculated from the two densities i.e., 29%. This is very close to the theoretical porosity of hexagonal close packing spheres 26% [8]. If we now take the BET total surface area (447 m^2/g) and assume that the entire surface area originates from the nanoparticles, the average diameter of the nanoparticles is calculated to be 3.5 nm. Or The total surface area of the aerogels is attributed to the sum of the surface of the nanoparticles.

Briefly, nitrogen adsorption is a very effective way to obtain average information like total surface area. The concept is simple and the experiment is accountable. It is a method which focus more on pores rather than particles.

CHAPTER 5. X-ray Powder Diffraction

Beginning with the pioneering experiments conducted in 1913 and 1914, X-ray powder diffraction has been an important tool for studying materials. Today powder diffraction is a standard technique in many laboratories which is capable of providing a wealth of information in areas such as: phase identification, crystal structure analyses, quantitative analyses, particle size and strain measurements, etc.. We are going to provide a brief description of the principle of diffraction, describe the instrumentation and show the experimental results.

§ 5. 1 Introduction

Scattering by points:

A single electron scatters as a point source, with the scattering amplitude being identical in all directions. The magnitude of scattering in a given direction (See Fig.5-2) is described in units relative to the scattering from a single electron. Intensity is the quantity measured by the diffraction device, and it is given by the square of the magnitude for centrosymmetric arrangement of scattering points.

The atoms are considered point sources of scattering even though they have a finite volume and partially destructive interference takes place between the scattering of electrons within the atoms. At a diffraction angle of zero degree, all scatterings are in phase, so the scattering amplitude f_0 is equal to the number of electrons in the atom or the atomic number minus the positive charge or plus the negative charge for an ionic form of the atom.

Atoms in a crystal are not spatially fixed. Thermal effects cause vibration around their balancing positions. So atomic scattering factors are given by means of the Debye-

Waller equation [1],

$$f = f_0 \exp(-C\sin^2\theta / \lambda^2) \qquad (5\text{-}1)$$

in which f_0 is the atomic scattering factor at a temperature of absolute zero, and C is a parameter that is related to the mean amplitude of vibration normal to the diffraction direction for which f is applied. The temperature effect causes the amplitude of scattering to decrease monotonically with high diffraction angles, and the larger the value of C, the more rapid the diminution.

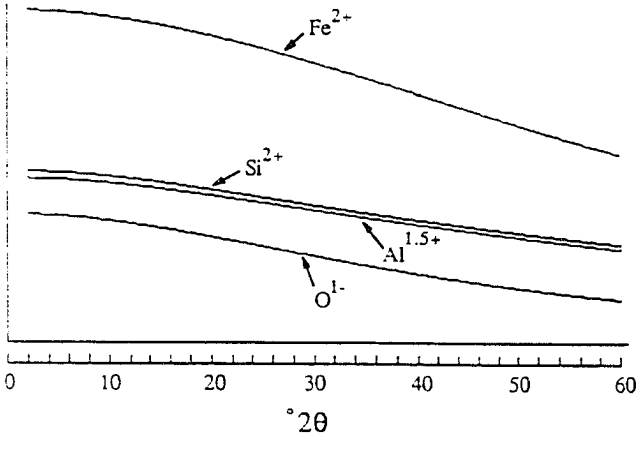

Figure 5-1 Atom scattering factors for Fe, Si, Al and O (CuKα).

Figure 5-1 represents the scattering factors [1] for Fe, Si, Al, and O that have been corrected for thermal vibration using C = 1.5 for metals and C = 2.0 for oxygen. The scattering magnitudes are expressed in electron scattering units versus the diffraction angles with incidental CuK_α X-rays. The scattering factors decrease with increasing 2θ because of destructive interference within the atoms and thermal effects. The curves in Fig. 5-1 show that Fe has a strong influence on peak intensities of silicate diffraction patterns because of its very different scattering factor compared to those elements that it substitutes, such as Al

and Si.

Summation of amplitudes:

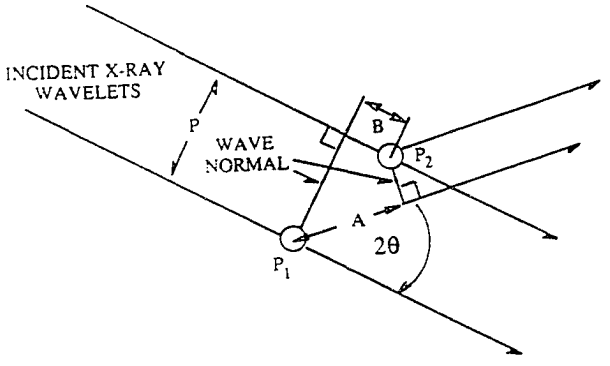

Figure 5-2 Scattering from two points.

Figure 5-2 illustrates the procedure for adding amplitudes from scattering centers. In this case, atoms P_1 and P_2, whose scattering factors are f_1 and f_2, are separated from each other by P which is measured as their separation (Å) in a direction normal to that of the incident X-ray wave. 2θ is the angle between the incident and the diffracted waves whose wavelength is λ (Å). The wave normal from P_1 connects points of equal phase for the two incident wavelets, and the wave normal from P_2 connects points of equal phase for the scattered wavelets. A is the distance that the wavelet scattered from P_1 must travel to coincide with the wave normal of the diffracted wave that passes through P_2, and B is the distance that P_2 lies from the incident wave normal. Because $B \neq A$ there is a phase difference between the scattering centers which causes the magnitude of scattering to be less than $f_1 + f_2$. The path difference, for the diffraction angle 2θ, is equal to (A - B). If $(A - B)/\lambda$ is integral, then the scattered wavelets are perfectly in phase, and if it equals half integral, the scattering is out of phase and the resulting magnitude is zero. For the general case, we define the phase angle, ϕ, as the path difference times $2\pi/\lambda$. So for this example,

$$\phi = 2\pi (A - B)/\lambda \qquad (5\text{-}2)$$

The expression for adding amplitudes of scattered wavelets is given by

$$F = f_1 \exp(i\phi_1) + f_2 \exp(i\phi_2) \qquad (5\text{-}3)$$

where F is the resulting amplitude. We have selected P_1 as the origin for this calculation, so $\phi_1 = 0$, and the result is $F = f_1 + f_2 \exp(i\phi_2)$.

The exponential notations are cumbersome, and Euler's identity is used to convert them to their trigonometric forms. The intensity I is equal to F times its complex conjugate, thus

$$I = \{f_1 + f_2 \cos[2\pi (A - B)/\lambda]\}^2 + \{f_2 \sin[2\pi (A - B)/\lambda]\}^2 \qquad (5\text{-}4)$$

The Bragg law:

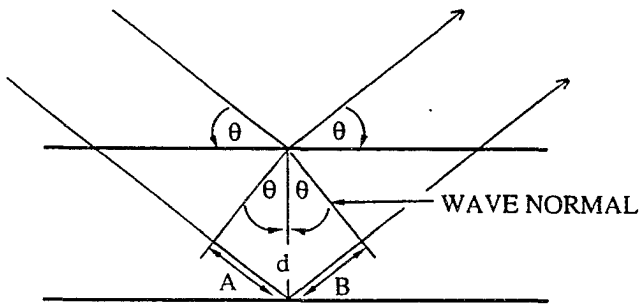

Figure 5-3 The Bragg law for parallel planes.

The diffraction principle developed by W. L. Bragg is the one most general and powerful in diffraction theory. And it is one of the most intuitive and easy to understand. Fig. 5-3 shows the diffraction from two scattering planes that are separated by a distance d (Å) and incidented by X-radiation of wavelength λ (Å) at an incident angle θ. The experimental parameter 2θ is the angle between the diffracted and undeviated X-ray waves. The diagram shows only two scattering planes, but implicit here is the presence of many

parallel, identical planes, each of which is separated from its adjacent neighbor by the spacing d. The locations of the planes are defined by a periodic function whose "wavelength" is related to the dimensions of the unit cell and the orientation of the plane *hkl*. The wave normals connect points of identical phase for the incident and diffracted waves. The distance (A+B) must equal a whole number of wavelengths for total constructive reinforcement to occur between the scattering from these planes, so we need to calculate the value of θ, for a given d, for which $(A+B) = n\lambda$, where n is an integral. The direction of d is normal to the planes, and the wave normal is normal to the wavelets, so the angles opposite A and B are also θ. Therefore $A+B = 2d\sin\theta$. Constructive interference occurs when $(A+B) = n\lambda$, and the Bragg law [2] states

$$n\lambda = 2d\sin\theta \qquad (5\text{-}5)$$

The integer n refers to the order of diffraction.

Diffraction from a set of reflecting planes:

The derivation given above for the Bragg law does not explain why crystals produce such sharp diffraction phenomena. Suppose that θ is increased by a small amount that leads to an increase in the quantity (A+B) by δ, and that the amplitude of the scattering for each of the planes is identical. Thus the phase ϕ between the two planes is equal to $(2\pi/\lambda)(A+B+\delta)$. The cosine of ϕ is very close to the cosine of the phase angle for the Bragg condition. Hence, if δ is small, only a slight reduction of magnitude results and significant intensity occurs at an angle different by $\pm\delta$ from the Bragg angle resulting in a broad diffraction peak. But there are additional, parallel planes, separated from the first by 2d, 3d, 4d etc. Consequently, for a thick crystal and a finite value of δ, some planes will lie at the

distance (nd) that is exactly out of phases with respect to the top plane of Fig. 5-3, and the diffracted intensity will be zero at the angle slightly different from θ. The same argument can be made for any plane in a thick crystal. Ideally, an infinitely thick perfect crystal would produce peaks with no width at all. In practice, however, perfect crystals are very rare, and even they produce reflections that are broadened by the finite width of the incident X-ray spectral distribution and other instrumental defocusing effects. If a crystal is thin, however, widely separated out-of-phase planes are precluded for a given value of δ. Consequently, thinner diffracting domains produce broader peaks. The relation between line breadth and crystal thickness is given by the Scherrer equation [2,3], which follows from the Bragg Law.

$$B = K\lambda / T\cos\theta \qquad (5\text{-}6)$$

where B is the width (in radians) of a reflection measured at half of its height; K is a crystal shape constant near unit and T is the thickness (Å) of the coherent diffracting domain along a direction normal to the diffracting plane *hkl*. Instrumental broadening effects must be removed from the experimental diffraction profile to yield the pure diffraction breadth B, in order to apply this equation to practical measurements.

Unit cell and structure factor:

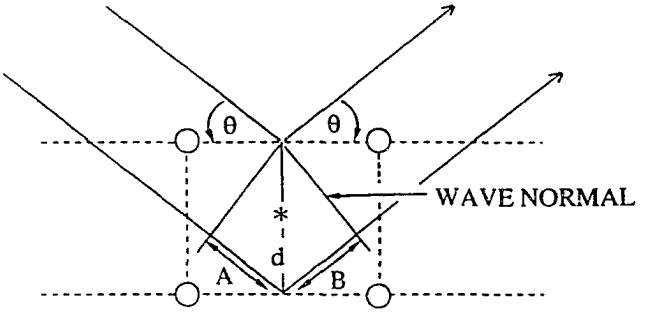

Figure 5-4 The Bragg law for the unit cell.

Figure 5-4 is a modified version of Figure 5-3. Atoms have been substituted by the

atomic planes, and the atomic positions define a primitive, two-dimensional orthogonal unit cell with Z parallel to the page. This arrangement is suitable for describing the diffraction series with *00l direction*. The structure factor, represented by symbol F, is used to portray the amplitude of scattering from the unit cell in the direction θ, which lies in a plane normal to the atomic plane *hkl* [4]. We can imagine the unit cell as a single point in space, but unlike an electron, a point has a complicated directional scattering distribution. The location of the "point-source" unit cell in space is fixed by the origin that is selected for calculations of scattering amplitude. The phases of scattering from all atoms are referred to that origin at which the phase angle is defined as zero. The reference point on Fig. 5-4 for calculating the structure factor F(*00l*) is located at the asterisk. That location is a center of symmetry. Then the amplitudes are summed as follows if each atom has same atomic scattering factor: for the top atomic plane, the phase angle with respect to the center is $(2\pi/\lambda)2z\sin\theta$, where z is the atomic coordinate in the Z direction and is equal to d/2 where d(*001*) = d. For the bottom atomic plane, ϕ is the same except that z = -d/2. F*(001)*, then, is equal to f $\cos[2\pi d\sin\theta/\lambda]$.

Equation (5-7) applies to a centrosymmetric unit cell with any number of atoms

$$F(00l) = \Sigma_j\ n_j\ f_j \cos\ (2\pi l z_j\ /d) \qquad (5\text{-}7)$$

where z_j is the distance in Å of each atomic layer from the center of symmetry; n is the number of atoms at z_j plane, and f_j is the scattering magnitude of each atom. Equation (5-7) is easily generalized into three dimensions by the expression

$$F(hkl) = \Sigma_j\ n_j\ f_j \cos\ [2\pi\ (hx_j + ky_j + lz_j)] \qquad (5\text{-}8)$$

where xj, yj and zj refer to the three dimensional locations of each atom expressed as

fractional coordinates of the unit cell in the directions of X, Y, and Z.

§ 5. 2 Instrumentation

Powder diffraction measurements are made by causing a beam of X-radiation to fall onto a suitably prepared specimen and measuring the angles at which a specific characteristic X-ray wavelength is diffracted. The diffraction angle θ can be related to the interplanar spacing d by the Bragg law. Figure 5-5 is the schematic diagram of X-ray powder diffractometer. It includes X-ray source, divergence slit, sample stage, receiving slit and detector. Figure 5-6 is the geometrical relation of the X-ray diffractometer. There are two instrument parameters which influence the X-ray source, i.e., focal spot dimension of the tube and take-off angle.

The maximum rating of the X-ray tube depends mainly on the ability of the anode to dissipate heat. Thus the specific loading, watts/mm^2, of the anode is an important parameter. Fine-focus tubes are usually employed for powder diffractometry depending upon the resolution/intensity compromisation required. It is not generally possible to choose just any combination of mA and kV for a given X-ray tube because the filament temperature must stay within certain limits to ensure optimum tube life, contamination rates, etc.. The acceptable ranges of kV and mA are usually defined by a power-rating curve supplied with the X-ray tube. The effective intensity of the source depends both on the receiving slit and the focal spot characteristics of the X-ray tube. The take-off angle of the X-ray tube (Fig. 5-6) can be important in the selection of tube conditions owing to the finite depth within the anode at which the characteristic X-radiation is produced. Also because the take-off angle determines the effective width of the X-ray beam, it influences the peak and background

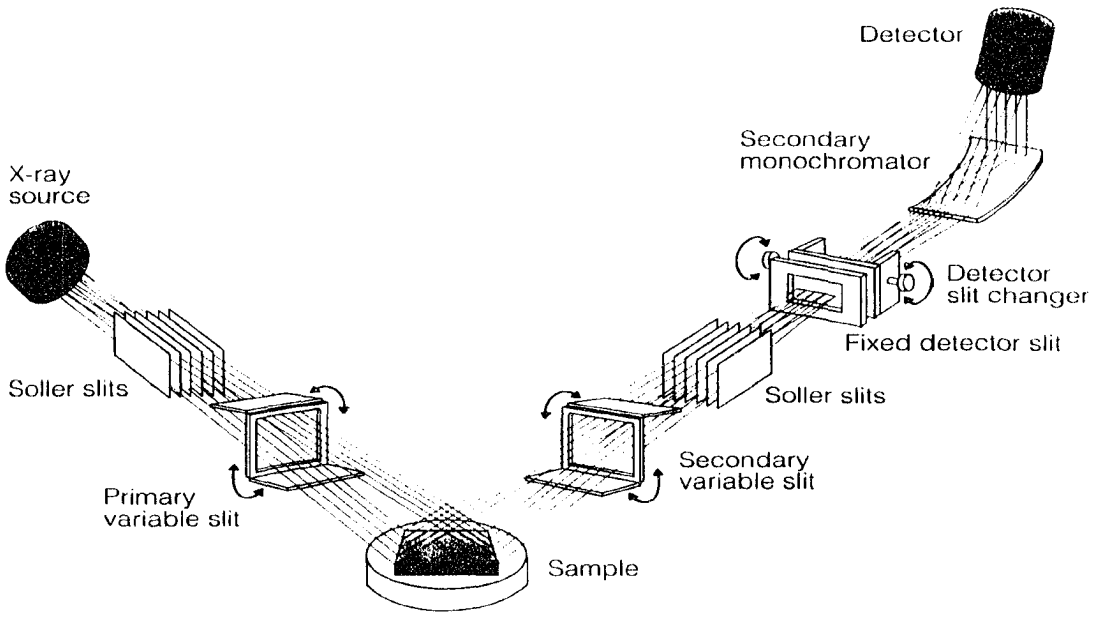

Figure 5-5 A schematic diagram of X-ray powder diffractometer.

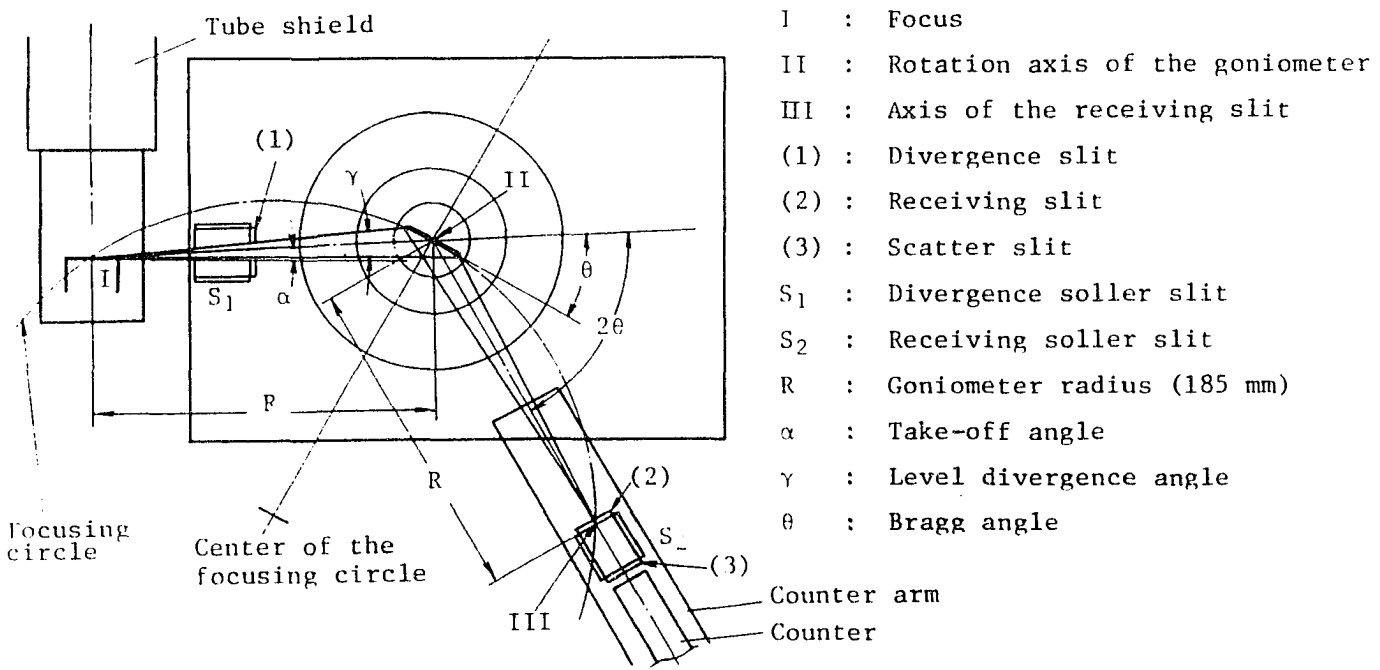

Figure 5-6 Geometry relation of the X-ray diffractometer.

response obtained with the diffractometer. A small value of α will give a narrow beam and a reasonable high intensity, but this intensity will be very sensitive to the surface roughness of the anode. The optimum size of the receiving slit is typically twice as large as the projected beam width because of the broadening of the beam due to axial divergence. As an example, the beam width at the receiving slit is about 0.2 mm for a fine-focus copper target tube with focal spot dimension of 12×0.5 mm^2, a take-off angle of 6° and Soller collimator giving $\pm2.5^\circ$ beam divergence.

The size of the receiving slit (RS) affects both the width and intensity of a given line profile. In general, as the intensity increases, the resolution of the lines decreases, and vice versa. When the beam width is close to the size of the receiving slit, optimum intensity and resolution are obtained.

In order to prevent too much axial divergence of the beam, parallel-plate collimator (Soller collimator) is placed in the radiation path, usually before and after the specimen. These collimator typically subtend an angle of 2.5° and will remove much of the axial divergence.

The diffracted-beam monochromator consists of a single crystal. When a suitable slit or aperture is used, the monochromator has a sufficiently narrow band pass to allow rejection of K_β radiation from the anode. A monochromator can be placed between the source and the specimen (incident beam), or between the specimen and the detector (diffracted beam).

The function of the divergence slit (DS) is to limit the lateral divergence of the X-ray beam so that as much as the sample surface is irradiated as possible, but at the same time avoiding irradiation of the sample support.

The function of the detector is to convert the individual X-ray photons into voltage pulses that are counted by the counting equipment, allowing various forms of visual indication of X-ray intensity to be obtained. The scintillation counter is by far the most commonly employed.

The X-ray powder diffraction (XRD) profile of TiO_2 aerogels were obtained from a Rigaku' diffractometer with a horizontal goniometer D/MAX-B. A Cu sealed tube and a scintillation counter were used as the X-ray radiation source and detector. The power settings of the source were 40 mA and 40 kV. The TiO_2 aerogel was ground and painted on a glass slide with alcohol.

§ 5. 3 Results and Discussion

Figure 5-7 shows the X-ray powder diffraction profile over a 2θ-range 20 to 70°. A well-developed anatase crystallite is evident with the peak positions (indicated by solid line) matching consistently to the theoretical pattern of anatase [5]. The mean crystallite size of 5.2 - 5.8 nm at the {101} peak for anatase was determined from the Scherrer equation (5-6): $T = K\lambda / B \cos(\theta)$, where K is a shape factor of the particle (it is unity for spherical shapes), λ and θ are the wavelength (0.154 nm) and the incident angle of the X-rays, respectively. The peak width B was measured at half of the maximum intensity.

Table 5-1 shows peak finding data which include 2θ, d-spacing, intensity and full width half maximum (FWHM).

X-ray powder diffraction is a powerful tool to characterize that there is an average crystallite size about 5 nm in our TiO_2 aerogels. This fact can also be related to the total surface area which was obtained in Ch.4 if the particle shape is assumed. The diffraction

theory is referenced not only for this chapter but also for next chapter which discusses small-angle scattering techniques.

Table 5-1 Peak finding data.

D/MAX-B PEAK FINDING PROGRAM V 1.8

DATA FILE: C\DATA\Z02134.RAW
COLLECTED ON 18-JAN-93 AT 22:34:55
SAMPLE IDENTIFICATION: TIO2 AEROGEL

DATA OF PEAK SEARCH: 1-19-93 AT 04:03:43

START 2THETA: 20.000 STOP 2THETA: 70.000
STEP SIZE: 0.010 SCAN SPEED: 1.000
KV: 40, MA: 40

PEAK FINDING PARAMETERS

THRESHOLD VALUES:	5.0, 10.0
RELATIVE CUTOFF INTENSITY:	0.0
TYPICAL FULL WIDTH-HALF MAXIMUM:	1.00
MINIMUM FULL WIDTH-HALF MAXIMUM:	0.01
PEAK SPAN:	15
ALPHA 2 REMOVAL USING CODE:	1

BACKGROUND-SUBTRACTED DATA WILL BE IN FILE D:\DATA\Z02134
PEAK DATA WILL BE IN THE NEW FILE D:\DATA\Z02134.PKS
THRESHOLD DATA WILL BE IN FILE D:\DATA\Z02134.THD

PEAK	2-THETA	D-SPACE	I (REL)	I(CPS)	FWHM
1	25.230	3.5270	100.00	657.8	0.700
2	37.850	2.3750	50.93	335.0	1.219
3	47.790	1.9017	44.46	292.4	0.769
4	54.210	1.6907	41.81	275.0	2.620
5	62.410	1.4868	29.04	191.0	1.244

5 PEAKS WERE FOUND AND WRITTEN TO THE PEAKS FILE

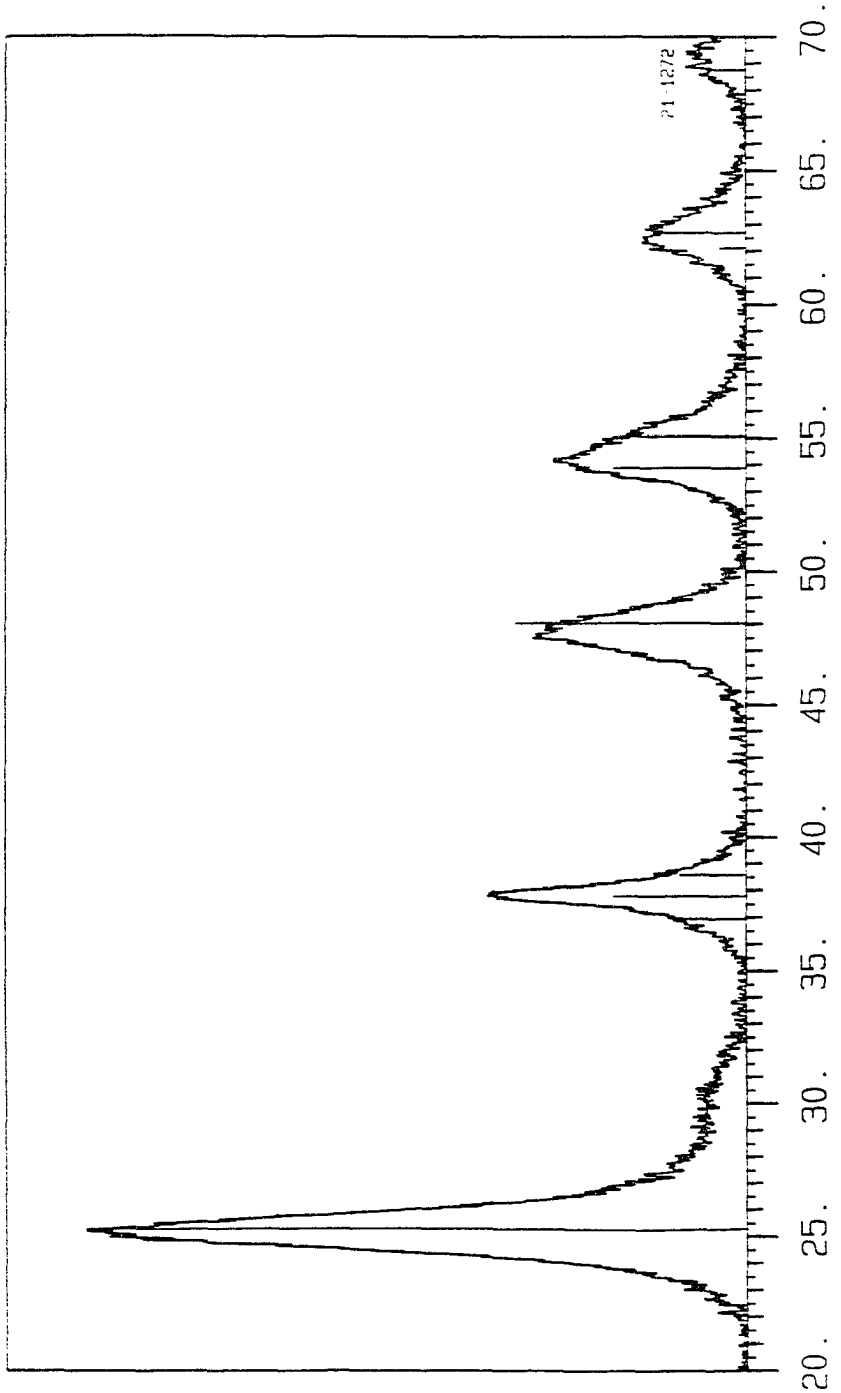

Figure 5-7 X-ray powder diffraction profile - Intensity (a.u.) vs. 2θ (degree).

CHAPTER 6. Small Angle Neutron Scattering

One of the most promising and nondestructive techniques for exploring the structure of materials is the Small Angle Neutron Scattering (SANS). The small angle scattering of an incident beam provides information at the superatomic level, i.e. with a spatial resolution from 1 nm up to 100 nm. The method of elastic scattering is used in various fields of science and technology including: condensed matter physics, molecular biology and biophysics, polymer science, and metallurgy. The SANS technique for studying porous materials is well established, but only in recent years its full potential has been realized [1-19]. Unlike electromagnetic radiation, electrons or other charged particles, which interact with the target primarily through long-range Coulomb fields, neutrons interact with the target via nuclear forces. Although these forces are strong, they are sufficiently short-ranged to allow neutrons to penetrate deeply into most materials, whereas electrons or X-rays of comparable wavelength are confined to the surface, or to samples of very small sizes. As a consequence, neutrons can easily probe bulk properties of materials. In addition, the advantages of SANS measurements include the sensitivity in a broad range of length scales and the low mass absorption coefficient.

§ 6. 1 Introduction

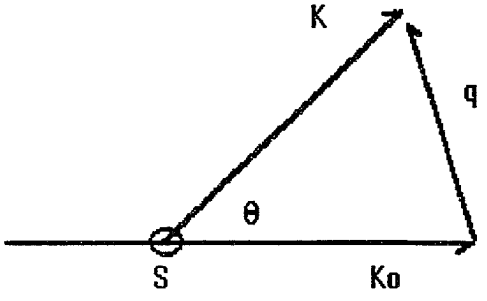

Figure 6-1 Basic geometry of scattering process.

Any scattering process is characterized by a reciprocity law, which gives an inverse relationship between the scattering vector q and the corresponding scale length $R_0 = 2\pi/q$. Figure 6-1 shows a basic geometry of scattering process (limit only elastic scattering), where **Ko** is the incident (or primary) wave vector; **K** is the scattered (or secondary) wave vector. The phase is $\phi = -\mathbf{q}\cdot\mathbf{r}$ if we define the scattering vector **q** as

$$\mathbf{q} = (\mathbf{K} - \mathbf{K}_o) \qquad (6\text{-}1)$$

or $q = (4\pi/\lambda)\sin(\theta/2)$, with θ the scattering angle and λ the neutron wave length. **S** can stand for solid, sample or scatterer.

The angle-dependent scattering amplitude is related to the neutron scattering length density distribution of the scatterer by a Fourier transformation.

The inverse Fourier transform can be performed to give the structure factors $F(\mathbf{q})$ from the Eq. (5-8) by replacing scattering density for a non-periodic structure

$$F(\mathbf{q}) = \int \rho(\mathbf{r}) \exp(i\mathbf{q}\cdot\mathbf{r})\, dV \qquad (6\text{-}2)$$

From Eq. (6-2), the best way of deriving the intensity $I(\mathbf{q})$ as the absolute square is by using the conjugate complex F^*

$$I(\mathbf{q}) = F F^* = \int\int \rho(\mathbf{r}_1)\rho(\mathbf{r}_2) \exp[-i\mathbf{q}\cdot(\mathbf{r}_1 - \mathbf{r}_2)]\, dV_1\, dV_2 \qquad (6\text{-}3)$$

The main problem in the structure analysis of matter is the reconstruction of the scattering density distribution according to the measured function I(q). The theory of Fourier transforms provides the basic mathematical apparatus for structural determinations.

§ 6. 2 Data Analysis [20-24]

A set of approximations and models will be used to derive microstructural parameters of interest from SANS data. The Guinier approximation is often used for well defined

discrete inhomogeneities [21], Porod's law mainly applies for interface surface area determination [21], and the Debye, Anderson and Brumberger (DAB) model is used for randomly disordered microstructure on a single length scale [9,25]. All three models were used to characterize the morphology of TiO_2 aerogels. The particle size distribution will be obtained by applying either the log-normal distribution [26-28] or the maximum entropy method (MEM) [11,12,29-32].

Guinier's approximation [21]

For dilute isolated particles, Guinier's approximation is applicable for small q, and it provides a simple characterization of the mean particle radius R_{Gr}. (The mean particle radius of gyration R_G is the root mean square of the distance from the particle center of gravity to its surface. For spherical particles $R_G^2 = (3/5)R_{Gr}^2$.) The scattering intensity at small angles ($qR_G < 2.5$) is given by

$$I(q) = I(0)\exp(-q^2R_{Gr}^2/5) \qquad (6\text{-}4)$$

where I(q) is the SANS intensity at small angles as a function of the modules of the scattering vector q. I(0) is the extrapolated scattering intensity at q = 0. The linear behavior of Guinier plot of Ln I(q) vs. q^2 indicates the presence of a population of particles with mean radius R_{Gr}.

Rigorously, Guinier's law is only valid for infinitely dilute systems where particle-particle correlations are absent, so that the measured I(q) is purely due to the individual particle's size and shape. However, in a few cases where the particle density is not low, the Guinier approximation can still be valid as long as the particle-particle correlations are nearly constant over the interested range [33]. Over that range, where qR_G is small, the only

particle-particle correlation is the nearest neighbor interaction for a connected network. However, if polydispersity is present, that correlation can be smeared out by the broad size distribution.

Porod approximation [21]

The scattered intensity of a smooth surface scatterer for sufficiently large q follows the standard Porod law. For a rough surface, the modified Porod law can be written as

$$I(q) = Pq^{-x} + B \qquad 3 \le x \le 4, \tag{6-5}$$

where P is the Porod constant and B is a background term. Both P and B are obtained from linear least-squares fit to Iq^x vs q^x plots (modified Porod plot). x can be interpreted in terms of the roughness of the surface. It was correlated with a surface fractal when x is between 3 and 4, such that the fractal dimension is given by $D_s = 6-x$ [34]. Therefore, $D_s = 2$ or $x = 4$ indicates a perfectly smooth surface. The total surface area down to certain probe size r per unit volume (S/V) can be determined by [34]

$$S/V = [2\pi\phi(1-\phi)P/F(x)Q]r^{x-4}, \tag{6-6}$$

where Q, the Porod invariant, is an important characteristic integral of the scattering intensity

$$Q = \int_0^\infty q^2 I(q)\, dq \tag{6-7}$$

and $F(x) = \Gamma(x-1)\sin[(x-3)\pi/2]/(x-3)$. We took r as the size of a nitrogen molecule ($r^2 = 0.162$ nm^2), in order to compare it with the results of nitrogen adsorption. An average particle radius R_p can be calculated from S/V by assuming particle distribution and geometry ($S/V=3/R_p$ for a homogeneous spherical particle distribution).

DAB model [25]

In order to determine structure-related geometrical parameters, one starts with the hypothesis that the aerogels can be approximated by a two-phase model. In this model the aerogel contains a solid matrix phase having a density of d_s (skeletal density) and an empty (air-filled) pore phase. The solid phase occupies a volume fraction $1-\phi$, and the porous phase occupies a volume fraction ϕ (porosity). Scattering takes place at the interface of these two phases.

An alternative isotropic two-phase system approach is the Debye-Anderson-Blumberger (DAB) approximation. From Eq. (6-6) the small-angle scattering intensity can be written as

$$I(q) = 4\pi\phi(1-\phi)V(\Delta\rho)^2 \int_0^\infty r^2\gamma(r)\frac{Sinqr}{qr}dr \qquad (6\text{-}8)$$

where V is the irradiated sample volume, ϕ and $(1-\phi)$ are the volume fractions of the phases; $\Delta\rho$ is the difference in scattering length density between the two mediums; $\gamma(r)$ is the correlation function defined as the average the product of the two local scattering length density fluctuations separated by a distance r.

$\gamma(r)$ can be expressed as an exponential correlation function, if the two-phase system exhibits a random distribution of particles (size, shape and position) by DAB

$$\gamma(r) = \exp(-r/a) \qquad (6\text{-}9)$$

where a is the correlation distance of the particles.

Substituting Eq. (6-9) into Eq. (6-8) results in

$$I(q) = \frac{A}{(1+a^2q^2)^2} \qquad (6\text{-}10)$$

In order to get better fitting, the DAB expression can also be modified to account for roughness

$$I(q) = \frac{A}{(1+a^2q^2)^{x/2}} \qquad (6\text{-}11a)$$

The characteristic length a is obtained from linear least-squares fit to $I^{-2/x}$ vs $\hat{q}$ plots (modified DAB plot).

For small q, Eq. (6-11a) can be approximated by a Guinier form

$$I(q) = A \exp(-q^2R_a^2/5) \qquad (6\text{-}11b)$$

where $R_a = \sqrt{(5x/2)}a$; it can be defined as an average radius of the spherical particles. For large q, Eq. (6-11a) takes Porod form

$$I(q) = (A/a^x)q^{-x} \qquad (6\text{-}11c)$$

When x = 4, the interface area per unit volume from the probability calculation of DAB model is

$$(S/V)_{DAB} = 4\phi(1-\phi)/a \qquad (6\text{-}12)$$

Consistently, if the Porod form $I(q) = (A/a^4)q^{-4}$ is taken, starting from the definition of Porod: $S/V = \pi\phi(1-\phi)P/Q$; the same result like Eq. (6-12) will be obtained. In another words, the quantity of interface area per unit volume, which is more sensitive to the large q from two different models, ended at same point.

The log-normal particle size distribution

The particle size distribution (PSD) from SANS data is often approximated by the

log-normal distribution. The log-normal distribution of small angle X-ray scattering analysis for particle size distribution was given by Harkness et. al.[26]. The result was theoretically derived by Baur and Gerold [27] in which only spherical particles having a log- normal size distribution were assumed. These authors pointed out that a deficiency of their procedure was that it could not be applied accurately if the Porod constant could not be experimentally determined over a reasonable q interval. For spherical particles, a particle size distribution function F(R) [28] is defined such that F(R)dR denotes the fraction of the particles having radii between R and R+dR. F(R) is thus normalized i.e., $\int F(R)dR = 1$.

The form of the log-normal distribution is given by

$$F(R) = \frac{1}{\sqrt{2\pi}R\ln\sigma}\exp\left[-\frac{1}{2}\left(\frac{\ln R-\ln\mu}{\ln\sigma}\right)^2\right] \qquad (6\text{-}13)$$

where μ is the geometric mean of the radius and σ is the geometric standard deviation of variance. These parameters can be derived in the following way.

The nth moment of R, $\langle R^n \rangle$, is given by

$$\langle R^n \rangle = \int_0^\infty R^n F(R)\, dR \qquad (6\text{-}14)$$

The ratio of nth moment to the kth moment of R is obtained by substituting Eq. (6-13) to (6-14)

$$\langle R^n \rangle / \langle R^k \rangle = \exp 0.5[2(n-k)\ln\mu+(n^2-k^2)\ln^2\sigma] \qquad (6\text{-}15)$$

Taking $R_{Gr}^2 = 5/3 \langle R^7 \rangle / \langle R^5 \rangle$, $R_p = 3V/S = 3 \langle R^3 \rangle / \langle R^2 \rangle$ [28], thus these parameters can be expressed in terms of R_{Gr} and R_p in the following way

$$\ln\mu = \ln R_{Gr} - 1.56 \ln(R_{Gr}/R_p) \qquad (6\text{-}16)$$

$$\ln^2\sigma = 0.22 \ln(R_{Gr}/R_p) \qquad (6\text{-}17)$$

The maximum entropy method

The other procedure to extract particle size distribution is the maximum entropy method (MEM) [29]. The main attraction of this procedure is that it shows considerable promise for estimating spectra when the length of the available data record is short and without phase information. The MEM has the important property of providing a unique solution to a practical inverse problem consistent with the experimental errors [30-32]. No assumptions are made about missing data. The derived particle size distribution has the maximum configurational entropy consistent with the available data, and has the least structure. The method, when used for SANS data analysis [10,11], requires that the scatterers all have the same shape, and the shape be known (e.g. spherical), and that the scatterers scatter independently.

All the above models use the particle's form factor in fitting the data, that is to assume that the particles scatter independently so that the correlation in their position, or the structure factor, can be ignored. This is usually only true at large q where the Porod's law is applied. For small and intermediate q ranges, it is conventional to assume that one has to consider at least the nearest neighbor interaction for a granular medium globally interconnected. However, in the DAB model [25], it was concluded that as long as the porous medium is random, the scattering function can be described by a Lorenzian squared form with a characteristic length only, despite the value of the porosity or the volume fraction. Although the degree of randomness needed to justify the neglect of the nearest

neighbor interaction is uncertain, the electron microscopy studies (See Ch.7) provide strong evidence for a considerable degree of randomness in the packing. The only experimental result that provides information about the packing of the nanoparticles in the mesoaggregates is the skeletal density. We have assumed that the measured skeletal density of 2.8 g/cm^3 corresponds to the density of the mesoaggregates which implies porosity of 0.26 for the mesoaggregates. This agrees with hexagonal close packing [35]. Random close packing of identical spheres requires porosity of 0.36 [35, 36], but if the spheres are not exactly identical the theoretical values can be varied.

§ 6. 3 Experimental Description

SANS spectrometer

Small angle neutron scattering experiments were performed at the National Institute of Science and Technology (NIST) using a 30 meter NG7 SANS spectrometer [37]. The spectrometer uses neutrons from a cold source of 20-MW NIST research reactor which has a beam flux of $2x10^{14}$ neutrons $cm^{-2} s^{-1}$. The spectrometer constitutes by 15 meters pre-sample flight path and 15 meters post-sample flight path. The layout of the NG7-SANS spectrometer is shown in Figure 6-2.

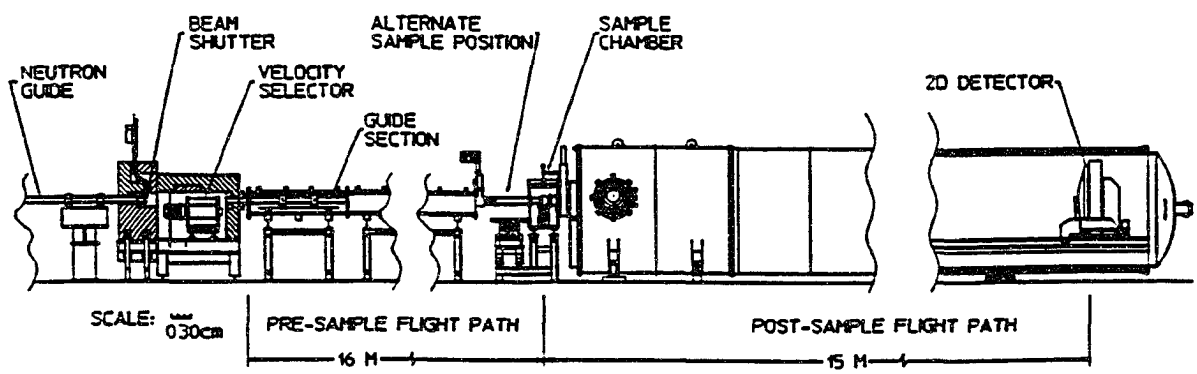

Figure 6-2 The layout of the NG7-SANS spectrometer in side view.

The major components of the spectrometer, data acquisition system and its performance are described as following: (a summary table of NG7-SANS' characteristics and performance is listed in appendix).

1) Beam filtering and wavelength selection:

Neutrons from the cold source are monochromated by a monochromator in conjunction with a liquid-nitrogen-cooled filter of single-crystal bismuth and polycrystalline beryllium to remove core γ-rays and fast neutrons from the beam. Then the beam is mechanically chopped by a helical channel (multidisk) velocity selector with variable speed and pitch which enables both the mean wavelength (0.5 to 2.0 nm) and wavelength spread (0.10 to 0.30 FWHM) to be varied. Flexibility in collimation is effected within this path by means of eight 1.5 m long neutron guide sections that can be easily shifted in or out of the beam. The beam divergence and flux on the sample are thus varied by changing the effective source-to-sample distance from 3 to 15 m in 1.5 m increments. Finally, a continuous incident beam whose wavelength is variable from 5 to 10 Å is provided.

2) Sample stage:

The instrument has two choices of sample location: one is a permanently installed sample chamber (that can be used in air or under vacuum) with a computer-controlled sample stage, and the other is a 60 cm diameter sample table, between the pre-sample flight path and the sample chamber, which can accommodate several types of cryostat, furnaces, electromagnets and a large superconducting magnet, a shear cell, etc.. A flux of 2×10^5 neutrons $cm^{-2}s^{-1}$ over a 1.27 cm diameter area will be at the sample position.

3) Two dimensional position-sensitive detector:

The 15 m long post-sample flight path consists of a long cylindrical section that forms a vacuum enclosure for a large two dimensional position-sensitive neutron detector. The area detector (65×65 cm^2 with 1 cm^2 spatial resolution) moves along rails that are parallel to the neutron beam inside the cylindrical vessel to vary the sample-to-detector distance continuously from 3.6 m to 15 m for NG7-SANS. In addition, the detector moves transversely to the beam direction (by up to 30 cm) to extend the q range covered at a given detector distance.

4) Position decoding and data acquisition electronics:

The rise-time encoded coordinates of each detected neutron are decoded through two independent time difference measurements effected by the electronics. A dedicated computer for data acquisition and instrument control is operated through a menu-driven interface. A color monitor displays a continuously updated image of the data being collected. Completed data sets can be produced on-line.

Experimental conditions

Generally, the finite size of the beam, its divergence, the size of the detector and the wavelength distribution will lead to an instrumental broadening as in most physical investigations. The measured scattering curve is said to be smeared by these effects. The high resolution NG7-SANS spectrometer is designed to limit all these effects to the minimum. The instrument is made to cover a wide q range, from 0.01 to nearly 6 nm^{-1}; it is suitable for examining structural features in materials ranging from roughly 1 to 600 nm.

In the experiments reported here, the wavelength of the incident neutrons was 0.7 nm, with a spread of 14%. A q range of 0.024 - 1.6 nm^{-1} was accomplished with two

configurations: one low-q configuration had a source-sample distance of 16.30 m and sample-detector distance of 15.35 m, and the other high-q configuration had a source-sample distance of 7.01 m and sample-detector distance of 3.70 m. A chunk of the samples were filled in a cell with 2 quartz windows 1 mm apart. At such path length, the transmission of the samples is typically above 0.85. Therefore, multiple scattering effects are negligible. A two-dimensional position-sensitive neutron detector was used to record the scattering pattern.

Before the two dimensional raw data was circularly averaged to produce the one-dimensional I(q) data in an arbitrary scale, it was corrected for the background (blocked beam) and empty cell scattering. A transmission correction is made for measured intensity as following

$$I_{cor} = I_{sam} - I_{bgd} - T_{sam}/T_{emp}(I_{emp} - I_{bgd}) \qquad (6\text{-}18)$$

where $T_{sam} = I_{sam}(0)/I_{bgd}(0)$, $T_{emp} = I_{emp}(0)/I_{bgd}(0)$.

§ 6. 4 Results and Discussion [38]

Figure 6-3 shows an example of the SANS profile for sample D. This profile and those from the other samples do not exhibit a peak as expected from the nearest neighbor correlation. However, if the correlation is present but very weak, it could show up as a little "shoulder", or a change in the slope of the scattering intensity profile at a q value corresponding to the average center-center distance of the nearest neighbors. This "shoulder" is apparent in Fig. 6-3, at $q = q_0 = 0.45$ nm^{-1}, corresponding to a distance of $d = 2\pi/q_0 = 14$ nm. For aerogels, d should also correspond to the average diameter of the particles, since the nearest neighbor is in contact, and is in good agreement with other models (See Table 6-2 below).

Figures 6-4, 6-5 and 6-6 show the Guinier, modified Porod and modified DAB plot of sample D along with the theoretical fits to Eqs. (6-7), (6-8) and (6-14a). Table 6-1 shows the surface to volume ratio (S/V) that is derived from the modified Porod, and compared with BET results and also lists the specific surface areas (S/M). Table 6-2 summarizes the Guinier, modified Porod and modified DAB parameters for the four samples.

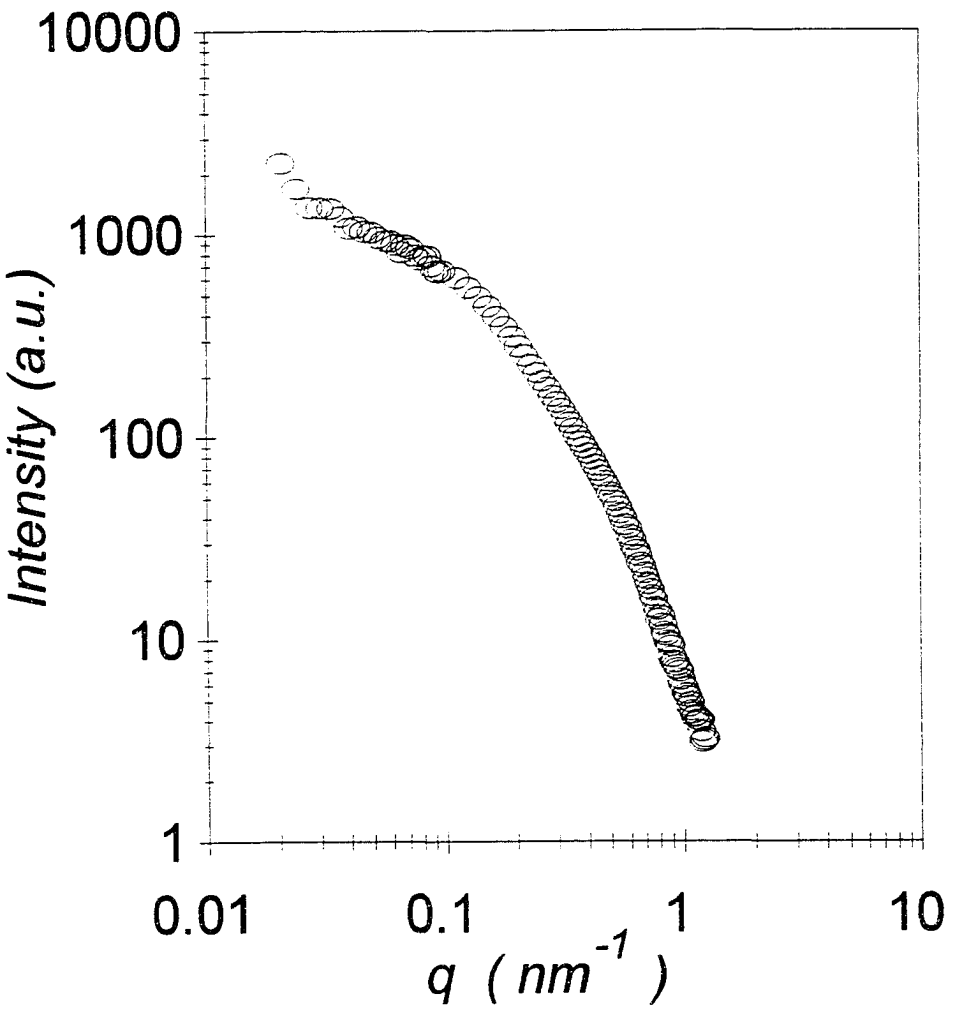

Figure 6-3 An example of the SANS profile for sample D.

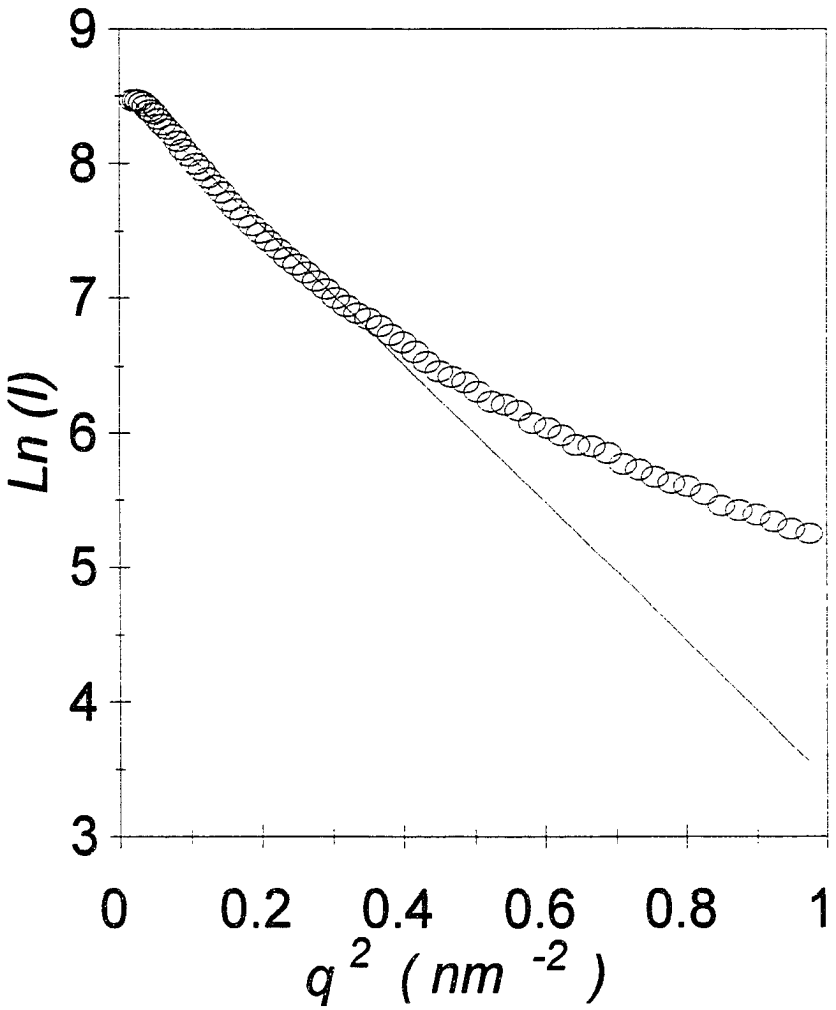

Figure 6-4 The Guinier plot of sample D along with the theoretical fit to Eq. (6-4).

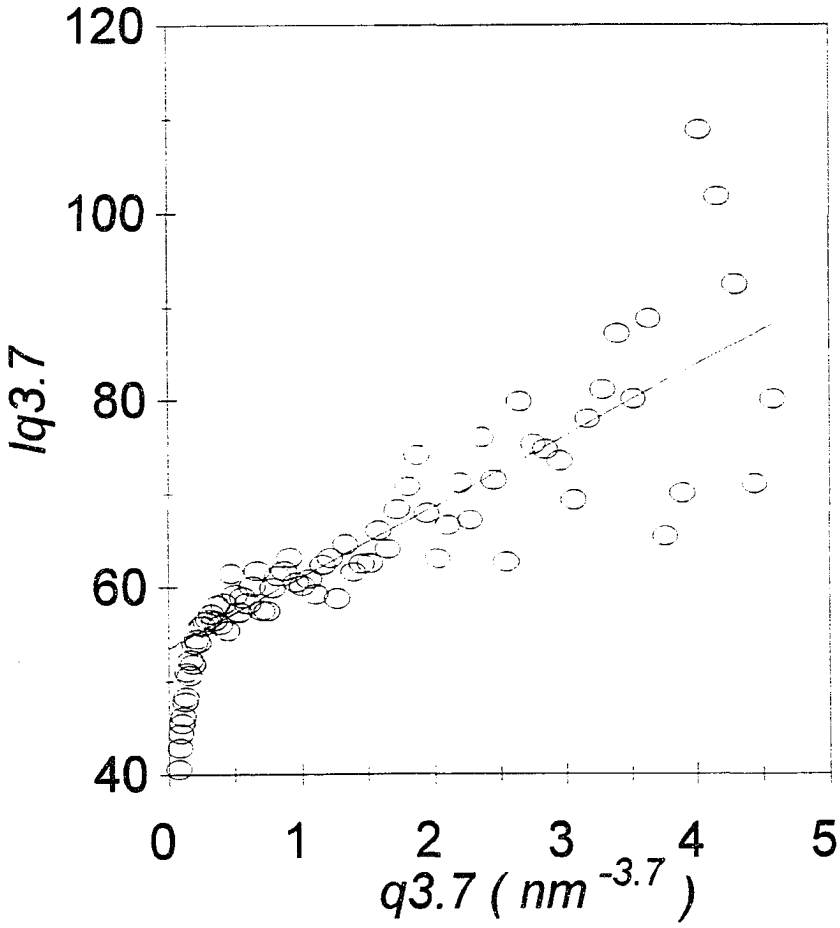

Figure 6-5 The modified Porod plot of sample D along with the theoretical fit to Eq. (6-5).

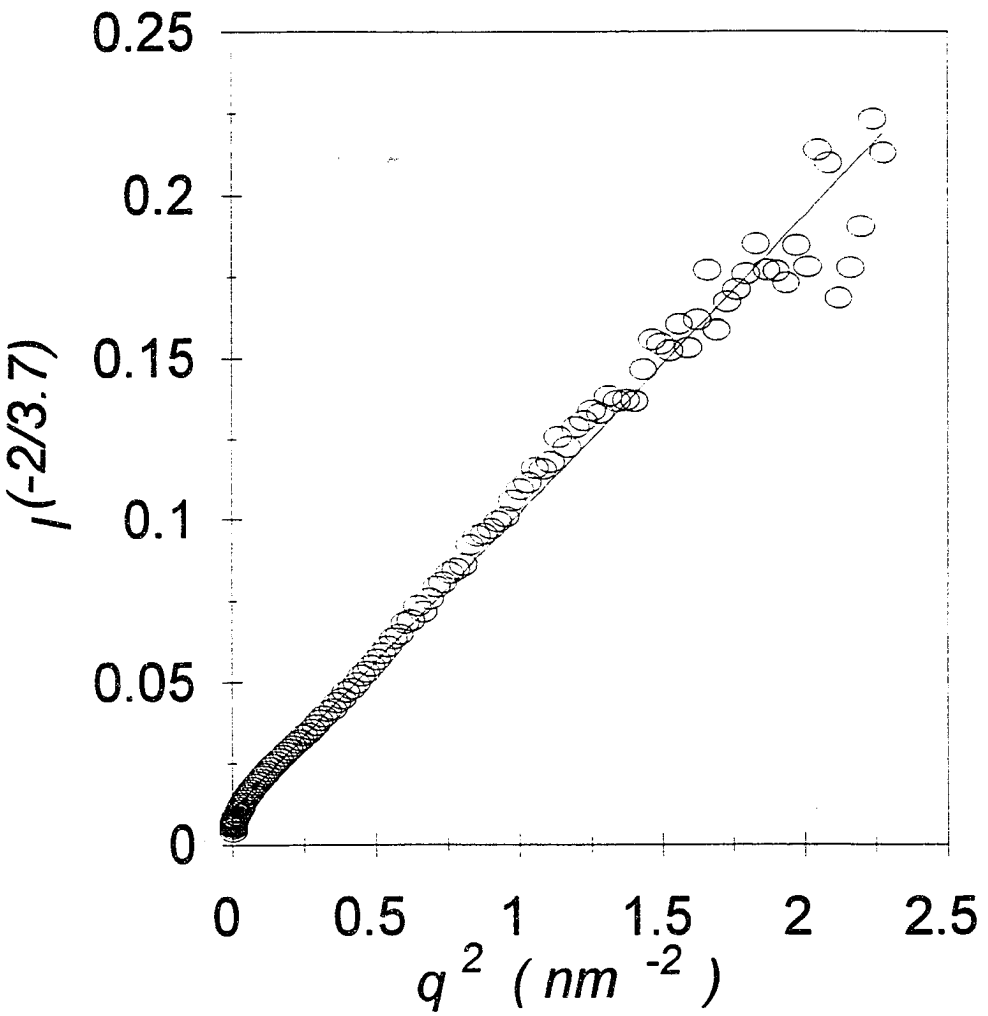

Figure 6-6 The modified DAB plot of sample D along with the theoretical fit to Eq. (6-11a).

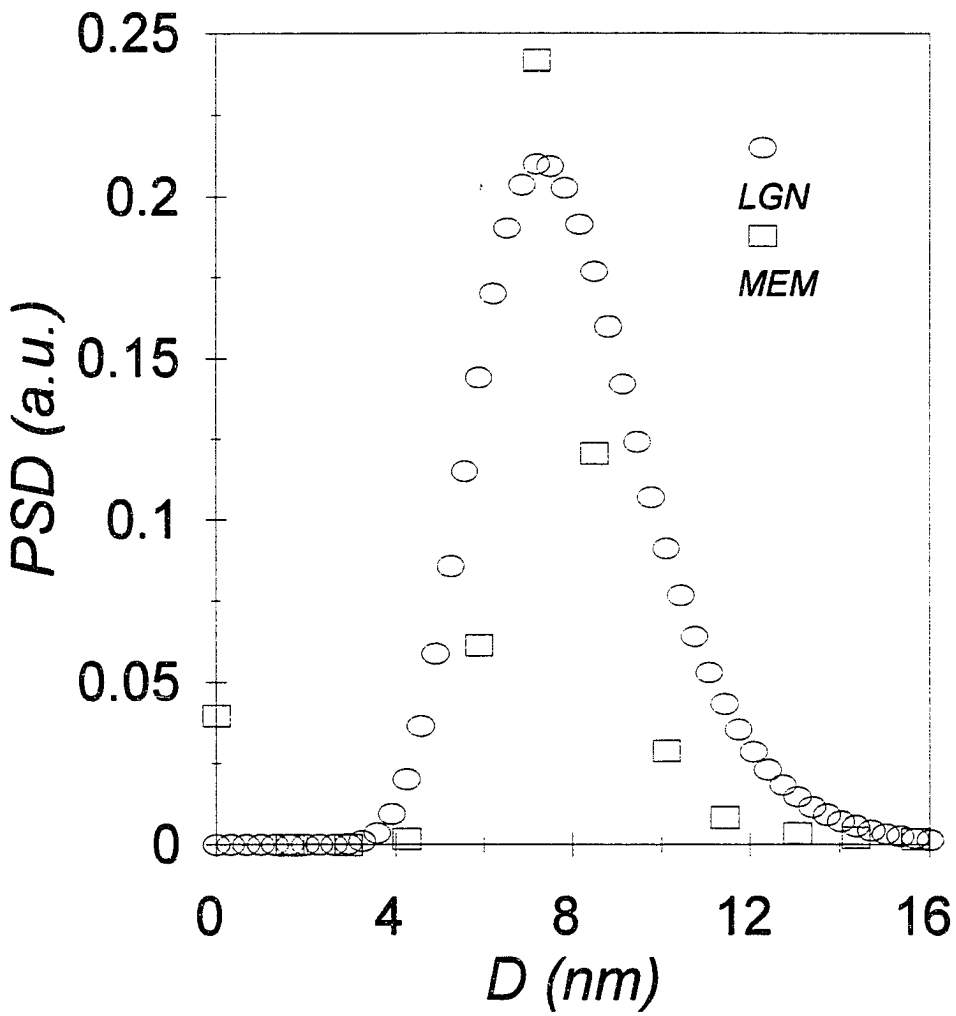

Figure 6-7 The particle size distributions (PSD) calculated for sample C using the log-normal size distribution (LGN) and the maximum entropy method (MEM).

Table 6-1 The modified Porod law exponent -x, surface to volume ratio S/V(nm^{-1}), specific surface area S/M(m^2/g) obtained from the modified Porod (p), and BET (b) methods.

Sample	x	$(S/V)_p$	$(S/V)_b$	$(S/M)_p$	$(S/M)_b$
A	3.22	0.223	0.223	201	201
B	3.47	0.229	0.256	416	465
C	3.25	0.257	0.222	494	426
D	3.70	0.217	0.259	374	447

Table 6-2 SANS parameters that were obtained from the Guinier plots (R_G, R_{Gr}-nm), the modified Porod plots (R_p -nm) and modified DAB plots (a, R_a-nm).

Sample	R_G	R_{Gr}	R_p	a	R_a
A	8.44	10.9	13.5	3.82	10.8
B	3.93	5.07	13.1	2.33	6.86
C	4.61	5.95	11.7	2.76	7.87
D	9.81	12.7	13.8	2.49	7.57

Table 6-1 compares the surface/volume ratio and the specific surface area obtained by using modified Porod method (Eq. (6-5)) with the BET (nitrogen adsorption) data. It shows an excellent agreement for all four samples. The maximum discrepancy is 16% for sample D. Since the length scale probed by the nitrogen adsorption data is of the order of the size of a nitrogen molecule (0.4 nm), and the one probed by the SANS experiment is $2\pi/q_{max}$ ~ 4 nm, it strongly suggests the validity of the extrapolation by an order of magnitude

that was done by modifying the Porod expression through the introduction of fractal assumption (q^{-x}).

In addition, the agreement of the SANS analysis with the BET method is strong evidence in support of a completely open pore structure, since the SANS data are insensitive to the openness of the pore structure and the BET data are generated only from pores that are accessible to the adsorbing gas.

Table 6-2 lists the equivalent size of the particles obtained using the different methods (a spherical shape is assumed). Comparing R_a with R_{Gr} tells us how good the DAB form fits the SANS data at low q, and, for most samples the fit is very good. Although it is an over-simplification to treat all particles as spherical, it nevertheless agrees remarkably well with microscopic measurements of the nanoparticles (See Ch.7). The Porod radius R_p was obtained assuming the surface area probed by the scattering beam is the total surfaces of the spherical particles. It neglects the fact that part of these surfaces were not exposed to the scattering because the particles are all fused together. As a result, R_p is larger than R_a by 20% to 50%. If other effects are negligible, this can be thought of as the percentage of those "non-exposed" surface areas. We note that SANS data here are only sensitive to the scale of the nanoparticles (5-10 nm). However, one can see that the scattering intensity starts to rise again at the lowest q (Fig. 6-3), which we believe is due to the larger length scale correlation responsible for the mesoaggregates (about 50 nm).

From the Porod radius R_p and the radius obtained from the Guinier fit, R_{Gr}, we can construct a particle size distribution in terms of the log-normal (LGN) distribution (Eqs. (6-16, 6-17)). In addition, we use the maximum entropy method which was developed as

MAXENT program by NIST group [10,11] with a spherical form to obtain the particle size distribution. Figure 6-7 shows the results from the two different methods for sample C. One feature, which is consistent for all samples, is that LGN distribution always peaks at a higher size than the MEM distribution. This is because the MEM uses a spherical shape, and cannot tolerate roughness. Any irregularly shaped particle would be preferably counted as several smaller "spherical" particles. If a modified "rough" spherical form factor was used with the maximum entropy method, we would expect to see the peak shift towards larger sizes. On the other hand, the log-normal formula is highly weighted by the Guinier approximation (Eq. (6-4)), which is insensitive to the detailed shape of particles. In that sense, the log-normal distribution is more reliable.

We have demonstrated excellent agreement between the various available models for interpreting SANS scattering data in terms of structural information when one expects a much higher degree of model-sensitivity in such analysis. This kind of agreement demonstrated that our SANS experiment is powerful in probing the nanoparticle structure. It also serves to strengthen the conclusion that the relevant length-scales in these aerogels are intrinsic and model independent, even the models that were applied to different q ranges.

CHAPTER 7. Electron Microscopies

§ 7. 1 Introduction

Although the first electron microscope was built in 1932[1], Electron Microscopy (EM) has been a major research tool in many areas of science [2]. The application of EM on aerogel study has been practiced [3-5] even with the difficulty of the sample preparation. Not only the information on size and shape can be obtained on very small samples but also the existence of pores or particles can be viewed directly. Generally, electron microscopies (EM) include the transmission electron microscopy (TEM) and scanning electron microscopy (SEM). For TEM, the instrumental resolutions can reveal important crystallographic details on the scale needed for structural studies. Sometimes, SEM have permitted a study of three-dimensional views of surface pores. Some of the fundamental concepts, methods and microscopic pore structure pictures are covered in this chapter.

TEM images are formed in two stages (See Fig. 7-1). The first consists of scattering of an incident electron beam by a specimen: this scattered radiation passes through an objective lens, which focuses it to form the primary image (A) that is subsequently magnified by additional lenses to form a highly magnified final image (B).

High spatial resolution is one of the major attractions of the TEM. Two widely used methods for specifying resolution are relevant for our purposes, and it is important to distinguish between them. Point-to-point resolution is the most useful. It is a measure of the ability of the TEM to faithfully reproduce the structure of the sample as projected in the direction of the incident electron beam. Another measure, line (or fringe) resolution, considers the smallest distinguishable separations between regularly spaced fringes.

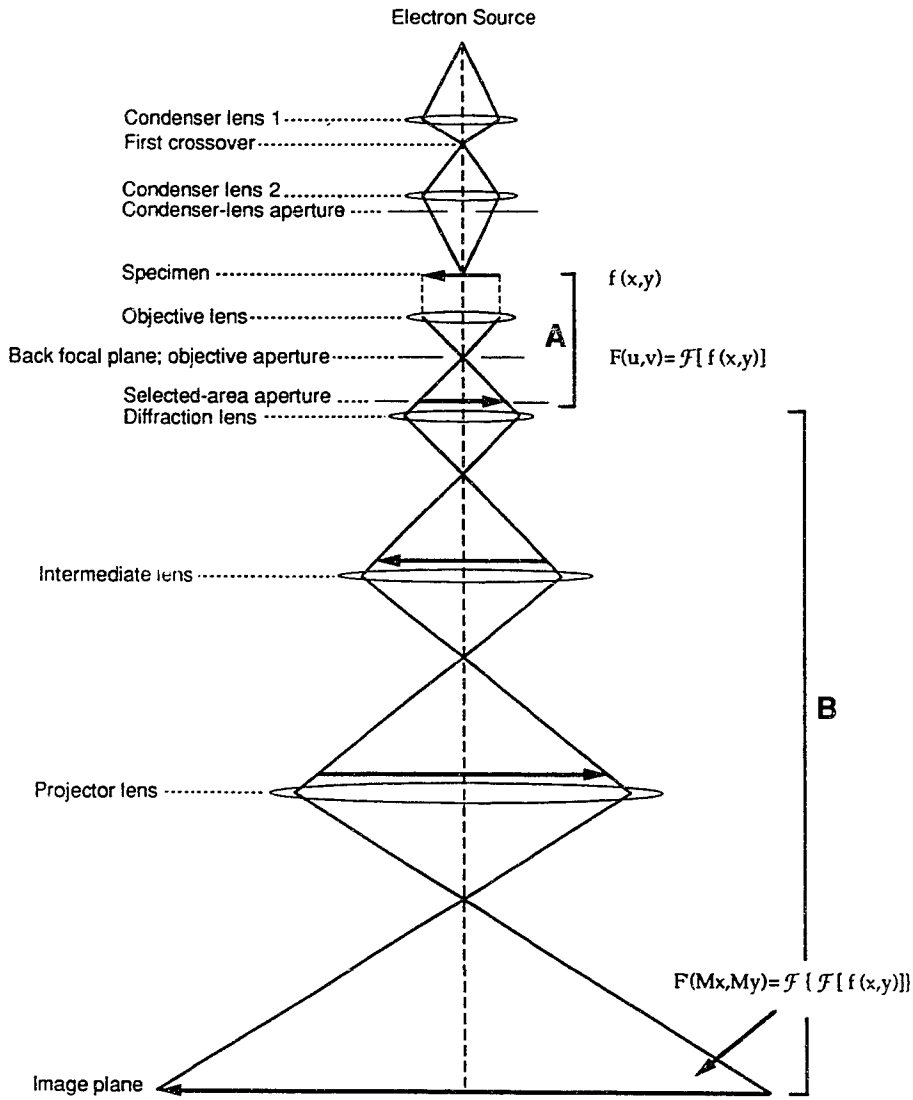

Figure 7-1 Ray diagram of a TEM. The horizontal arrows show the positions of the specimen and its images as they are progressively enlarged at various levels of the microscope. "A" indicates stage 1, and "B" indicates stage 2.

The general express for resolution, r, for bright-field point-to-point imaging is

$$R = 0.67\ \lambda^{3/4} C_s^{\ 1/4} \qquad (7\text{-}1)$$

where λ is the electron wavelength, and C_s is the coefficient of spherical aberration of the objective lens. It is evident that improvements in resolution can be made by decreasing the wavelength and spherical aberration. An increase in accelerating potential decreases the wavelength but causes other problems such as power-supply and instrumental instabilities as well as greatly increased costs. Achieving decreases in C_s requires the solution of extremely difficult pole-piece design and engineering problems.

Although the principles of diffraction are identical, there are prominent differences arising from the contrasting character of electron radiation versus X-radiation. The most prominent difference for our purposes is that electrons can be used to produce images whereas X-rays, except in very special cases, cannot. Also, electrons can be focussed into narrow, high-intensity beams that permit measurements confined to small specimen volumes, i.e., at high spatial resolutions. In addition, the ease of obtaining diffraction patterns by the two methods differ greatly.

X-rays interact with and are diffracted by orbital electrons, whereas electrons interact with and are diffracted by the electrostatic potential arising from both orbital electrons and the atomic nuclei. The result of this strong interaction is that electron scattering is far more efficient than X-rays (by a factor of 10^2 or 10^3), and so diffraction patterns are obtained much more rapidly with electron beams. In the TEM, diffraction patterns are produced almost instantaneously.

The wave nature of electrons is significant. The wave length is given by $\lambda = h/p$,

where h is Planck's constant, and p is the momentum, p = mv, where m is the mass, and v is the velocity. If relativistic effects are neglected, the convenient formula is $\lambda = (150/V)^{1/2}$, where λ is the wavelength in angstrogn, and V is the voltage in volts used to accelerate the electrons. For the higher energies, relativistic effects become important. The wavelength is given by

$$\lambda = h/[2m_0 eV(1+eV/2m_0c^2)]^{1/2} \qquad (7\text{-}2)$$

where m_0 is the rest mass, and c is the velocity of light. The relativistic correction is amount to 4.4% at $V=10^5$ V ($\lambda = 0.0370$Å) and 29% at V=1MV ($\lambda = 0.00872$Å).

Electrons have far shorter wavelengths than X-rays, and that difference greatly affects the diffraction conditions. For example, 200 KeV electrons, which are commonly used in high-resolution electron microscopy, have $\lambda = 1.54\times10^{-3}$ nm. For comparison, Cu K_α radiation has $\lambda = 1.54\times10^{-1}$ nm, almost two orders of magnitude greater. It follows from the Bragg equation ($n\lambda = 2d\sin\theta$) that a decrease in λ results in a corresponding decrease in diffraction angles, and so Bragg angles for diffraction are far smaller for electrons than for X-rays. For example, the scattering angles for 1-Mev electrons is roughly a quarter those of 100-KeV electrons. Such differences in scattering angles have major effects on the ways diffraction data are collected.

Another consequence of the strong interaction of electron beams with atoms is that, in distinction to X-ray diffraction, diffracted electrons have a greater probability of themselves being scattered as they pass through the sample. Such multiple scattering is characteristic of transmission electron microscopy and is important for all but the thinnest of specimens. The multiple scattering produces major effects and so must be considered when interpreting

electron-diffraction patterns and HRTEM images. Single-scattering diffraction is called kinematical and multiple-scattering diffraction is called dynamical. Kinematical theory is typically used for X-ray diffraction; it is also a useful first approximation for understanding events in the TEM, particularly when very thin crystals are being studied. Dynamical theory, while more complex, is required for understanding electron diffraction in all but the thinnest crystals [6].

Dynamical diffraction gives rise to diffracted intensities that are difficult to interpret quantitatively. Even the slightest differences in path lengths, such as are produced by local variations in crystal thickness or crystal tilt, can have significant effects on the intensities. Moreover, some energy can be lost through inelastic scattering independent of these diffraction events, further complicating the resultant intensities for calculation and interpretation of electron diffraction patterns and images. Here it suffices to note that X-ray intensities can be calculated more easily than electron intensities, which is a major reason why crystal-structure analyses are best done through X-ray measurements when a sufficiently large crystal is available. (In some cases structure analyses are done using convergent-beam electron diffraction because it is sensitive to a lack of inversion symmetry, whereas, to a first order, X-ray diffraction is not.)

Diffraction patterns can be produced using parallel electron beams. Such patterns are called selected-area electron-diffraction (SAED) patterns; the areas of specimen to be studied are chosen with a "selected area" aperture inserted in the image plane of the objective lens (Fig. 7-1) or, alternatively, in the image plane of the diffraction lens. Generally the area of specimen used for an SAED pattern, perhaps a half micrometer in diameter, is significantly

larger than the portion used for an HRTEM image. For many purposes, it is helpful to use a focused electron beam, generated by converging the beam by suitable adjustments to the condenser-lens aperture (Fig. 7-1). These patterns are called convergent-beam electron-diffraction (CBED) patterns.

Neglecting complexities in order to illustrate basic principles, the diffraction pattern from a thin specimen can be considered as the Fourier transform of the specimen (more accurately, as the Fourier transform of the projected potential distribution of the atoms in the specimen). The relations are illustrated schematically in Fig. 7-1. We shall assume the specimen is planar, with its features described as f(x,y). Here x,y are real-space position parameters, and f(x,y) represents the distribution of electron potential in the sample. Then F(u,v), suitably adjusted for the variables considered in the previous section, describes the diffraction pattern: F(u,v) = F[f(x,y)], where F represents a Fourier transform. The variables u,v are the reciprocal-space analogues of x,y. With the TEM, the electron wave in the image plane can then be described by applying another Fourier transform: F(x,y), so that F(Mx,My) = F{F[f(x,y)]} (the inverse Fourier transform is used for calculations; for the lens it is a proper Fourier transform). The magnification produced by the projector lenses is represented by the term M. The amplitudes of the Bragg reflections form the Fourier coefficients in a series whose sum gives the image amplitude.

While a comparable process is also conceptually feasible for X-rays, the second Fourier transform would need to be carried out on the diffracted-beam intensities. However, since the phases of the X-ray beams are lost, it is not normally possible to obtain the inverse Fourier transform, nor to obtain images using X-rays.

Computed images are critical for achieving proper interpretations of experimental results. Repeated iterations are typical, since commonly one or more of these variables are not known with high precision and must be estimated until good matches are obtained between experiments and calculation. By using a set of images obtained at a range of focus conditions (a through-focus series), it is generally possible to confirm that the approximations are reliable [7].

Measurements analogous to those made with the electron microprobe analyzer are routinely made with many TEMs. As in the microprobe, the incoming electron beam excites X-rays that are characteristic of the elements in the specimen, and these can be monitored by using a detector placed above or at the same level as the specimen. When the electrons in the incoming beam interact inelastically with the specimen atoms there is a transfer of energy, and the beam electrons lose energy. This decrease in energy can be monitored by a detector that is placed below the sample, so that it records electrons after they have traversed the sample.

The incoming beam can also excite secondary electrons, such as are used in the conventional scanning electron microscope (SEM) [8].

§ 7. 2 Instrumentation

1) Sample stages:

The position of the specimen within the TEM greatly affects performance. The specimen is placed between the upper and lower halves (pole pieces) of the objective lens, so that it is effectively immersed within the lens. For maximum resolutions the pole-piece gap should be as narrow as possible; values of only a few millimeters are used in modern high-resolution TEMs. Since TEM grids are thin, as are the samples used for microscopy, this

space restriction might seem minor. However, it actually places severe and conflicting constraints on lens design and TEM performance.

Clearly, a tilted grid requires a greater pole-piece separation than one that is perpendicular to the TEM axis. The tilting mechanism also requires space, and so an increased pole-piece separation is needed. The other problem arises if we desire to monitor the emitted radiation. Such spectroscopy is integral to many analytical purposes, but it requires a path by which the radiation can exit from between the pole pieces. Moreover, for X-ray detection, high take-off angles are desirable, and these are physically incompatible with small pole-piece gaps. Hence, the configuration of the lens pole pieces is critical, and it gives rise to two types of widely used sample stages: top-entry and side-entry.

2) Aberrations:

Optical aberration and instrumental instabilities such as power supply and specimen drift are the main limitations for problems in high-resolution work. Axial aberrations are the most important ones for TEMs, and the most important of these are spherical and chromatic (depth-of-focus) aberrations and astigmatism.

The objective lens is commonly the strongest of the several lenses of the TEM. This means it has the greatest deflection angle (Fig. 7-1). A result is that the paths of many diffracted electrons extend further laterally from the optical axis of the TEM than that which occurs with the other lenses. As with glass lenses, distortions increase with distance from the optical axis, and thus aberrations are most severe for the objective lens. The spherical aberration determines the number of diffracted beams that can be passed through the objective lens without production of unacceptable misphasing and thus image distortions. C_s, the

spherical aberration constant, is commonly used as an indicator of the severity of the spherical aberration. The C_s can be decreased by closing the gap between pole pieces, narrowing the bore of the lens, or increasing the strength of the magnetic field. However, decreasing the size of the opening in the lens restricts sample handing, and increasing the field strength causes saturation of the magnetic material, effectively increasing the dimensions of the pole piece. Thus, difficult compromises are required in order to decrease the C_s. For most purposes aberrations can be neglected for the other TEM lenses.

Spherical aberration is commonly the dominating factor in limiting maximum resolution, but for thicker samples chromatic aberration is of greatest concern. Chromatic aberration arises from instabilities in the electron source and from interaction between the electron beam and the specimen. Both effects result in changes in the wavelength of the electron beam, which explains why it is called chromatic aberration. A range in beam wavelength produces a corresponding range of focal lengths together with inevitable blurring of the image. The same effect is produced by instabilities of the objective-lens current. Much effort is devoted to minimizing high-voltage and lens-current instabilities in the electron source of the TEM and the energy spread of the electrons as they leave the filament. However, even with the most stable sources and best designed filaments, there will be energy losses resulting from inelastic interactions as the beam passes through the specimen. Thus, chromatic effects are unavoidable.

Astigmatism is produced by image distortions resulting when the magnetic field of a lens is not perfectly symmetrical.

3) Image recording:

The primary method for recording images with the TEM is by photography; data for analytical microscopy is recorded by spectrometry. Photographic film and video are the choice for most purposes [9].

§ 7. 4 Sample Preparation

The preparation of samples is one of the critical steps in many analytical methods, and particularly for TEM analysis. Depending on the nature of the TEM study and the desired results, sample preparation can be of minimal importance or it can be crucial.

For TEM imaging, a small thickness is desirable. The strong interaction of electrons with matter means that especially for high-resolution imaging there is a premium in using thin specimens to minimize multiple scattering events; the mean free path in solids for elastic scattering ranges from a few nm for heavy elements to a few tens of nm for light elements. Thicknesses no greater than the mean free path are best for images in which we wish to see maximum structural details. Preparing such samples can be challenging.

Perhaps the simplest way of preparing samples for the TEM is by crushing them into small grains.

Ultramicrotomy is used for samples that can be prepared by cutting them into extremely thin sections, such as is typically done with tissues in biological samples. Fortunately, suitable aerogel which is soft and highly porous, can be fixed, dehydrated, embeded within a matched epoxy and then sliced, much like a salami is sliced in a delicatessen. The result is a series of extremely thin wafers that can be floated onto sample grids and examined directly with the TEM.

There is a well-defined series of steps in the fixation, dehydration and embedding of

biological specimens, and in general it is only necessary to adopt a very standard routine [6]. The aim of the whole procedure is to produce blocks which can be sectioned and which contain specimens in which the fine structure is preserved with as little alteration as possible when compared with the original.

Fixation is the first step in the preparation of the aerogel for examination by TEM of thin sections and has the aim of stabilizing pore space to such an extent that ultrastructural relations are preserved despite the subsequent rather drastic treatments of dehydration, embedding and exposure to the electron beam.

Most embedding media are not soluble in water, and consequently fixed specimens are "dehydrated" by passing them through a sequence of solutions, the last of which is miscible with the embedding medium. The two most widely used dehydrating agents are ethanol and acetone.

In the final stage of preparing a specimen in a form suitable for thin-sectioning it is infiltrated with a liquid embedding medium which is then polymerized to produce a solid block.

With modern ultramicrotomes it is relatively easy to cut sections 50 to 100 nm thick from the majority of biological specimens. Sections less than 50 nm thick may be required for high resolution work and this will call for a little more care and patience.

SEM: A piece of aerogel was mounted on a sample plate with an adhesion double sided carbon tape. The sample was uncoated in order to preserve the original texture. The SEM microscope was a HITACHI S-4500 equipped with a field emission gun as the electron source. Because of the low electrical conductivity of the sample, the image was degraded and

unstable due to charge built up. This problem was resolved by using a low accelerating voltage of 2.0 kV. Some samples were mounted on silver blocks, sputter-coated in an argon atmosphere with gold using a sputter coater, and then examined and photographed at 15 kV in the upper stage of a Hitachi S-530 scanning electron microscopy.

TEM: Two methods were used in sample preparation. In one the aerogel was sonicated into fine powder in distilled water. The suspension was deposited on a holey carbon film supported by a the copper grid. A sample was obtained when the suspension was dried for TEM.

In the second approach the blocks and the pellets of aerogels were fixed in 3% gluteraldehyde in 0.2 mol/L sodium cacodylate buffer for 1 hour, postfixed in 1% osmium tetroxide, and dehydrated by increasing the concentration of ethanol at 50% (10 min), 70% (10 min), 95% (10 min), 100% (30 min), propylene oxide (10 min). It was then embedded in Epon 812 for 19 hours followed by a curing process at 60 C for 16 hours. Ultrathin sections were cut into 40-70 nm by using a diamond knife of a LKB Bromma Ultramicrotome System. The films were mounted on a 400- mesh copper grid. The TEM studies were performed using a Phillips CM200 TEM with high resolution pole pieces (Cs=1.2 mm) which gives a point to point resolution of 0.24 nm at 200 kV.

§ 7. 4 Results and Discussion

Figure 7-2 is a typical secondary electron SEM image of the aerogel sample. SEM has permitted a study of three-dimensional views of surface pores. The texture on the surface shows a great uniformity in respect to the grain size and the pore structure. This monograph contains much evidence that the interpore structure (designated as particle space) is

constructed by near uniform grains of elliptical shapes with 30 x 50 nm axes. In some areas, the grains are loosely packed, whereas in others, it appears that a few of the grains agglomerate into a larger grain. The percentage of the pore space, estimated from this micrograph, is roughly 5%.

Figure 7-3 is a TEM micrograph of the sample prepared by sonicated dispersion. The area shown in the micrograph is a region hanging over a hole in the carbon film. In the thin areas, individual crystalline particles of approximately 5 nm × 10 nm in size are visible (marked by arrows). The nanoparticles interconnect into a network structure, which encompasses abundant small pore space of about 15 nm diameter in size. Excluding the large open space in the upper left corner of the micrograph, we estimate that the pore area occupies roughly 50% of the cross-sectional area.

Figure 7-4 shows a high resolution image of a sample that was microtomed. Though only about 60 nm thick, the sample is a relatively thick compared to the particle size and hence can be regarded as representative of a bulk sample. The individual crystalline particles are outlined by lattice fringes 0.36 ± 0.03 nm apart, which represent the (101) planes spacing in anatase.

The size of the crystallites can be more clearly seen in the dark field imaging at a slightly lower magnification (Figure 7-5). The individual crystallites are about 5 nm in diameter with irregular shapes that resemble ellipses with an axial ratio of 1.1/1.4. These particles look like the grains in the SEM image but are one order of magnitude smaller in size.

A convergent beam electron diffraction (CBED) pattern corresponding to the area in Figure 7-4 is shown in Figure 7-6. The pattern contains a set of rings that correspond

(1)0.36, (2)0.24, (3)0.19 nm in the d spacing, representing d(101), d(004), d(200) of anatase respectively. The ring pattern was formed by very fine randomly distributed crystalline particles.

Figure 7-7 is a microdiffraction pattern predominantly from a single crystallite using a 10 nm probe size to select the particle. Due to its small particle size, the pattern is limited to only a few diffraction spots.

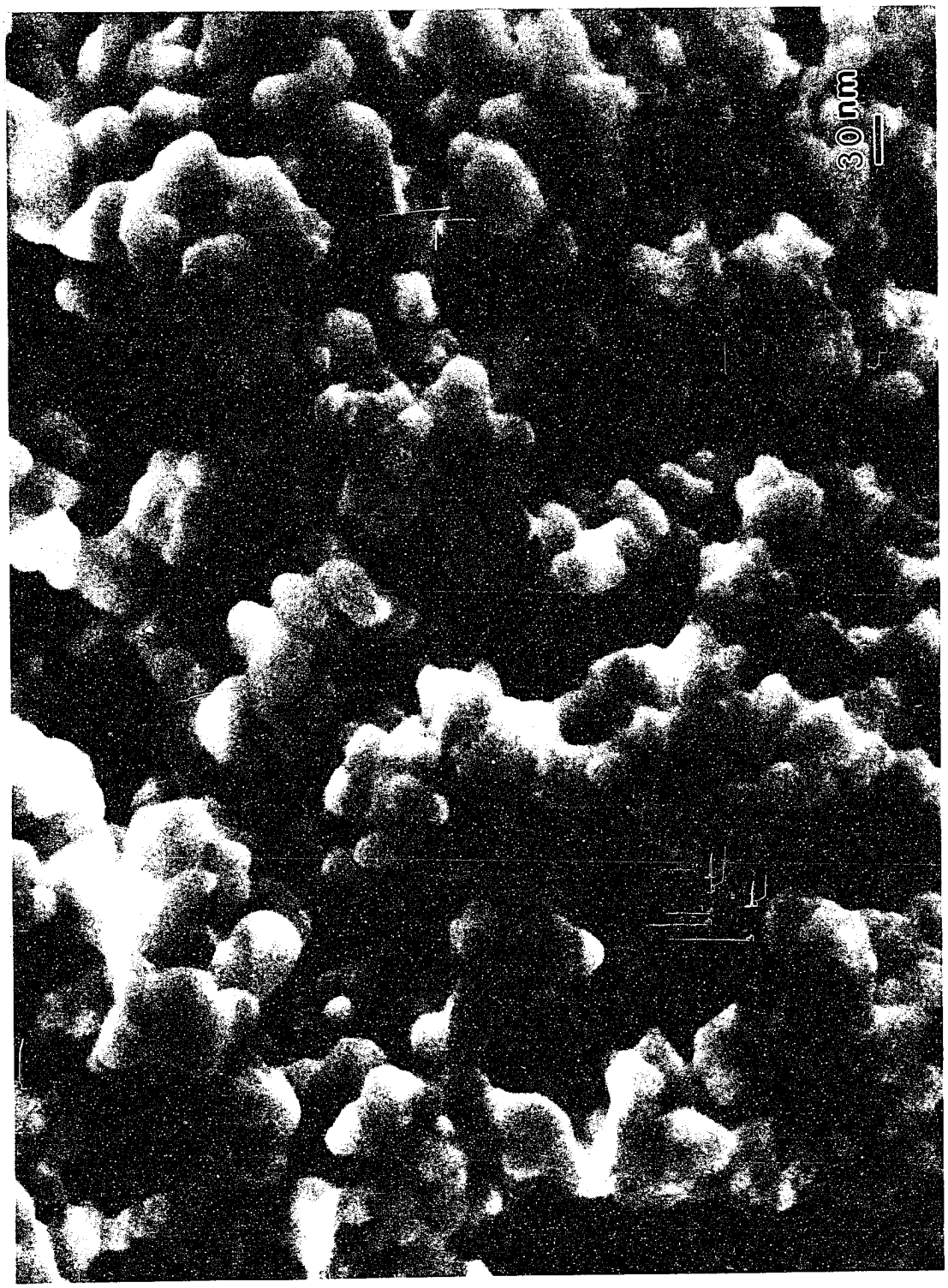

Figure 7-2 SEM images of TiO_2 aerogel.

Figure 7-3 TEM image of a sonicated dispersion TiO_2 aerogel after evaporation of the solvent.

Individual crystalline particles of approximately 5 nm in size are visible (marked by arrows).

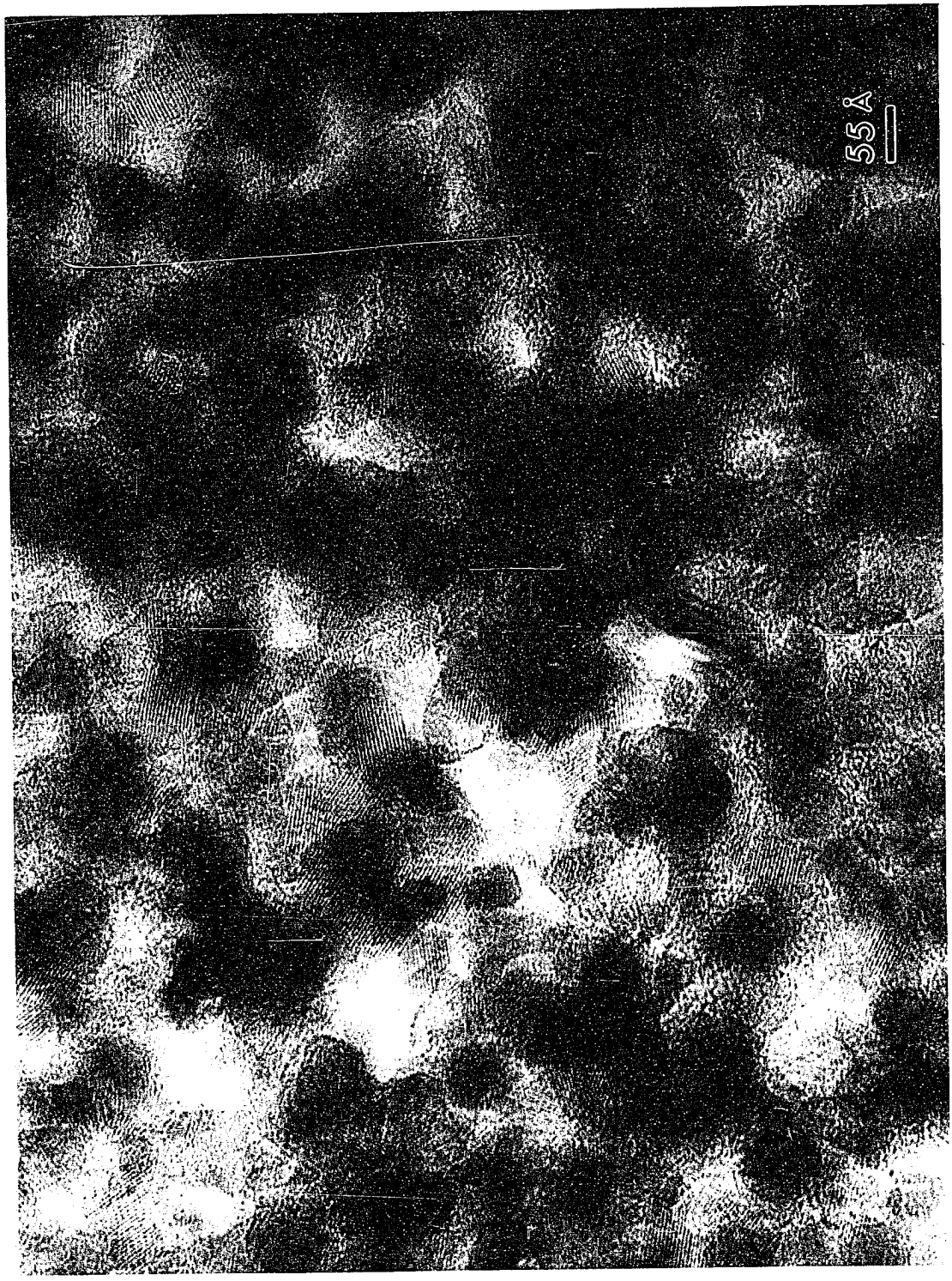

Figure 7-4 High resolution TEM lattice image of microtomed TiO_2 encapsulated aerogel section.

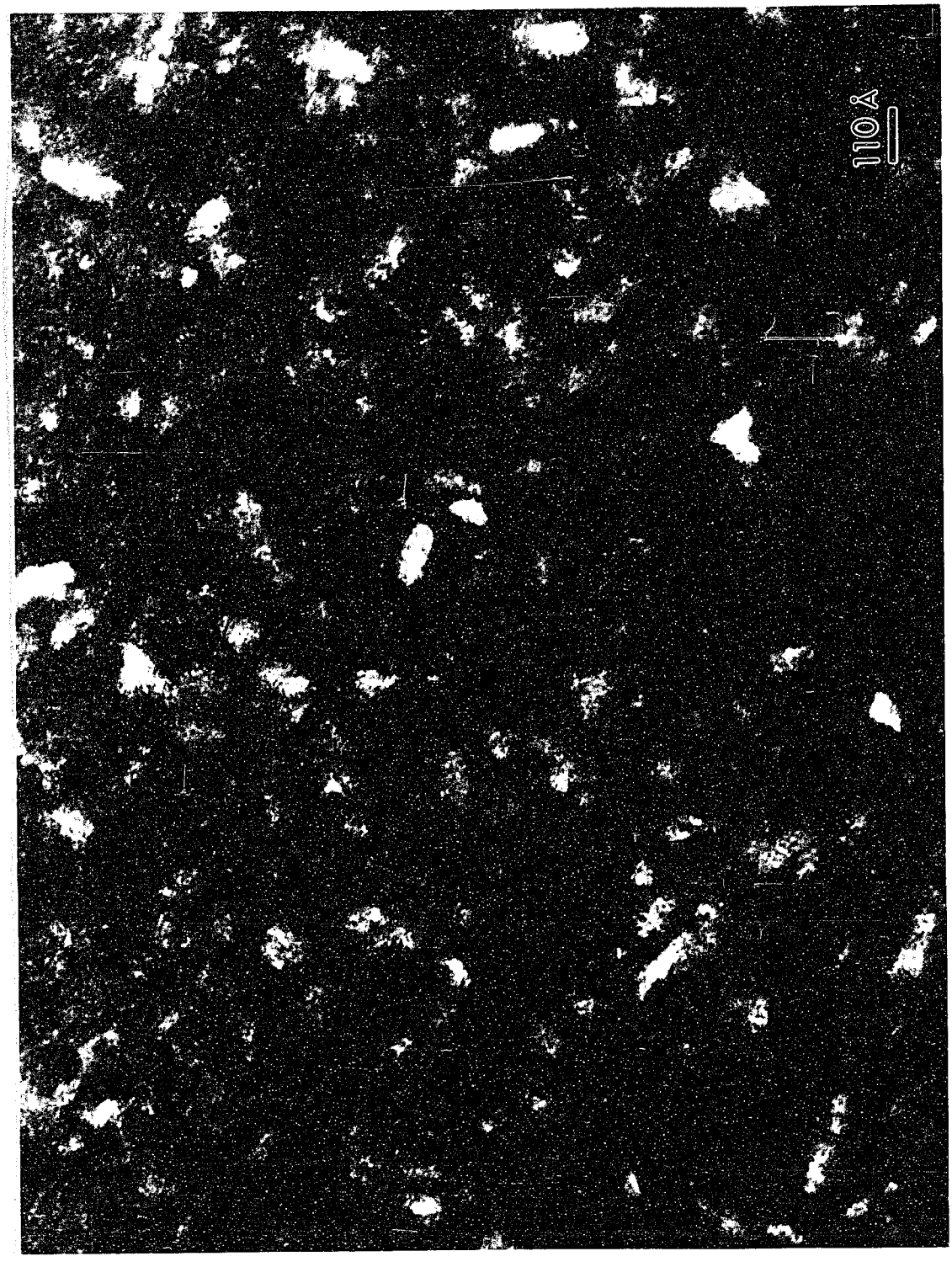

Figure 7-5 Dark field TEM image of microtomed TiO_2 encapsulated aerogel section.

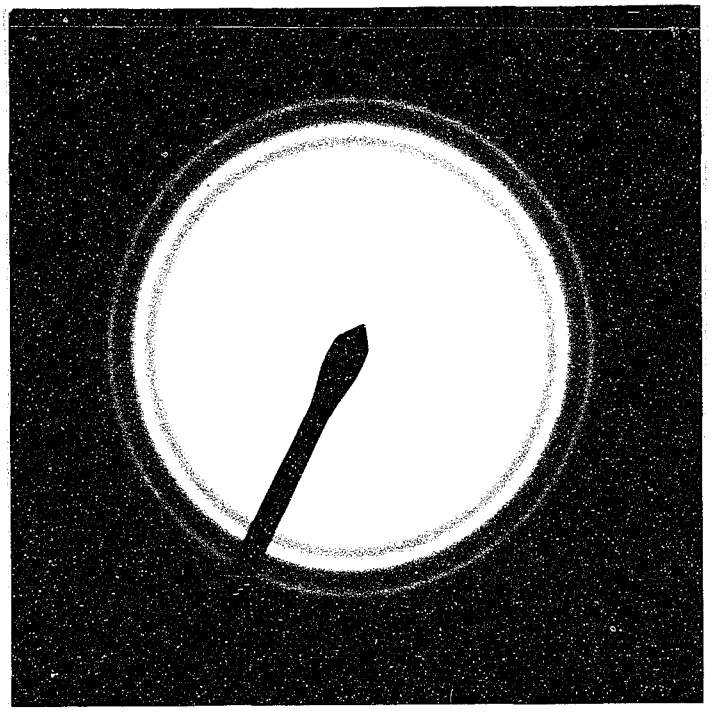

Figure 7-6 Convergent Beam Electron Diffraction pattern of the section shown in Fig. 7-4.

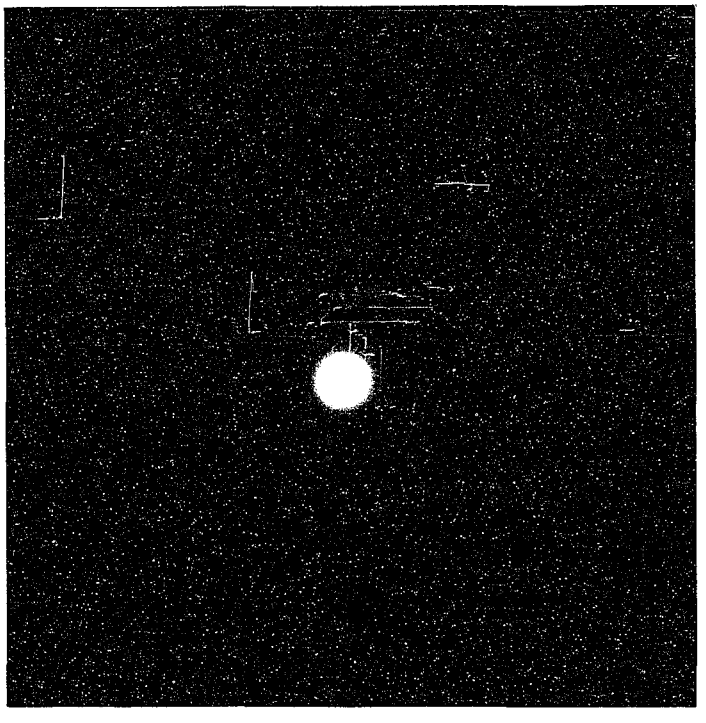

Figure 7-7 Microdiffraction pattern of the section shown in Fig. 7-4.

CHAPTER 8. Conclusion

We have presented the results from four major characterization techniques. Each of these techniques is independent and all of them are complementary. The information we got from each technique are consistent with each other even though each one has its own advantages and disadvantages. First, the different aspects of the techniques will be discussed. Then a morphology model of titanium dioxide aerogels will be presented based on all the information supplied by these characterization techniques.

The techniques used to characterize the structure of TiO_2 aerogels revealed different aspects of the morphology. The nitrogen adsorption and X-ray diffraction reflect the average property of the entire sample. The nitrogen adsorption provides global parameters such as the total surface area and differential global parameters such as the distributions of the volume and area of the pores. X-ray diffraction provides information on the average crystal size weighted towards the large particles. The electron microscopies provide model-independent particle size distributions on two different length scales. And SANS provides a model-dependent particle size distribution with good statistics.

Electron beams can be focused into far smaller regions than is normally possible with X-rays (electron beams as small as 0.3 nm can be used, whereas X-ray beams are commonly 0.25 to 0.5 mm across.). This difference gives rise to both advantages and disadvantages relative to X-ray instruments. TEMs routinely provide far higher spatial resolutions – in several respects – than do X-rays. The advantage is that the electron beam can produce diffraction from significantly smaller volumes than is possible with conventional XRD measurements. The disadvantage is that the averaging over substantial volumes of crystal (>

10^{12} nm^3) that typically occurs with X-rays is impractical with electrons, which typically average over volumes between 10^{-1} and 10^{8}. (a rather substantial difference!).

In addition, there is a loss of information in small-angle scattering experiments caused by averaging the over all orientation in space. The three-dimensional structure is represented by a one-dimensional function which is dependent of the scattering intensity on the scattering angle. This is a also true for powder diffraction. To recover the structure uniquely is therefore impossible. It should be noticed that it is possible to find different models that fit the data within statistical accuracy. In order to reduce this ambiguity it is necessary to have additional independent information from other experiments. Wrong models, however, can be rejected when their scattering function differs significantly from the experimental data.

Electron microscopy is in competition with the scattering methods. It has the big advantage of giving real pictures with rather high resolution. Because of this capability, microscopy is the reference technique often used in the standardization of other methods. But it has the inherent disadvantage that the preparation may introduce artifacts and lack of statistical evaluations.

It is time to summarize the basic information from all these techniques. The nanoparticles are readily observable in the TEM. In some cases the lattice image can also be observed (Fig. 7-4 and 7-5). The lattice spacing is consistent with the anatase structure. The single crystallite electron diffraction pattern shows a sharp diffraction pattern (Fig. 7-6). A larger field of view will average the orientations of crystalline particles to result in the concentric rings shown in Fig. 7-5; this pattern is again consistent with anatase. The X-ray diffraction pattern (Fig. 5-7) which averages over the entire sample is, again, consistent with

the theoretical pattern of anatase. The peak width measurement of the X-ray diffraction pattern indicates 5.8 nm crystallites. The density of anatase is 3.8 g/cm^3 and the skeletal density measured by helium pyknometry is 2.7 g/cm^3. Thus the porosity of the nanoparticles can be calculated from the two densities i.e., 29%. This is very close to the porosity of theoretical hexagonal close packing spheres 26% [1]. By taking the limiting cases, if we now take BET total surface area (447 m^2/g) and assume that the entire surface area originates from the anatase nanoparticles, the average diameter of the nanoparticles is calculated to be 3.5 nm which is the limit of the smallest possible size. On the other hand, in terms of size derived from SANS Porod's method, nanoparticles are about 27 nm which is an over-estimate of the true size because it assumes the particles are not touching. So both approaches give a set limit for the sizes of the nanoparticles.

It is difficult to determine the morphology of the mesoaggregate from Figure 7-2. But it can be described in terms of coordination number of the nearest neighbors. It is obvious that the structure from Figure 7-2 is random and homogeneous. Thus a possible structure should be a coordination number of randomly packed spheres; it will result in the total measured porosity of 80%. The coordination number that satisfies this is somewhere between 3 and 4 [1].

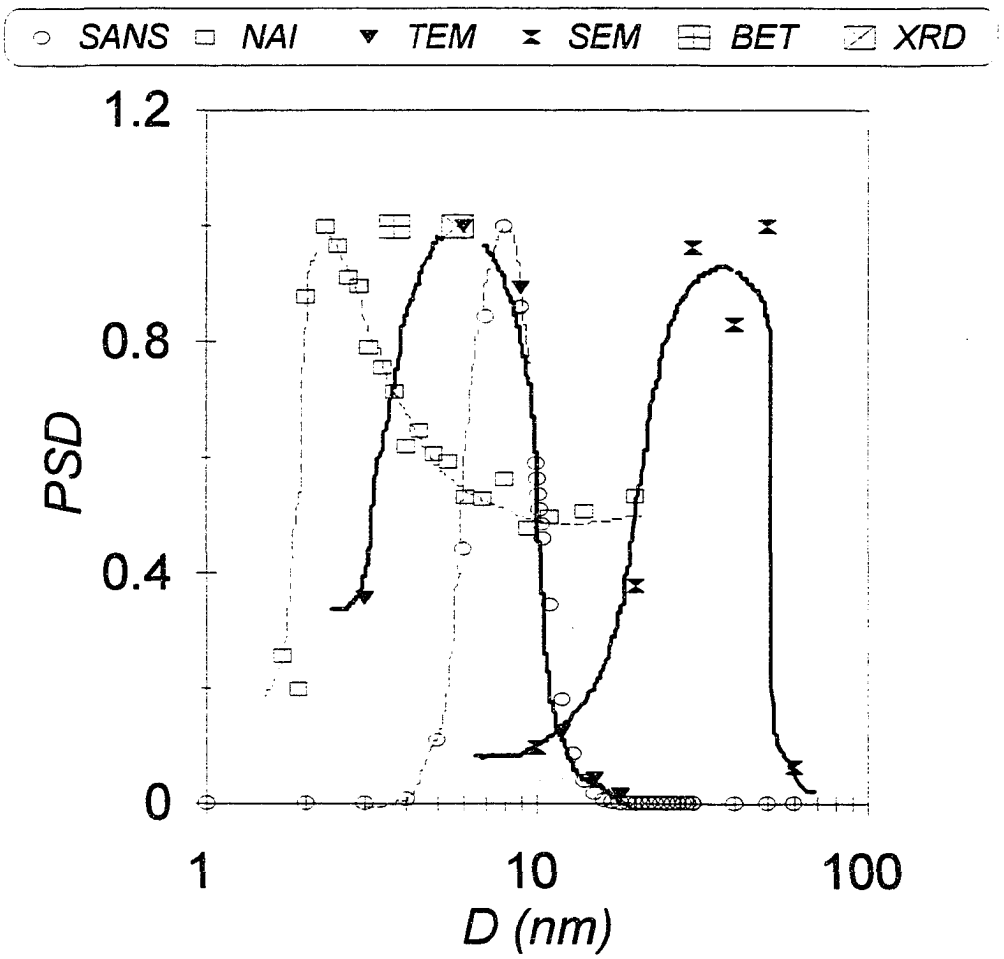

Figure 8-1 The particle size distributions that were derived from the various techniques - BET, XRD, SANS, and TEM, SEM.

Figure 8-1 shows the particle size distributions (PSD) that were derived from all these techniques. Nitrogen adsorption measurements provide information about two parameters: at low pressure we obtain surface area from BET adsorption isotherms, while at the higher pressure we obtain differential condensation that provides information about pore distribution. In Figure 8-1 we have converted the surface area into particle size by assuming that the nitrogen penetrates inside the mesoaggregates and measure the surface area of the nanoparticles (BET). We also assume that the nanoparticles are spherical and uniform. Hence - the contribution from this measurement is included in Figure 8-1 as a point that indicates the average particle size. This is also true for the information that was derived from the X-ray powder diffraction data (XRD).

As to the pore size distribution (PSD) that was derived from the nitrogen adsorption data (NCM) - we assume that the large pores, that constitute the inter-mesoaggregate space, contribute only to the tail-end of the distribution and that the pore distribution reflects primarily that of the mesoaggregates. The largest diameter of a pore-space in the mesoaggregate should be of the order of the diameter of the nanoparticle, hence, the pore space was left as such with no attempt at converting it into particle space. The distributions were normalized such that wherever there is a peak in the distribution, the maxima are set at PSD = 1. The scale on the X-ray powder diffraction and BET data, that are represented by a single point, is set at PSD = 1. With all the intrinsic limitations that surface with attempts to compare morphological information deduced from results that were obtained from such a wide spectrum of techniques, the ability to present the data on a single graph might be considered rewarding. The bimodal particle distribution is evident. It is also apparent that

most of these techniques are sensitive mostly to the nanoparticles. Only the SEM, the bulk density and the skeletal density provide data consistent with the mesoaggregates.

The most important conclusion that we derived from these data was the degree of uniformity in the structural elements of the TiO_2 aerogels. We have defined the morphology of the TiO_2 aerogels in terms of two length scales and three densities (or coordination numbers): the size and density of the nanoparticle, the size and density of the mesoaggregates and the total geometric density. These parameters determined the morphology of the TiO_2 aerogels.

As a quick summary, a schematic morphology model consistent with all the experimental data presented here is constructed and illustrated in Figure 8-2. This model consists of closely-packed crystalline nanoparticles of about 5 nm in diameter, which form loosely packed mesoaggregates of about 50 nm in diameter with an overall porosity of 80%.

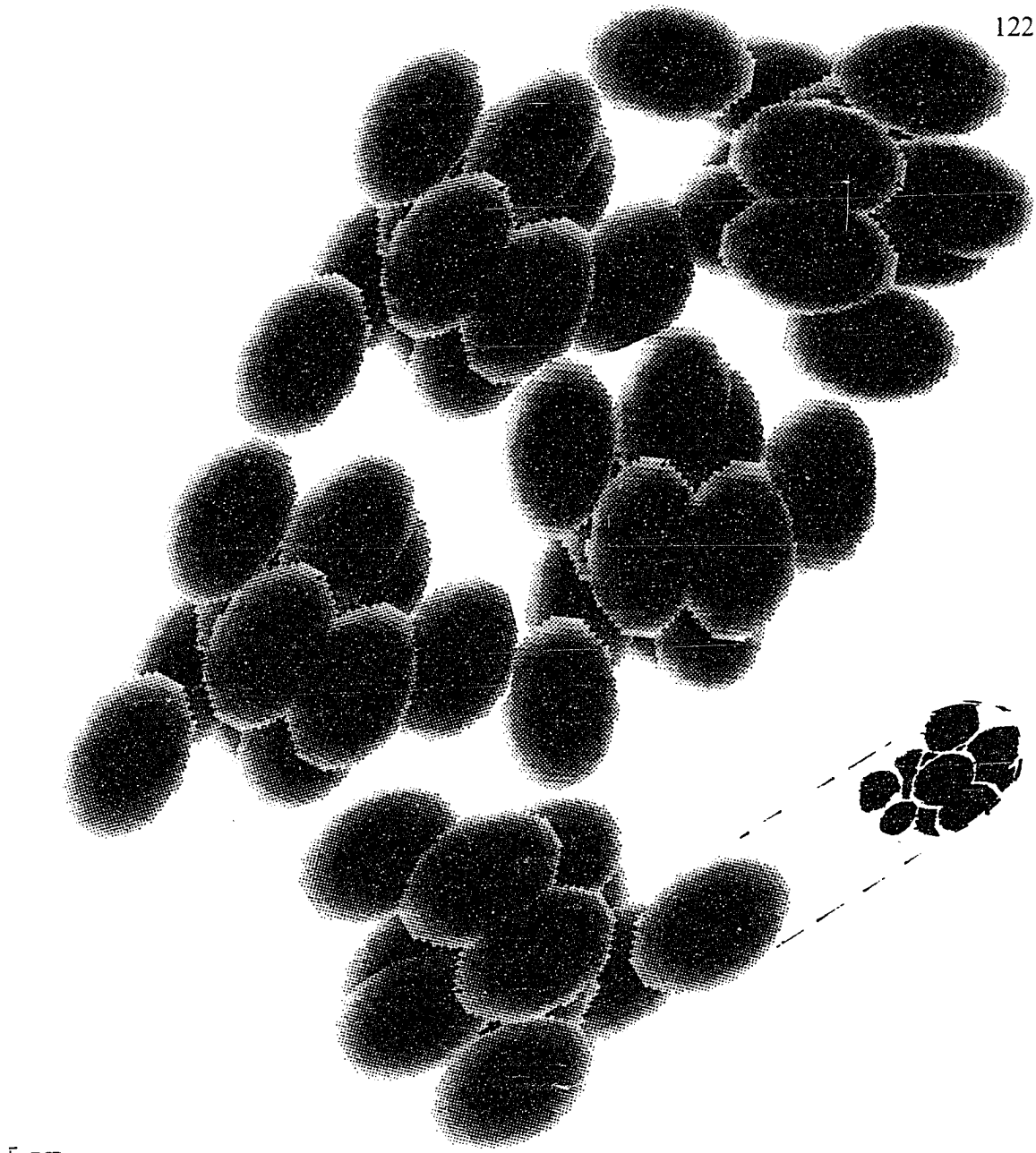

Figure 8-2 A schematic morphology model of the TiO_2 aerogels with two length scales.

APPENDIX Characteristics and Performance of 30-meter NG7-SANS

Source:	neutron guide (NG7), 50×50 cm^2.
Monochromator:	mechanical velocity selector with variable speed and pitch.
Wavelength Range:	0.5 to 2.0 nm.
Wavelength Resolution:	10% to 30% $\Delta\lambda/\lambda$ (FWHM).
Source-to-Sample Distance:	3.0 to 15 m in 1.5 m steps via insertion of neutron guide segments.
Sample-to-Detector Distance:	primary detector, 3.5 to 15 m wide-angle detector, 2 m, 0 - 40°, in developing.
Collimation:	circular pinhole collimation.
Sample Size:	5 - 25 mm diam.
q - range:	primary detector, 0.01 to 6 nm^{-1}
Size Regime:	1 to 600 nm.
Detectors:	65×65 cm^2 ^3He position-sensitive proportional counters (1×1 cm^2 resolution).

Neutrons on Sample vs. q_{min}:

q_{min} (nm^{-1})	I(q)* (n-sec)
0.01	2×10^4
0.02	6×10^4
0.04	9×10^5
0.10	5×10^6

* estimated for 1.5 cm diam sample with $\Delta\lambda/\lambda = 0.25$.

BIBLIOGRAPHY

CHAPTER 1

1. Ed., Corapcioglu, M.Y., *Advances in Porous Media* Vol 1&2. Elsevier Science (1994).
2. Dullien, F. A. L., *Porous Media Fluid Transport and Pore Structure*, Academic Press Inc. (1991).
3. Ed., Jacobs, P.A., Jaeger, N.I., *Zeolite Chemistry and Catalysis*, Proceedings of International Symposium, Prague, Czechoslovakia, 8-13 September 1991, Elsevier Science (1991).
4. Ed., Murakami,Y., Ijima, A. and Ward, J.W., *New Developments in Zeolite Science and Technology*, Proceedings of the 7th International Zeolite Conference, Elsevier Science (1986).
5. Pampuch, R., *Constitution and Properties of Ceramic Materials*, Elsevier Science (1991).
6. Ed., Brannon-Peppas, L. and Harland, R.S., *Absorbent Polymer Technology*, Elsevier Science (1990).
7. Ed., Hrino, R. and Lang, W., *Porous Silicon and Related Materials*, Proceedings of Symposium on Porous Silicon and Related Materials of the 1994 E-MRS Spring Conference, Strasbourg, France, Elsevier Science (1995).
8. Schaefer, D.W. *Engineered Porous Materials*, MRS Bulletin, **1994**, XIX, (4).
9. Kistler, S. S., *Nature*, **1931**, (127), 741.
10. Kistler, S. S., and Swann, S., *Ind. Eng. Chem.*, **1934**, (26), 388.

11. Nicolaon, G. A., and Teichner, S. J., *Bull. Soc. Chim. Fr.*, **1968**, 1906.

12. Vicarini, M. A., Nicolaon, G. A., and Teichner, S. J., *Bull. Soc. Chim. Fr.*, **1969**, 1466.

13. Vicarini, M. A., Nicolaon, G. A., and Teichner, S. J., *Bull. Soc. Chim. Fr.*, **1970**, 165.

14. Ed., Bergna, H.E., *The Colloid Chemistry of Silica*, American Chemical Society, (1994).

15. Brinker, C.J. and Scherer, G.W., *Sol-Gel Science*, Academic Press, Inc. (1990).

16. Jones, R. W., *Fundamental Principles of Sol-Gel Technology*, The Institute of Metals, London (1989).

CHAPTER 2

1. Fox, A. M. And Dulay T. M., Chem. Rev., **1993**, (93), 341-357.

2. R. Hill and M. D. Archer, *J of Photochemistry and Photobiology, A: Chemistry*, **1990**, (51), 45-54.

3. Yu. Ya Gurevich and Yu. V. Pleskov, *Photoelectrochemistry of Semiconductors*, Semiconductors and Semimetals Vol.19, Academic Press, Inc. (1983).

4. Banfield, J. F. and Veblen, D. R., *American Mineralogist*, **1992**, (77), 545-557.

5. Nolan, R. P., Langer, A. M., Weisman, I. and Herson, G.B., *British Journal of Industrial Medicine*, **1987**, (44), 687-698.

6. Clark, R. J. H., *The Chemistry of Titanium And Vanadium*, Elsevier Science (1968).

7. 1994 Ed., *Compton's Encyclopedia.*

8. Kippenhahn, R., *Discovering The Secrets of The Sun*, John Wiley and Sons, (1994).

9. Solomon, D.H. and Hawthorne, D.G., *The Chemistry of Pigments and Fillers*, John Wiley and Sons, (1983).

10. Ed., Serpone, N. and Pelizzetti, E., *Photocatalysis Fundamentals and Applications*, John Wiley & Sons, (1989).

11. Ed., Fricke, J. *Aerogels, Proc. 1st. Int. Symp.*, Springer-Verlag, Berlin Heidelberg, (1986).

12. Gesser, H.D. and Goswami, P.C., *Chem. Rev.* **1989**, 89, 765.

13. Dagan, G., Tomkiewicz, M., *J.Phys. Chem.* **1993**, 97, (49), 12651-12655.

14. Jackson, N.B., Wang, C.M., Luo, Z., Schwitzgebel, J., Ekerdt, J.G., Brock, J.R., Heller, A., *J. Electrochem. Soc.*, **1991**, 138, 3660-3664.

15. Tomkiewicz, M., Dagan, G. and Zhu, Z. , *Res. Chem. Intermed.*, **1994**, 20, (7), 701-710.

16. Ehrich, J.B., Logan, A.D., Datye, A.K., Smith, D.J., *Journal of Catalysis*, **1989**, 118, 227-237.

17. Tomkiewicz, M. and Kelly, S., *Proc. of NATO workshop on "Fine Particles Science and Technology - from micro to nanoparticles"*, Italy, **1995**.

18. Vlachopoulos, N., Lisk, P., Augustynski, J. and Gratzel, M., *J. of Am. Chem. Soc.*, **1988**, (110), 1216.

19. Duong, D., Ramsden, J. and Gratzel, M., *J. Of Am. Chem. Soc.*, **1982**, (104), 2977.

CHAPTER 3

1. Iler, R. K., *The Chemistry of Silica*, John Wiley & Sons, (1979).

2. Unger, K. K., *Porous Silica*, Elsevier Science, (1979).

3. Lowell, S., *Powder Surface Area and Porosity*, John Wiley & Sons, (1979).

4. Dubinin, M. M., *J. Colloid interface Sci.*, **1967**, (23), 487.

5. IUPAC, Manual of Symbols and Terminology, Appendix 2, Part I, *Pure and Appl.Chem*, **1972**, (31), 578.

6. Sing, K.S.W., Evertt, D.H., Haul, R.A.W., Moscou, L., Pierotti, R.A., Rouquerol, J. and Siemieniewska, T., *Pure and Applied Chemistry*, **1985,** (57), 603.

7. Brunauer, S., Mikhail, R. Sh. and Bodor, E. E., *J. Colloid interface Sci.*, **1967**, (24), 451.

8. Ed., Unger, K., Rouquerol, J., Sing, K.S.W. and Kral, H., *Characterization of Porous Solids,* Proceedings of the IUPAC Symposium, Bad Soden, Germany, April 26-29 (1987).

9. Ed., Rodrguez-Reinoso, F., Rouquerol, J., Sing, K.S.W. and Unger, K.K., *Characterization of Porous Solids II*, Proceedings of the IUPAC Symposium (COPS II), Alicante, Spain, Elsevier Science, (1990).

10. Ed., Rouquerol, J., Rodrguez-Reinoso, F., Sing, K.S.W. and Unger, K.K., *Characterization of Porous Solids III*, Proceedings of the IUPAC Symposium (COPS III), Marseille, France, Elsevier Science, (1993).

11. Hackley, V.A., Anderson, M.A., and Spooner, S., *J. Mater. Res.*, **1992**, (7), 9, 2555-2571.

CHAPTER 4

1. Gregg, S.J. and Sing, K.S.W., *Adsorption, Surface Area and Porosity*, Academic Press, New York, (1976).

2. Brunauer, S., Emmett, P.H. and Teller, E., **1938,** *J. Am. Chem. Soc.* (60), 309.

3. Gregg, S.J., Sing, K.S.W., *Adsorption, Surface Area and Porosity*, Academic Press, New York, (1982).

4. Lowell, S., *Powder Surface Area and Porosity*, John Wiley & Sons, (1979).

5. Camp, R. W. and Stanley, H. D., **1991,** *American Laboratory*, (9).

6. Nelson, F. M. and Eggertsen, F.T., **1958**, *Anal.Chem.* (30), 1387.

7. Ed., Fricke, J., *Proceedings in Physics*, Vol. 6, Springer-Verlag, Berlin, (1986).

8. Brinker, C.J., Scherer, G.W., *Sol-Gel Science,* Academic Press, Inc. (1990).

CHAPTER 5

1. Wright, A. C., *A compact representation for atomic scattering factors*, Clay & Clay Minerals, 1973, (21), 489-490.

2. Cullity, B. D., *Elements of X-Ray Diffraction*, Addison-Wesley Publishing Co., Inc., New York, (1978).

3. Klug, H. P. and Alexander, L. E., *X-ray Diffraction Procedures for Polycrystalline and Amorphous Materials*, Addison-Wesley Publishing Co., Inc., New York, (1974).

4. James, R. W., *The Optical Principles of the Diffraction of X-Rays*, Cornell Univ. Press, Ithaca, New York, (1965).

5. JCPDC Mineral Powder Diffraction Data File 21-1272, 21-1276, Park Lane, Pennsylvania, (1980).

6. Bergeron, C.G. and Risbud, S.H., *Introduction to Phase Equilibria in Ceramics*, The American Ceramic Society, (1984).

CHAPTER 6

1. Li, J. C., Ross, D. K. and Benham, M. J., *J. Appl. Cryst*, **1991**, (24), 794-802.

2. Jones, A. F., Parker, I. B. and Stacey, M. H., *J. Appl. Cryst*, **1991**, (24), 607-615.

3. Acharya, D.R, Crowley, T.L., Hughes, R., Koon, C.L., Menendez, M., Rieutord, F., *J. Appl. Cryst*, **1990**, (23), 424-429.

4. Vezin, V., Goudeau, P.H., Naudon, A., Herino, A., Bomchil, G., *J. Appl. Cryst*, **1991**, (24), 581-587.

5. Semenyuk, A.V., Svergun, D.I., Mogilevsky, L.Yu., Berezkin, V.V., Mchedlishvili, B.V., Vasilev, A.B., *J. Appl. Cryst*, **1991**, (24), 809-810.

6. Fratzl, P., Vogl, G. and Klaumunzer, S., *J. Appl. Cryst.*, **1991**, (24), 588-592.

7. Allen, A.J., *J. Appl. Cryst*, **1991**, (24), 624-634.

8. Vollet, D.R. and Craievich, A.F., *Advances in Cement Research*, **1988**, 1, (2), 107-111.

9. Vollet, D. R., Varela, J. A., *J. Am. Ceram. Soc*, **1991**, (74), 10, 2683-2685.

10. Long, G.G., Krueger, S., Jemian, P.R., Black, D.R., Burdette, H.E., Cline, J.P. and Gerhard R.A., *J. Appl. Cryst.*, **1990**, (23), 535-544.

11. Krueger, S., Long, G.G., Black, D.R., Minor, D., Jemian, P.R., Nieman, G.W. and Page, R.A., *J. Am. Ceram. Soc.*, **1991**, 74, (10), 2538-2546.

12. Muller-Stach, M., Franz, H., Herr, U., Peisl, J., Petry, W., Wallner, G., *J. Appl. Cryst*, **1991**, (24), 603-606.

13. Hackley, V. A., Anderson, M. A., Spooner, S., *J. Mater. Res.*, **1992**, (7), 9, 2555-2571.

14. Pahl, R., Bonse, U., Pekala, R.W., Kinney, J.H., *J. Appl. Cryst.*, **1991**, **24**, 771-

776.

15. Wang, P., Emmerling, A., Tapper, W., Spormann, O., Fricke, J., Haubold, H.G., *J. Appl. Cryst.*, **1991** (24), 777-780.

16. Emmerling, A., Goswin, R., Gross, J., Reichemauer, G., Fricke, J., Haubold, H.G., *J. Appl. Cryst.*, **1991**, (24), 781-787.

17. Heinrich, T., Raether, F., Spormann, O., Fricke, J., *J. Appl. Cryst.*, **1991**, (24), 732-739.

18. Harold, D.B., Schmidt, P.W., *Phys. Rev. Let.*, **1984**, (53), 6, 596-599.

19. Rothwell, W.S., *J. Appl. Phys.*, **1968**, (39), 3, 1840-1845.

20. Feigin, L.A. and Svergun, D.I., *Structure Analysis by Small-Angle X-ray and Neutron Scattering,* Plenum Press, New York, (1987).

21. Ed., Glatter, O. And Kratky, O., *Small Angle X-ray Scattering,* Academic Press, New York, (1982).

22. Ed., Shapiro, S. M., Moss, S. C. and Jorgensen, J. D., Mat. Res. Soc. Symp. Proc., **1990**, (166).

23. Guinier, A. And Fournet, G., *Small-Angle Scattering of X-Rays*, John Wiley & Sons, Inc., New York, (1955).

24. Ed., Brumberger, H., *Small Angle X-ray Scattering*, Gordon and Breach, New York, (1967)

25. Debye, P., Anderson, H.R., Brumberger, H.Jr., *J. Appl. Phys.* **1957**, 28, (6), 679-683.

26. Harkness, S.D., Gould, Hren, R.W., *Phil. Mag.*, **1969**, 19, 115-128.

27. Baur, R., Gerold, V., *Acta Metallurgical*, **1964**, 12, 1449-1453.

28. Neilson, G.F., *J. Appl. Cryst.*, **1973**, **6**, 386-392.

29. Ed., Donald, C., *Modern spectrum Analysis*, New York IEEE Press, 1978.

30. Gull, S.F., Daniell, G.J., *Nature*, **1978**, 272, (20), 686-690.

31. Potton, J.A., Daniell, G.J., Melville, D., *J. Phys. D.*, **1984**, 17, 1567-81.

32. Potton, J.A., Daniell, G.J., Rainford, B.D., *J. Appl. Cryst.*, **1988**, 21, 663-668, 891-897.

33. Chen, S.H., Rouch, J., Sciortino, F. and Tartaglia, P., *J. Phys. Condens. Matter*, (in press).

34. Hurd, A.J., Schaefer, D.W., Smith, D.M., Ross, S.B., Méhauté, A.L., Spooner, S., *Phys. Rev.B*, **1989**, 39, 9742-45.

35. Brinker, C.J., Scherer, G.W., *Sol-Gel Science,* Academic Press, Inc. (1990).

36. Jullien, R., Meakin, P., Pavlovitch, A., *Disorder and Granular Media*, Ed. Bideau, D and Hansen, A., Elsevier Science Publishers, New York, (1993).

37. Glinka, C.J., Rowe, J.M., Larock, J.G., *J. Appl. Cryst.,* **1986**, (19), 427-439.

38. Zhu, Z., Lin, M., Dagan, G., Tomkiewicz, M., *J. Phys. Chem.*, (in press).

CHAPTER 7

1. Ruska, E.E., *Bull. Electr. Microsc. Soc. Am.*, **1988**, (18), 53-61.

2. Ed., Fricke, J. *Aerogels, Proc. 1st. Int. Symp.*, Springer-Verlag, Berlin Heidelberg, (1986).

3. Ed., Cheetham, A.K., Brinker, C.J., Mecartney, M.L. and Sanchez, C., *Proc. Mater. Res. Soc.*, **1994**, (346).

4. Schneider, M., Duff, D.G., Mallát, T., Wildberger, M. and Baiker, A., *Journal of Catalysis*, **1994**, 147, 500-514.

5. Brinker, C.J., Scherer, G.W., *Sol-Gel Science,* Academic Press, Inc. (1990).

6. Agar, A.W., Alderson, R.H., and Chescoe, E. *Principles and Practice of Electron Microscope Operation*, Elsevier/North-Holland, Amsterdam, (1974).

7. Spence, J.C.H., *Experimental High-Resolution Electron Microscopy*, Oxford University press, oxford, (1988).

8. Ed., Rossiter, B.W. and Hamilton, J.F., *Physical Methods of Chemistry Vol. IV Microscopy*, John Wiley & Sons, New York, (1991).

9. Ed., Buseck, P.R. *Minerals And Reactions At The Atomic Scale: Transmission Electron Microscopy*, Mineralogical Society of America, (1992).

CHAPTER 8

1. Brinker, C.J., Scherer, G.W., *Sol-Gel Science,* Academic Press, Inc. (1990).